DISSERTATION

SUBMITTED TO THE

COMBINED FACULTIES OF THE NATURAL SCIENCES AND MATHEMATICS

OF THE RUPERTO-CAROLA-UNIVERSITY OF HEIDELBERG, GERMANY

FOR THE DEGREE OF

DOCTOR OF NATURAL SCIENCES

PUT FORWARD BY

KELLY FOYLE

BORN IN: MONTREAL, CANADA

ORAL EXAMINATION: OCTOBER 13^{th}, 2010

SPIRAL ARMS AND THEIR EFFECTS ON SECULAR EVOLUTION AND STAR FORMATION IN DISK GALAXIES

REFEREES: PROF. DR. HANS-WALTER RIX
PROF. DR. RALF S. KLESSEN

"The most important reason for going from one place to another is to see what's in between."
- Norton Juster (The Phantom Tollbooth)

Abstract

We investigate how spiral structure affects the observational properties of disk galaxies both in terms of dynamical secular evolution and of star formation. We derived the first observational estimate of the torque-induced instantaneous angular momentum flow, resulting from non-axisymmetric features in the stellar distribution for a sample of 24 galaxies. The strongest torques were found among barred galaxies. In the inner regions, the average torques are strong enough to redistribute angular momentum on a timescale of $\sim$4 Gyr with an outward angular momentum flow. In examining the role of spiral arms in star formation we found that they do not dominate, even in grand-design spiral galaxies as there is a comparable amount of interarm star formation. Further, we found that the arms show no enhancement in the efficiency of star formation in terms of molecular gas. We searched algorithmically for angular offsets between star formation tracers and found that there was no systematic spatial ordering of these tracers, as would be predictable by a shock triggering model of spiral structure. It seems spiral structure is most likely transient or at least more complex than the simplest models predict. These results point to a spiral structure that plays a lesser role in shaping a galaxy's observable properties as was previously thought. The strength of gravitational torques depends more strongly on bars than on spiral structure, and spiral arms are not regions of enhanced star formation efficiency. At best they act to reorganize the interstellar medium and concentrate the gas.

Zusammenfassung

Wir untersuchen, wie dynamische Entwicklung und Sternentstehung von Scheibengalaxien durch Spiralarmstruktur beeinflusst werden. Es gelang die erste beobachterische Abschätzung des drehmomentinduzierten Drehimpulstransport, der durch eine asymmetrische Sternverteilung entsteht, basierend auf 24 Galaxien. Es zeigt sich, dass Balkengalaxien die stärkste Drehmomente haben. Im Durchschnitt sind die gravitativen Drehmomente in den Zentralbereichen der Galaxien stark genug, um den Drehimpuls auf Zeitskalen von $\sim$4 Gyr nach außen zu transportieren. Wir haben die Sternentstehung in den Spiralarmen und zwischen den Spiralarmen untersucht und gefunden, dass die Sternentstehung in beiden Gebieten vergleichbar stark ist. Zudem zeigen die Arme keine größere Sternentstehungs-Effizienz in Bezug auf molekularen Wasserstoff. Darüberhinaus gibt es keine Anzeichen für eine systematische räumliche Anordnung von Sternentstehungs-Indikatoren, wie man etwa in einem Schock-Trigger-Modell der Spiralstruktur erwarten würde. Diese Ergebnisse legen nahe, dass Spiralarmstruktur nur eine untergeordnete Rolle in der Entwicklung der beobachtbaren Galaxien-Eigenschaften spielt.

Selbst die gravitativen Drehmomente werden stärker durch Balken als durch Spiralarmstruktur beeinflusst. Spiralarme haben keine erhöhte Sternentstehungseffizienz. Es scheint, dass Spiralarmstruktur relativ kurzlebig ist oder mindestens komplexer als einfachste Modelle erwarten lassen.

Contents

Contents i

List of Figures iii

List of Tables vii

1 Introduction 1

1.1 Island Universes . . . 1
1.2 Disk Galaxy Formation . . . 3
1.3 Spiral Galaxies, the Interstellar Medium & Star Formation . . . 5
1.3.1 Components of the ISM . . . 7
1.3.2 Star Formation . . . 8
1.4 Spiral Arms: their Formation, Persistence and Effects . . . 10
1.4.1 Basic Properties . . . 11
1.4.2 Theories of Spiral Structure . . . 13
1.4.3 The Effects of Spiral Arms . . . 16

2 Secular Evolution in Spiral Galaxies 19

2.1 Introduction . . . 20
2.2 Background & Motivation . . . 20
2.3 Determining the Angular Momentum Flow Timescale from Photometric Data . 23
2.4 Testing Torque Estimates using Disk Galaxy Simulations . . . 25
2.4.1 Simulations . . . 25
2.4.2 Projected Mass Densities and the 2D Potential . . . 26
2.4.3 Torques on Stars from Stars versus Torques from the Gas & Dark Matter 28
2.5 The Role of Torques from Stars: a Pilot Study . . . 30
2.5.1 Sample . . . 30
2.5.2 Stellar Mass Maps . . . 33
2.5.3 Making Radial Torque and Angular Momentum Profiles . . . 37
2.5.4 M100 - Comparison with the analysis Gnedin, Goodman & Frei (1995) 44
2.6 Results & Discussion . . . 44

2.7 Conclusion 51

3 Arm & Interarm Star Formation 53
3.1 Introduction 53
3.2 Analysis 56
3.2.1 Images 57
3.2.2 Defining Spiral Arms 58
3.3 Star Formation & Gas Tracers in the Arm and Interarm Regions 59
3.4 The Star Formation Efficiency in the Arm and Interarm Regions 61
3.5 Molecular Gas Fraction 67
3.6 Conclusion 67

4 Testing Spiral Structure Theories 71
4.1 Introduction 71
4.1.1 Long-Lived Spiral Arms & Shock Triggered Star Formation 72
4.1.2 Method of Tamburro et al. 2008 75
4.1.3 Toy Model 76
4.2 Analysis 80
4.2.1 2D Cross-Correlation 80
4.3 Comparison with Tamburro et al. 2008 82
4.4 Fitting Offsets using the 2D Cross-Correlation 85
4.5 Angular Offsets with Other Tracers 89
4.6 Dispersion of Star Formation Tracers 93
4.7 Conclusion 97

5 Conclusions & Outlook 103
5.1 Secular Evolution 103
5.2 Star Formation & Spiral Arms 104
5.3 Towards an Understanding of Spiral Structure 105
5.4 Conclusion 107

Acknowledgments 109

Bibliography 111

List of Figures

1.1 Sketch of the Andromeda galaxy by Abd al-Rahman al-Sufi. 2
1.2 Sketch of the Whirlpool Galaxy, M51 2
1.3 Edwin Hubble's morphological classification system of galaxies. 3
1.4 Depiction of the orbit of an oval locus. 13

2.1 Rotation curves for simulation models. 26
2.2 Snapshots of the stellar component of simulation models. 27
2.3 Snapshots of torques on stars by stars. 27
2.4 Accuracy of torques from projected mass densities in comparison to the 3D potential. 29
2.5 The relative importance of torques exerted by stars, gas and dark matter. 31
2.6 The cumulative distribution of the ratio of the total torques on stars due to the stars compared to the total torques arising from dark matter and stars. 32
2.7 Fit of dark matter enhancement function on torque. 33
2.8 Torque and angular momentum flow profiles for simulations. 34
2.9 Mass maps and torque maps of M101. 37
2.10 Comparison of the mass density profiles using the mass maps made by a pixel-by-pixel method and that using a global mass-to-light ratio. 38
2.11 Mass maps after deprojection for the sample of 24 galaxies. 39
2.12 Comparison of the effect of the deprojection values measured from GALFIT to the literature values on the torque profiles. 43
2.13 Radial profiles of the torque for M100 using different mass maps. 45
2.14 Torque profiles of sample. 49
2.15 Mean torque profiles for the sample of galaxies. 50
2.16 Mean $\nu_{inflow} \cdot t_{Hubble}$ profile for the sample of galaxies. 50

3.1 Identification of arm and interarm regions. 60
3.2 Concentration of 3.6μm light, gas and SFR towards spiral arms. 62
3.3 The effect of spatial resolution on our estimates of interarm star formation tracers. 63
3.4 The effect of finite pointing errors on H_2 maps. 63
3.5 The SFE for H_2 for NGC 5194, NGC 628 and NGC 6946. 65

3.6 The median value of the molecular SFE at different radii in the arm and interam regions. 66
3.7 Distribtuion of the pixel-by-pixel molecular SFEs for the total image, arm and interarm regions. 66
3.8 Mean fraction of molecular gas (H_2/HI) in radial annuli in the arm and interarm regions. 68
3.9 Molecular gas (H_2/HI) as a function of the total gas surface density in the arm and interarm regions 68

4.1 Illustration of the ordering of gas and stars in a long-lived spiral structure and results of a simulation showing the ordering of stellar cluster ages. 74
4.2 Toy model properties showing the rotation curve, azimuthal offsets and relative positions of star formation tracers in the spiral arms. 78
4.3 Model of the azimuthal profiles of star formation tracers and the correlation functions. 79
4.4 Sample of 12 galaxies. 81
4.5 HI Emission of NGC 5194 in polar coordinates. 83
4.6 Radial profiles of the angular offsets based on the location of the peak of the cross-correlation function between HI and 24μm versus radius. 86
4.7 Cross-correlation functions $cc(l)$ as a function of azimuth offset for NGC 5194. 87
4.8 Cross-correlation functions $cc(l)$ as a function of azimuth offset for NGC 3627. 88
4.9 Comparison of the offsets found by T08 and the offsets measured in this study. 89
4.10 The effect of spatial resolution on the autocorrelation function of HI maps at two different resolutions. 90
4.11 The effect of spatial resolution on the $cc(l)$ function using HI and 24μm images. 91
4.12 2D Cross correlation coefficients for a range of $t_{HI \rightarrow 24\mu m}$ and R_{cor} 92
4.13 H_2 as traced by CO emission of NGC 5194 in polar coordinates with contours of the 24μm emission overlaid. 94
4.14 Radial profiles of the angular offsets based on the location of the peak of the cross-correlation function between H_2 and 24μm versus radius. 94
4.15 Radial profiles of the angular offsets based on the location of the peak of the cross-correlation function between H_2 and the SFR as traced by a combination of 24μm and UV emission versus radius. 95
4.16 Radial profiles of the angular offsets based on the location of the peak of the cross-correlation function between the SFR as traced by a combination of 24μm and UV emission and the 3.6μm emission versus radius. 96
4.17 Fit of spiral arms in NGC 628. 98
4.18 Fit of spiral arms in NGC 5194. 98
4.19 Azimuthal profiles of star formation tracers for NGC 5194. 99
4.20 Azimuthal profiles of star formation tracers for NGC 628. 99

4.21 Distribution of stellar cluster ages in the spiral arms of four simulations. 101

List of Tables

2.1 Simulation Model Properties 26
2.2 Properties of 24 Sample Galaxies 35
2.3 Comparison of Deprojection Parameters 42

3.1 Sample Properties for Arm and Interarm Star Formation Study 57

4.1 Properties of 12 Sample Galaxies 82

Chapter 1

Introduction

Spiral galaxies are some of the most beautiful objects in the Universe with their eponymous structure that is both captivating and mystifying. Like our own Milky Way and our nearest spiral neighbour, the Andromeda galaxy, spiral galaxies consist of a disk made up of stars, gas and dust that exhibit a range of spiral patterns of varying complexity. There have been a tremendous number of studies which have sought to explain the formation, evolution and persistence of spiral structure and much of the details remain unresolved.

The existence of spiral structure invites us to apprehend its ramifications on the observable properties of the host galaxy. The non-axisymmetric structure of spiral arms may lead to gravitational scattering of stars and to angular momentum transport in the disk. In the inner disk, spirals and bars may also help feed black holes. Beyond these dynamical effects, spiral arms are also known to be important sites of star formation. Increased rates of star formation in the arms leave behind magnificent spiral patterns of bright, young stars, gas knots and dust lanes.

This thesis is an inquiry into how spiral structure affects its host galaxy both in terms of disk dynamics and star formation. We first provide some historical background followed by a review of the fundamentals of galaxy formation and of spiral galaxy properties. We then examine theories put forth to explain star formation, spiral structure and disk dynamics, three pieces of the puzzle, which we will find are intimately related.

1.1 Island Universes

The first sightings of spiral galaxies outside our own date back to the 10th century by the Persian astronomer, Abd al-Rahman al-Sufi, who identified the Andromeda galaxy, as a 'small cloud' (see Figure 1.1). Andromeda was later rediscovered by Simon Marius in 1612. It took almost a millennium though, after the development of sufficiently large telescopes, before features in these 'clouds' became apparent. William Parsons, the third Earl of Rosse, built a 1.8 m telescope in 1845, which remained the largest in the world for over seventy years (Binney & Merrifield 1998, hereafter BM98). With it, he identified and sketched two types of nebulae, those with elliptical, symmetrical distributions of light and those with spiral features, including a famous

Figure 1.1: Sketch of the Andromeda galaxy (red cloud) in Cetus, from "The Constellations" by Abd al-Rahman al-Sufi first published in 964. This image is from a copy made in 1417. *Image Credit*: World Digital Library, http://www.wdl.org/en/

sketch of the Whirlpool Galaxy (see Figure 1.2). The identification of spiral features in some of these objects supported Immanuel Kant's hypothesis that these nebulae, which Kant believed were 'island universes' like our own Milky Way, were rotating about an axis perpendicular to their plane.

At the turn of the century, both the nature of these nebulae and in particular their distance were not known and hotly debated. The discussion culminated in the *Great Debate* in 1920 between Shapeley and Curtis at the National Academy of Science in Washington, D.C.. Shapeley defended that the nebulae were part of our Galaxy, while Curtis supported Kant's hypothesis that these objects were extragalactic. The details of both of their arguments proved to be inaccurate and it was only in 1923, when Edwin Hubble used Cepheid variables to determine the distances to these objects via the period-luminosity relation, that the spiral nebulae were shown to be 'island universes' (BM98). We have since uncovered that galaxies are far from being isolated, 'island universes', as almost all galaxies undergo mergers and interactions.

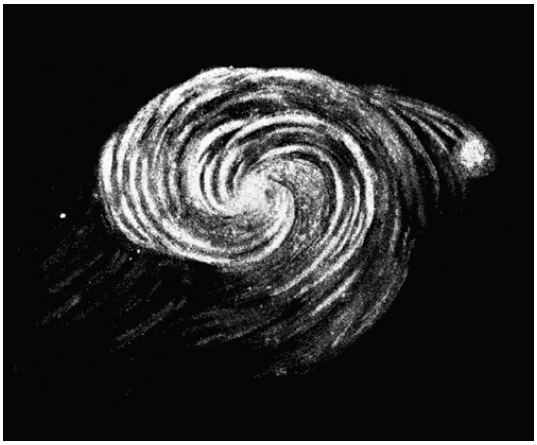

Figure 1.2: Sketch of the Whirlpool Galaxy, M51, by Lord Rosse, the first astronomer to discern spiral structure. *Image Credit*: Wikipedia, http://en.wikipedia.org/

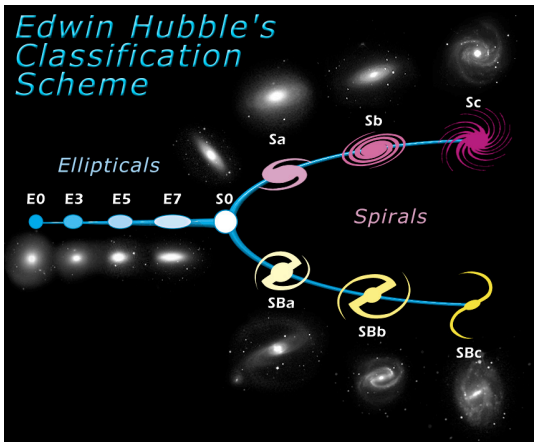

Figure 1.3: Edwin Hubble's morphological classification system depicting elliptical galaxies (left) and spiral galaxies (right) divided into barred spirals (top fork) and unbarred spirals (bottom fork). The elliptical galaxies are divided based on their ellipticity, while the spiral galaxies are grouped according to how tightly wound the arms are. *Image Credit*: NASA, ESA, http://www.spacetelescope.org/

Hubble continued to make important advances in our understanding of galaxies. The Hubble Sequence is still the most common classification scheme of galaxies and presents the galaxies as "a sequence progressing from globular masses of unresolved nebulosity to widely open spirals whose arms are swarming with stars" (Hubble 1926). The classification scheme was seen as an evolutionary progression from ellipticals, or early-type galaxies, to spirals, or late-type galaxies (see Figure 1.3). Of course, today the sequence is known to be reversed, with blue, spiral galaxies merging to form larger ones and eventually depleting their gas reservoir to form red, elliptical galaxies. However, the terms late-type and early-type are still in use today. Hubble's classification scheme has uncovered a number of important correlations. Properties, including the amount of gas and dust, the ability to resolve the arms into stars and HII regions and the bulge-to-disk ratio all correlate well with Hubble Type (*e.g.* van den Bergh 1960; Kennicutt 1982). However, many other important properties of spiral galaxies, including luminosity and mass do not correlate well, or only weakly (*e.g.* Kennicutt 1981; Kennicutt 1982; Bothun 1982). While our understanding of galaxy morphology has certainly come along way with the advent of new technology and larger telescopes capable of probing different wavelengths, the answers to many fundamental questions continue to evade us.

1.2 Disk Galaxy Formation

In recent years, the combination of increased precision in the measurements of cosmological parameters, as well as significant breakthroughs in observations and simulations, have allowed us to make important advances in understanding galaxy formation.

The framework in which most galaxy formation models are based consists of two key components to describe the evolution of the Universe and the structures within. Firstly, the Big Bang

theory predicts an expanding, initially smooth Universe. Structure in the Universe originates from early quantum fluctuations. Gravitational amplification through clustering and merging then leads to the subsequent growth of these perturbations. Secondly, the cold dark matter model (CDM), in which baryons contribute only a small fraction of the total mass of the Universe in comparison to dark matter, accounts for nearly all observations of the large-scale structure of the Universe (Peebles 1982; Blumenthal et al. 1984; Davis et al. 1985).

Despite the fact that the nature of dark matter is still unknown and that candidate particles have yet to be detected, there is overwhelming support for the CDM model of the Universe. The COBE and WMAP satellites, and soon the Planck satellite, have measured the temperature anisotropies of the cosmic microwave background (CMB), which are linked to the initial density perturbations in the early Universe (Planck: The Planck Collaboration 2006; WMAP: Bennett et al. 2003a; COBE: Boggess et al. 1992). Galaxy surveys like the two degree Field Galaxy Redshift Survey and the Sloan Digital Sky Survey (SDSS) have provided measures of the galaxy distribution and the power spectrum of galaxy clustering in agreement with the CDM model (2dFGRS: Cole et al. 2005; SDSS: Abazajian et al. 2009).

Simulations and analytical studies are typically used to trace the formation of galaxies using the CDM model. The first step in this process involves defining the cosmological parameters, including the density of matter, density of baryons and the amplitude of the density fluctuations. These parameters uniquely determine the power spectrum of the initial density perturbations. The spectrum is such that the largest amplitudes are on small scales. This means that small structures develop first and gradually merge to form larger structures and galaxies. The formation of bound halos is the starting point for all galaxies. The mass distribution of the halos, their formation history or merger tree and their internal structure, including their angular momentum and radial density profiles, are central to the development of the observed properties of galaxies.

In the standard picture of galaxy formation developed by Fall & Efstathiou (1980) , the disk of the galaxy forms out of collapsed gas in the halo, conserving its specific angular momentum. Tidal torques due to nearby structures are thought to provide this angular momentum, which is necessary for rotation (Peebles 1969). Because cooling rates are proportional to the square of the density, gas preferentially cools in the centre of dark matter halos. Once the density of the baryons is high enough, they decouple from the dark matter and hydrodynamic effects become important (Dalcanton et al. 1997; Mo, Mao & White 1998). The dark matter halo cannot dissipate energy and the collapse halts when it reaches the virial stage. Due to angular momentum conservation, the disk matter does not condense all the way to the center, but rather settles into a cold, rotationally supported disk. The cooling of the gas is also essential for star formation, which leads to the formation of the disk and bulge.

The subsequent evolution of galaxies is a complex process involving angular momentum redistribution, star formation, chemical evolution, feedback and further galaxy mergers. As we saw in the previous section, historically galaxies were grouped according to their morphology into two main groups: ellipticals, which are spheroidal in shape, and spirals, which are rota-

tionally supported disk galaxies. Today, it is common to divide these galaxies based on their color and location in the color magnitude diagram. The elliptical galaxies form much of the *red sequence*, which have a tight correlation in the color and magnitude diagram and the disk galaxies form the *blue cloud*, which have a broader distribution. The bimodality in color is largely a reflection of the star formation history, with the red galaxies no longer forming stars, in contrast to the blue, star forming galaxies (*e.g.* Strateva et al. 2001; Baldry et al. 2004; Bell et al. 2004). It is the merger of galaxies which takes them from the blue cloud onto the red sequence, by disrupting their morphology and quenching star formation (*e.g.* Barnes & Hernquist 1996; Naab & Burkert 2003; Bell et al. 2006; Cox et al. 2006; Skelton et al. 2009).

In this work, we focus on disk galaxies that populate the blue cloud. We now examine in greater detail the general properties of these star-forming galaxies.

1.3 Spiral Galaxies, the Interstellar Medium & Star Formation

The defining feature of spiral galaxies is their stellar disk. The stars and gas follow circular orbits in the thin disk with relatively little random motions. This cold medium plays an important role in determining the spiral structure of galaxies. It is responsible for producing stars and for maintaining the stability of the disk.

Empirically, it has been shown that the light distribution of galaxies is exponential (*e.g.* de Vaucouleurs 1959; Freeman 1970; Boroson 1981) and may extend over several disk scale lengths (*e.g.* Courteau 1996; de Jong 1996; Bland-Hawthorn et al. 2005). Spiral galaxies come in a range of structures from very compact to very diffuse and the central surface brightness is correlated to the disk scale length with physically larger systems having a lower central surface brightness. The gas disk typically extends much further beyond the stellar one and this has commonly been attributed to a star formation threshold, the critical gas density below which star formation ceases. However, many exceptions to simple exponential profiles exist, including the presence of rings and lenses and profiles, which require fitting with two or even three components (*e.g.* van der Kruit 1987; Erwin et al. 2005; Pohlen & Trujillo 2006; Athanassoula & Bosma 1985).

The greatest proportion of the mass budget of disk galaxies is not made up of stars, gas and dust, but rather the dark matter halo. Measurements of the 21-cm line of neutral hydrogen and optical emission lines allowed the rotation velocity of galaxies to be measured well-beyond their stellar disks (*e.g.* Rubin & Ford 1970; Rubin et al. 1980; Bosma 1981; Courteau 1997). Such measurements showed that most of the mass could not reside in stars alone, because the rotation curve did not rapidly fall off with radius, but rather remained flat. A flat rotation curve means the mass surface density must vary as r^{-1}. If the radial distribution of the luminosity is exponential, this means that the mass-to-light ratio in disk galaxies must increase to values over 100 in the outer parts (Athanassoula 1984, hereafter A84). Thus, at large radii, the mass of the galaxies is dominated by dark matter and, in total, is roughly 10 times the stellar mass.

The measurements of the circular velocity of disk galaxies, which are typically between 100 and 300 km s^{-1}, also lead to the important observation that the rotation speed of galaxies is tightly coupled to their luminosity via the Tully-Fisher Relation (Tully & Fisher 1977). With a measure of the magnitudes of galaxies, this relation has been used as an important means of determining distances.

Most disk galaxies contain a bulge, a central concentration of stars, which deviates from the exponential profile and can vary in appearance from elliptical to box-shaped. The elliptical bulges are known as classical bulges and, like elliptical galaxies, they are thought to have formed via mergers. The more disk-like bulges are called "pseudo-bulges" and are thought to be the result of dynamical processes during the secular evolution of the galaxy and are typically associated with bars (Kormendy & Kennicutt 2004; Kormendy & Fisher 2005). Indeed there is a correlation between bulge size and bar length (Athanassoula 1980; Gadotti 2010). Bars are very common in disk galaxies with over 70% of disk galaxies having bars when imaged in the infrared (Eskridge et al. 2000). The connection between bars and spiral structure is a complex one and as we will see in §1.4, bars may also drive the formation and persistence of spiral structure.

The Hubble classification scheme distinguishes spiral galaxies based on the presence of bars (*SB*'s) and on the degree to which the arms are wound (see Figure 1.3). As one progresses from *a* to *d*, the arms become more open. Many of the observable properties of spiral galaxies are well-correlated along the Hubble Sequence. As one progresses from *Sa*'s to *Sd*'s the luminosity of the bulge decreases, the gas fraction increases and regions of recent star formation become more prominent (A84).

One of the most important indicators of the structure and dynamics of disk galaxies is the interstellar medium (ISM). The ISM is the space between the stars in galaxies and is comprised of a mixture of multi-phase gas and dust. While it makes up less than 15% of the mass in galaxies, it plays a defining role in shaping the observable properties of galaxies. Not only is it the site of star formation, it also affects the stability of the disk[1] and exchanges matter and energy with the stellar environment. As such, it plays a central role in the formation of spiral structure.

The interplay between spiral structure, the ISM and star formation is certainly a complex one, because the processes controlling them are tightly coupled. Spiral structure can have very obvious effects on star formation and may even be a result of star formation, as we will see in §1.4. It also serves to reorganize the ISM, and due to this, the ISM has been relied upon as the primary source of observational tests to elucidate spiral structure and decipher between the competing theories of spiral arm formation. Thus, before examining how spiral structure forms, we first briefly review the main components of the ISM and the dominant theories of star formation.

[1]Because it is a cold, dissipative component, the gas acts to destabilize the disk by making the effective Q parameter smaller.

1.3.1 Components of the ISM

The most important and by far the most dominant component of the ISM is hydrogen, which is found in molecular, atomic and ionized forms. Due to this, the ISM is typically divided based on these phases. We briefly discuss the properties of each component, how they are detected and highlight specific qualities that are of use in our discussion of star formation (see Young & Scoville 1991; Ferrière 2001; Larson 2003; Tielens 2005; McKee & Ostriker 2007; Koda 2008 and references therein for more details).

Hot Ionized Medium (HIM)

Hot ionized gas is heated to high temperatures exceeding 10^6 K by supernovae shocks. It has a low density of less than 0.003 cm^{-3} and is organized into bubbles or fountains correlated with supernovae. It is typically observed via the X-ray spectrum of the hot plasma.

Warm Ionized Medium (WIM)

Warm ionized gas forms a diffuse medium between 6000-12000 K with a density of 0.1 cm^{-3}, which has been heated by the UV emission of massive O and B stars. While this component is mostly diffuse throughout galaxies, it also is locked into higher density HII regions. The WIM can be probed by measuring optical emission lines like the Balmer series of hydrogen. Hα is one of the most important lines and is due to the emission of a photon from an electron cascading from the n=3 to the n=2 state.

Hα emission is a powerful probe of the star formation rate in galaxies. The Hα emission is directly related to the number of ionizing photons produced by the massive, young stars and thus we can infer the rate at which these massive, young stars are forming by making some assumptions about their spectral type distribution. With the rate of massive star formation and knowledge or estimates of the initial mass function, one can determine the global star formation rate. An alternative to measuring Hα emission, is to measure the UV emission directly. However, dust extinction of the UV emission can have a strong effect, introducing uncertainties.

Warm Neutral Medium (WNM)

Neutral atomic hydrogen, HI, at temperatures of 8000 K, makes up about 30% of the volume of the ISM. HI cannot be optically observed, but fortuitously the ground state of hydrogen is split into two hyperfine levels by the interaction of the spins between the electron and proton. The transition between these two energy levels gives rise to the 21-cm emission line, which has become a powerful tool for mapping our Galaxy and others. The 21-cm line gives the total HI column density at a given location. Integrating over the surface area of the galaxy, one can determine the total atomic hydrogen content. As we noted earlier in §1.2, the shape of the 21-cm line also allows the rotation curve of a galaxy to be measured.

Cold Neutral Medium (CNM)

Cold neutral atomic hydrogen at temperatures of 80-100 K occupies only a small fraction of the volume of the ISM (1-4%). It is found in dense filaments and sheets (50 cm^{-3}) and is traced by absorption lines in the optical and the UV spectrum of distant quasars or bright stars. This cold phase exists in thermal pressure balance with the warm phase.

Molecular Clouds

Molecular clouds are comprised of H_2 gas at low temperatures (10-20K) and high densities ($>$ 100 cm^{-3}). Thus, while H_2 makes up 30% of the mass of the ISM, it only makes up 0.05% of the volume. Most molecular clouds are gravitationally bound and the densest cores are likely gravitationally unstable, making them the future sites of star formation. Unfortunately, H_2 is a homonuclear molecule, so it has no permanent electric dipole moment. CO has a net dipole moment allowing it to radiate when it spins. CO emission traces the amount of H_2 molecular clouds and not the diffuse molecular gas, because very high densities are required for its excitation ($>$ 300 cm^{-3}). Since stars form out of dense gravitationally bound molecular clouds, CO measurements should correlate very well with the star formation rate. Using a conversion factor, CO emission at the 1.3 mm (J=2$\rightarrow$1 transition) and 2.6 mm (J=0$\rightarrow$1 transition) wavelengths are used to measure the density of giant molecular clouds.

Dust

Mixed in with these gas phases, is a solid dust phase with grains that range in size from fractions of a micron to clumps of 50-100 atoms. These larger clumps are likely molecules or polycyclic aromatic hydrocarbons (PAHs). The grains absorb blue and UV light with wavelengths close to the grain size. They then re-emit this radiation via blackbody radiation in the infrared and mm wavelengths. As we saw before, UV emission suffers from dust obscuration, making it less reliable as a star formation tracer. However, a combination of infrared emission and UV emission is an alternative. Unfortunately, not all dust is heated by young stars. Widely distributed grains can also be heated by ambient stellar light. The emission from such grains is typically referred to as diffuse or cirrus emission and complicates accurate measures of the star formation rate.

Dust plays an important role in the chemistry of the ISM by acting as sources and sinks for the gas phase. In cold, dense regions, they accrete gas and in hot regions, they shed their mantle, which releases the gas phase. Dust grains also serve as catalysts for the formation of molecular hydrogen by allowing the hydrogen atoms to combine on their surface.

1.3.2 Star Formation

Having examined the gas phases of the ISM and how certain tracers can be used to measure star formation rates, we now review the process of star formation and the empirical observations of star formation rates in galaxies.

The process of star formation begins when massive bound structures form out of the diffuse ISM due to gravitational instabilities, which may be caused by, but not limited to, perturbers like spiral arms. These structures ($>10^7 M_\odot$) fragment into giant molecular clouds (GMCs) of a range of masses. Supersonic turbulence within the GMCs creates a distribution of gas condensates, the densest of which are self-gravitating cores and sites of future star formation. Core collapse leads to star formation and depends on a variety of processes including gas accretion, magnetic forces, winds and radiation. When massive stars form they ionize their surroundings into HII regions, which energizes surrounding GMCs and eventually destroys them through photoevaporation. For this reason, star formation is a highly inefficient process with a mean cloud efficiency of only 5% over the cloud lifetime. The return of the GMC gas to the diffuse ISM allows this process to begin anew (McKee & Ostriker 2007).

Star formation and its connection to the observable properties of galaxies is not yet at the level where we can examine the scales described above. Rather than the small scale physical processes, the star formation rate (SFR) in galaxies is studied via gross characterizations and phenomenological descriptions. The star formation rate is believed to be controlled by at least two factors: the local gas density and the dynamical properties of the disk. The SFR is almost always described by a set of empirical laws, which have provided an important framework for analytical models and numerical simulations, and we now examine their formulation and implications.

Star Formation Laws

The SFR is almost always described by two empirical laws put forth by Kennicutt (1998) as an extension of the formulations of Schmidt (1959) and Sanduleak (1969). The seminal paper of Kennicutt (1998) on star formation in gas-rich environments combined observations of Hα, HI and CO distributions of spiral and starburst galaxies and uncovered a tight correlation between the gas surface density, Σ_{gas} and SFR per unit area, Σ_{SFR}. The so-called *global Schmidt law* applies for disk-averaged quantities and is a power law of the form:

$$\Sigma_{SFR} = A\Sigma_{gas}^{N}, \tag{1.1}$$

where the normalization, A, and the slope, N=1.3-1.5, is remarkably consistent from galaxy to galaxy. The same law appears to hold locally for azimuthally averaged gas densities and star formation rates. However, the normalizations and slopes vary from galaxy to galaxy.

The second empirical law is that of a star formation threshold either at a gas column density of 5-10 $M_\odot pc^{-2}$ or a threshold ratio of gas surface density to the critical density for the Toomre (1964) gravitational instability with,

$$\alpha_Q = \frac{\Sigma_{gas}}{\Sigma_{crit}} = 0.69 \pm 0.20. \tag{1.2}$$

The critical column density of the gas, Σ_{gas} is that density which overcomes the Coriolis

and pressure forces and allows the gas to collapse and form stars. The Toomre (1964) criterion for the critical gas density may be expressed as:

$$\Sigma_{crit} \approx \frac{\sigma_{gas}\kappa}{\pi G}, \tag{1.3}$$

where σ_{gas} is the radial velocity dispersion of the gas and κ is the epicyclic frequency of the stars and gas.

While many galaxies seem to obey these empirical laws, there are exceptions and more recently it has become clear that this picture is more complex. Several studies have questioned the existence of a clear threshold (*e.g.* Boissier et al. 2003) and others have shown that different slopes at low gas densities may be required (Bigiel et al. 2008). High redshift studies (z $>$ 3) have shown much steeper slopes in general and lower normalization amplitudes.

In order to understand these empirical observations, a variety of models have been put forth, which can be differentiated by the mechanisms they employ to determine the timescale over which gas forms stars. The simplest versions argue that the SFR scales to the free-fall time in the gas disk (Kennicutt 1989). It is also common to scale the SFR with the local orbital time scale (*e.g.* Kennicutt 1998; Wong & Blitz 2002) or the dynamical timescale which sets the rate of collision between gravitationally bound clouds (Tan 2000).

Recent advances in HI, CO and infrared imaging have allowed for spatially resolved measurements of the kinematics, gas and stellar surface densities and the SFR surface density across optical disks (*e.g.* Bigiel et al. 2008; Leroy et al. 2008). These studies show that star formation correlates strongly with molecular gas and that one should expect a fixed SFR per unit molecular gas, SFE(H_2)=SFR/M(H_2), which supports theories that have posited a fixed GMC efficiency (*i.e.* Krumholz & McKee 2005; Gnedin & Kravtsov 2010). For a range of parameters, including galactocentric radius, stellar and gas surface density, orbital timescales, pressure and the slope of the rotation curve, the SFE(H_2) is found to be constant to first order (Leroy et al. 2008). Thus, the relationship between the star formation rate density and gas density varies depending upon the fraction of molecular gas.

1.4 Spiral Arms: their Formation, Persistence and Effects

The history of our quest to understand spiral structure has been fraught with many divergencies and has followed a winding path almost in homage to the structure itself. The early work of Bertil Lindblad between 1920 and 1940 developed the basic foundations of stellar kinematical theory which provided a framework for his and other theories of spiral structure. Owing in part to the lack of observational support, his theories only became appreciated much later. In the 1960s, spiral structure garnered much attention and much of our current understanding of this subject stems from this time. An excellent review of the history of the field can be read in Pasha (2004a & 2004b). The following summary does not attempt to explain in great detail all of these theories, but rather focuses on the key points necessary to understand this work. It is largely

based on comprehensive reviews in A84, Bertin & Lin (1996, hereafter BL96) and Binney & Tremaine (2008, hereafter BT08).

1.4.1 Basic Properties

While the Hubble Sequence (see Figure 1.3) is certainly the most widely used classification system for spirals, there are other schemes (*e.g.* van den Bergh 1960a and 1960b : Elmegreen & Elmegreen 1982) which differentiate spirals based on the degree to which their arms are developed and may be more directly coupled to the way in which the pattern forms. Galaxies with a clear, coherent, bright and typically two-arm spiral pattern are called *grand-design* and are distinguished from *flocculent* galaxies that have a more patchy, filament-like structure. Most grand-design spirals (at least 70%) are found in groups or pairs and almost all exhibit a bar. As we shall see, bars and companions may play an important role in driving spiral structure.

In order to trace spiral arms and determine their strength, the surface brightness is typically expressed as a Fourier series (*e.g.* BT08; A84; Rix & Zaritsky 1995):

$$\frac{I(R,\phi)}{\bar{I}(R)} = 1 + \sum_{m=1}^{\infty} A_m(R)\cos m[\phi - \phi_m R](A_m(R) > 0), \tag{1.4}$$

where $\bar{I}(R)$ is the azimuthally averaged surface brightness at radius, R, and A_m and ϕ_m are the amplitude and phase of the mth Fourier component. The m=0 component has no phase associated with it and reflects the mean surface density in the annulus. The most dominant phase in grand-design spirals is the m=2 component, which reflects the two-armed spiral.

Almost all spiral galaxies are known to be trailing spirals, which means the tips of the arms point in the opposite direction of rotation. The degree to which the arms are wound is defined by the pitch angle, which is the angle formed between the tangent to the spiral and a circle centered on the center of the galaxy.

The primary difficulty in understanding how spiral arms form is that there is no unique way of describing them. The simplest way to describe spiral arms is that they are *material*. As we have seen, the rotation curve of galaxies remains constant over much of the disk, which means that the disk is in differential rotation. This observation has important consequences for spiral structure. Imagine a series of flags along one diameter in the galaxy. Since the angular rotation rate is a decreasing function of R, trailing spiral arms will form. However, this kinematic shear will gradually decrease the pitch angle of the arms over time and the arms will wind up (BT08). This is typically referred to as the *tight winding dilemma*[1] (Oort 1962).

In order to resolve this, rather than seeing the spiral structure as being made up of material arms, we can see it as a manifestation of excess matter associated with a rotating pattern. This is what is known as the *density wave theory*. While other theories of spiral structure such

[1]It is important to note that this dilemma was a problem in the early studies of spiral structure. Today, there are spiral structure theories which posit transient, evolving patterns. These theories explain spiral structure as material arms that wind up and reoccur (Dobbs & Bonnell 2008; Dobbs et al. 2009)

as recurring gravitational instabilities may account for spiral arms, density wave theory has dominated the field for several decades. We briefly describe the key foundations of this idea before examining in greater detail the different possible variations and other theories which can be used to elucidate spiral structure (§1.4.2).

Our discussion depends on the assumption that the disk can be described by a continuous distribution of matter and that we can use the collisionless Boltzmann equation and Poission equation, relating the density and the potential (BT08).

It is important to realize that stellar orbits are not strictly circular. Rather, there are always some random motions which incur deviations from a circular orbit. We typically refer to such motions as radial oscillations or *epicyclic motions* about a circular orbit called the *guiding center*.

The circular orbit is described by the rotational velocity, V(r), and the respective angular velocity, Ω(r), such that:

$$\Omega = V/r \tag{1.5}$$

and

$$V(r) = (rd\Phi/dr)^{1/2}, \tag{1.6}$$

where Φ is the gravitational potential responsible for the centrifugal acceleration.

Due to conservation of angular momentum, if a star moves inward with respect to its reference radius it is then rapidly pulled back. The restoring force also works in the opposite direction if it moves outward. The net effect, if one is in the framework of the guiding center, is that the orbit makes a small ellipse retrograde to the rotation. The frequency of the oscillations is described by the epicyclic frequency, κ,

$$\kappa = 2\Omega[1 + \frac{1}{2}d\ln\Omega/d\ln r]^{1/2} \tag{1.7}$$

Only in the case where κ and Ω commensurate will the orbit be closed, otherwise, in the non-rotating frame, the star moves in an open rosette pattern. These epicycles allow us to derive what is known as the *kinematical spiral wave*.

Consider a galaxy in rotation with an angular velocity, Ω, and stars moving in an oval orbit (see Figure 1.4). Due to the epicyclic frequency of the stars, the image of the oval or the *locus* of the oval moves more slowly than the stars. The precession of the oval is $\Omega - \kappa/m$, where m is an integer which defines the symmetry or, in this case, the number of arms. If a series of ovals are nested, a spiral pattern develops, since the ovals would each be turned by an angle (Toomre 1977). The density at each orbit would be proportional to the distance between the two neighboring orbits. The speed at which the oval appears to move is called the pattern speed Ω_p. For a two-armed spiral, the pattern speed is expressed as:

$$\Omega_p = \Omega - \kappa/2. \tag{1.8}$$

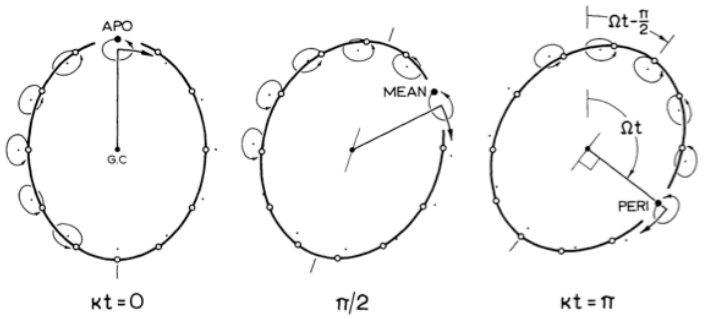

Figure 1.4: Depiction of the orbit of an oval locus, which is advancing more slowly than the orbiters (Figure 2 from Toomre 1977). The orbiters have a mean angular speed, Ω, in the clockwise direction. They also move in small epicycles counterclockwise with a frequency, κ. The precession rate of the oval is thus, $\Omega - \kappa/2$.

If this quantity were independent of radius, the spiral pattern could exist indefinitely.

At this point, it is useful to note three important frequencies, ν, for which the orbits are closed. Note that these frequencies can be derived without requiring the kinematic wave scenario as they can be derived for any perturbation of an axisymmetric background. For brevity and ease of explanation we present them here. The frequencies are described by the pattern speed and epicyclic frequency such that $\Omega(r) - \Omega_p$ and κ(r) are commensurable,

$$\nu = \frac{m(\Omega_p - \Omega)}{\kappa}. \tag{1.9}$$

At the so-called *corotation radius* $\nu = 0$, the pattern and the stars orbit at the same angular speed. In the rotating frame, the stars simply make small ellipses with frequency κ. Inside this radius, the pattern rotates slower than the disk and the *inner Lindblad resonance* occurs when $\nu = -1$. Beyond corotation, the pattern rotates faster than the disk and at $\nu = 1$ the *outer Lindblad resonance* occurs. The existence and location of these resonances depend on the rotation curve and pattern speed.

While at first this kinematic picture seems a satisfying solution to the *winding dilemma*, one quickly realizes that it falls short of a complete picture. It too would rapidly disappear unless $\Omega - \kappa/2$ were precisely constant. Furthermore, the self-gravity of the arms has been neglected and the shape of the arms would be completely arbitrary since the position angle of the ovals is arbitrary. Thus, we now turn our analysis to a more complete picture.

1.4.2 Theories of Spiral Structure

At some level the presence of spiral structure is not hard to understand. Patches of star formation can easily be sheared into a spiral-like structure by local gravitational instabilities (BT08). Such a process might explain *flocculent* spiral galaxies, which have short, fragmented arms (Elmegreen & Elmegreen 1984) and high-resolution galaxy simulations typically exhibit such spiral structures (Li et al. 2005). What is more difficult to understand are coherent spiral arms

that extend over a large portion of the galaxy even beyond the optical disk to the outer gaseous disk, as in grand-design spirals (Oort 1962; Bertin & Amorisco 2009). In some cases, this can be attributed to tidal effects either due to a nearby companion like M51 (Toomre & Toomre 1972; Dobbs et al. 2010) or a bar (Elmegreen & Elmegreen 1982). Indeed it has been proposed that all grand-design spirals form in this way (Kormendy & Norman 1979; Bottema 2003). However, the ease of their development in simulations without such perturbers suggests that spiral structure can be self-excited (Sellwood 2010).

Typically self-excited models for spiral structures can be divided into two groups based on the longevity of the spiral pattern. A long-lived quasi-stationary spiral structure that depends on density wave theory has been developed largely using analytical studies. The spiral features are attributed to quasi-steady global modes of the disk (*e.g.* Lin & Shu 1964; BL96). The other approach, which has largely been based on simulations, purports that spirals are short-lived, recurrent transient patterns that originate from recurrent gravitational instabilities. We briefly summarize these two positions as well as their possible implications.

Long-Lived, Quasi-Stationary Spirals

First developed by Lin & Shu (1964, 1966) and extended by Lynden-Bell & Kalnajs (1972) and Bertin et al. (1989a, 1989b), this theory is based on density wave theory and maintains that spirals are global instabilities that grow slowly in a cool disk with a smooth distribution function. The main assumption is that the spiral pattern rotates at a constant pattern speed with little evolution. The gravitational attraction of the stars and gas at different radii act to offset the kinematical spiral from winding up and the pattern grows. The spiral pattern develops in the following sequence of events. A growing spiral pattern develops in an unstable disk, the pattern that emerges is a reflection of the most unstable mode. The wave builds and shocks the gas, which dampens the wave. Eventually, the damping and the growth rates are equal and the pattern is in a stable state (BT08). The model requires a dynamically cool outer disk and a hot inner region. In order for the gravitational attraction of the stars and gas to reinforce the pattern, it is usual to assume that the arms are tightly wound. A proper calculation of the modes requires lengthy mathematics involving a system of the linearized Boltzmann and Poisson equations with proper boundary conditions. We defer the reader to BT08 and BL96 for the mathematical description of this process. Density wave theory is appealing because, since density waves propagate radially, the spiral patterns seen in grand-design galaxies can correspond to a global, long-lasting spiral mode with a single pattern speed. In order to have a single pattern speed however, the waves must propagate back and forth between the inner and outer Lindblad resonance. The major problem with density theory is that it fails to show how this happens (Dobbs et al. 2010). Almost all spirals are *trailing* which means that structures can only move inwards within corotation and outwards beyond. Thus, observed spirals show no obvious mechanism for the propagation of these waves.

Density wave theory accurately predicts several observed properties of spiral galaxies (BT08)

including a smooth, broad pattern over much of the disk and in all wave bands. The presence of the pattern in all wave bands, including the redder bands which best probe the stellar mass density, supports this theory because a density wave should incur the participation of the whole disk. Due to the supersonic relative velocity between the pattern and the disk, shocks should lead to the rapid triggering of star formation in the arms (Roberts 1969). Thus, one expects bright stars to be observed downstream from the arms and this has been noted in several cases (*e.g.* Tamburro et al. 2008; Egusa et al. 2009). However, since many of these observations could also be predicted by other theories, observations confirming the finer details of this picture including pattern speeds and the locations of corotation and resonances have been sought. Unfortunately, these basic parameters have proven difficult to uncover (Sellwood 2010). Furthermore, N-body simulations, even with an ever increasing resolution, do not develop stationary spiral patterns. Indeed, the alternative picture, which we now describe, was largely formulated using N-body simulations.

Short-Lived, Recurrent Spirals

Early studies supporting the idea of transient spirals were put forth by Goldreich & Lynden-Bell (1965) and Julian & Toomre (1966) and Toomre (1981). While disk shearing and triggering by companions can describe transient spirals, *swing amplification* of a small perturbation (or noise in the case of simulations) (Toomre 1981) could also be a means to create spiral patterns.

Disks are stabilized on small scales by random motions and on large scales by the disk rotation. The stability of the disk is typically expressed in terms of the Toomre Q instability criterion, which is an extension of the Jean's instability criterion for a two-dimensional, rotating system. For a stellar disk, this criterion is expressed as:

$$Q \equiv \frac{\sigma_R \kappa}{3.36 G \Sigma} > 1, \tag{1.10}$$

where σ_R is the radial velocity dispersion, κ is the epicyclic frequency, G is the gravitational constant and Σ is the surface density.

If the random motions are temporarily suppressed, a small perturbation can be swing amplified. A density wave is first excited by epicyclic motions in the disk. The wave is initially a leading spiral, which is rapidly sheared into a trailing spiral by differential rotation. In a stable disk, random motions would remove the overdensity before it had time to collapse. In this case, however, the wave is amplified by a modified form of the Jean's instability. The amplification depends on the stability of the disk, expressed by the Q parameter and a critical wavelength, which describes the shortest wavelength stabilized by rotation.

Early N-body simulations also showed spiral patterns being created and then rapidly dissolving (*e.g.* Hohl 1970; Efstathiou, Lake & Negroponte 1985). The spirals developed due to swing amplification of particle noise. However, the simulations showed the rapid dissolution of the spiral without any subsequent recurrence. The dissolution was caused by disk heating due

to rising random motions induced by the spiral perturbation (Sellwood & Carlberg 1984). By adding dissipative infalling gas, the pattern was found to reoccur. It was later shown that any cooling process could have this effect (*e.g.* Carlberg & Freedman 1985; Chakrabarti, 2008). Unfortunately, swing amplification is only convincing for the most chaotic and gas rich disks, which provide high enough seed noise. Observed spirals tend to have high arm amplitudes and clear symmetry, which doesn't match this picture (Sellwood 2010).

Sellwood and co-workers have recently developed a convincing picture of transient, recurring spiral patterns that has some agreement with observations as well as simulations. The central idea in their work is that stars are scattered at the main resonances in the disk. The scattered stars change the distribution function, which subsequently seeds the growth of a new instability. Thus, each wave provokes a new instability, which leads to an ever-changing spiral pattern (see Sellwood & Lin 1989; Sellwood & Carlberg 1984; Sellwood & Kahn 1991; Sellwood 2010). By analyzing the velocity distribution of F & G dwarfs in the Geneva-Copenhagen survey, Sellwood (2010) finds that there is evidence for scattering and trapping at resonances in a way predicted by this model.

It is clear that the debate between long-lived, quasi-stationary spirals versus short-lived, recurring spirals is one that will require careful observational analysis to settle. The situation is further complicated by the fact that recent studies have shown that spiral structure may be more complex than once thought, with spirals exhibiting multiple pattern speeds (Meidt et al. 2009). In this work, we focus primarily on the implications of the presence of spiral structure in disk galaxies. At the end we use observations to draw some inferences on which of these two pictures best predicts them.

1.4.3 The Effects of Spiral Arms

Having provided an overview of the formation and properties of spiral galaxies and spiral structure, we now turn to the focus of this thesis, which is to examine how spiral structure can affect the observable properties of disk galaxies. We will examine two primary means by which spiral structure can transform disk galaxies: secular evolution and star formation. We briefly describe each in turn.

Spiral Arms & Secular Evolution

While the early processes of disk assembly and mergers are central to producing many of the observed properties of disk galaxies, the later phases of galaxy evolution are dominated by the slower processes of secular evolution. Secular evolution refers to any gradual change in an isolated disk due to internal dynamical processes (BT08). Examples of such processes include the response of the disk to a growing black hole, gas inflow resulting from dissipation in the interstellar gas, the increase of random motions due to gravitational perturbers like molecular clouds, the development of the afore-mentioned 'pseudo-bulges' and the scattering of stars at resonances (BT08; Sellwood 2010).

Spiral arms may play a key a role in secular evolution processes. Like bars and other non-axisymmetric features, they can lead to angular momentum transport in the disk by exerting torques through their gravitational field. This angular momentum transport may have a number of effects, including redistributing matter in the disk and changing the mass density profile. In Chapter 2, we examine how strong such processes might be and whether they can significantly reshape galaxies within the galactic age ($\approx$ 10 Gyr).

Spiral Arms & Star Formation

Spiral arms are clearly important sites of star formation. The simple fact that we see spiral arms means that a high proportion of stars must be forming there. The connection between spiral arms and star formation is still not well-understood and is intimately connected to how spiral arms form and persist. In the case of flocculent galaxies, sheared patches of star formation may actually cause spiral arms to form. In grand-design spirals, the arms may simply act to reorganize the ISM and draw gas into the arms producing high gas densities, which then lead to the high star formation rates. If the quasi-stationary, long-lived, spiral structure theory is accurate, spiral arms should be sites of increased star formation efficiency. The supersonic relative velocity between the spiral pattern and the disk should cause shocks which could trigger the formation of molecular gas and stars. In this way, one would expect to see the different star formation tracers offset from one another, reflecting the sequence of events and their timescales.

These scenarios each predict different observable properties, which in the past, due to poor spatial resolution, have been difficult to measure. Recently, high-resolution maps of the gas and infrared emission have opened the door for better studies. In Chapter 3, we compare the arm and interarm regions of three spiral galaxies and examine whether spiral arms are more efficient at forming stars and molecular gas than the interarm regions. In Chapter 4, we look for evidence for the triggering scenario by examining offsets of star formation and gas tracers and the relative skewness of these tracers in comparison to the direction of rotation. We close in Chapter 5 with a brief summary and an outlook on the future directions of this work.

Chapter 2

Secular Evolution in Spiral Galaxies

This chapter is based on the paper "An Observational Estimate for the Mean Secular Evolution Rate in Spiral Galaxies" by K. Foyle, H.-W. Rix and S. Zibetti, published in MNRAS.

Abstract

We have observationally quantified the effect of gravitational torques on stars in disk galaxies due to the stellar distribution itself and explored whether these torques are efficient at transporting angular momentum within a Hubble Time. We derive instantaneous torque maps for a sample of 24 spiral galaxies, based on stellar mass maps that were derived using the pixel-by-pixel mass-to-light estimator by Zibetti, Rix and Charlot. In conjunction with an estimate of the rotation velocity, the mass maps allow us to determine the torque-induced instantaneous angular momentum flow across different radii, resulting from the overall stellar distributions for each galaxy in the sample. By stacking the sample, which effectively replaces a time average by an ensemble average, we find that the torques, due to the stellar disk, act to transport angular momentum outward over much of the disk (within 3 disk scale lengths). The strength of the ensemble-averaged gravitational torques within one disk scale length have a timescale of 4 Gyr for angular momentum redistribution.

The individual torque profiles show that only a third of our sample exhibit torques strong enough to redistribute angular momentum within a Hubble Time, mostly those with strong bars. However, advective angular momentum transport is another source of angular momentum redistribution, especially in the presence of long-lived spiral arms, but is not accessible to direct observations. The torque-driven angular momentum redistribution is thus observed to be effective, either in one third of disk galaxies or in most disk galaxies one third of the time and should lead to either changes in the mass density profile or the orbital shapes.

We use a set of self-consistent disk, bulge and halo simulated isolated disk galaxies with realistic cold gas fractions to verify that the torques exerted by the stellar distribution, such as spiral arms or a bar, exceed those of the gas and halo, as assumed in the analysis of the observations.

This study is the first to observationally determine the strength of torque-driven angular momentum flow of stars for a sample of spiral galaxies, providing an important empirical constraint on secular evolution.

2.1 Introduction

Three primary aspects control the observable features of present-day galaxies: (1) the particular density fluctuations from which they originated, (2) successive mergers and various interactions with the environment and (3) the (internal) secular evolution. While it is clear that the first and second point play a decisive role in shaping and reshaping a galaxy over time, the significance of the third mechanism continues to be debated. In particular, it has not been empirically demonstrated how effective gravitational torques (induced by non-axisymmetric features like bars and spiral arms) are at redistributing angular momentum, which can lead to re-shaping the dynamics and stellar density profile of a galaxy over time.

In this present study we develop a framework on how to combine simulations, 'stellar mass density' images of spiral galaxies and sample averaging to address this question. Specifically, we examine 24 galaxies with photometry from SDSS in order to assess how strong gravitational torques are at any given instant on the stellar distribution. Unless otherwise stated, we consider torques due to the stellar distribution acting solely on the stellar distribution. This modest galaxy sample serves to a) determine the limitations of both the method and the data; b) determine if gravitational torques are significant for a set of individual galaxies and c) explore how samples of galaxies should be 'stacked' in order to establish an average measure over time of the secular evolution for galaxy disks. In §2.2 we describe our motivation and in §2.3 we describe how the torques are calculated. Tests completed with N-body/SPH simulations are outlined in §2.4. The observations and analysis are described in §2.5 and §2.6 and §2.7 summarizes the conclusions.

2.2 Background & Motivation

Stellar bars and spiral arms are common in and eponymous for disk galaxies. Two key questions present themselves for the study of bars and spiral arms: a) why do these features exist and look the way they do? and b) given that we observe these features, what instantaneous effect do they have? In the present study, we focus on the second one. Previous studies have attempted to calculate the strength of bars and spiral arms and their role in angular momentum transfer. The early analytical calculations of Lynden-Bell & Kalnajs (1972) showed that a trailing spiral structure will lead to an overall outflow of angular momentum, and observations indicate that most spirals are trailing (*e.g.* de Vaucouleurs 1958; Pasha & Smirnov 1982 and Pasha 1985). Bertin (1983) derived a time scale for galaxy evolution due to a spiral mode from the angular momentum contained in the disk and the angular momentum flux. His work suggested a time scale which was an order of magnitude greater than a Hubble Time. However, he did not

use spiral arm parameters from observed galaxies, but rather chose what he presumed to be reasonable values for an average spiral.

Gnedin et al. (1995) (hereafter G95) pursued this further, using direct observations of M100 to construct a deprojected stellar mass map for this galaxy and calculate the torques. They found that if the instantaneously observed torques in M100 were to act over long periods, they would redistribute angular momentum on a timescale of 5-10 Gyr, *i.e.* they would re-shape the stellar distribution within a Hubble Time.

Torques exerted by the stars also act on the (cold) gas. Several studies have explored the effects of such gravitational torques exerted by stars on gas and used them to measure gas inflow rates in galaxies (*e.g.* Jogee et al. 2005; Hunt et al. 2008; Haan et al. 2009). In particular, Haan et al. (2009) has shown that gravitational torques are extremely efficient at redistributing cold gas and can act on a timescale of a few dynamical periods, 5×10^8 Gyr.

The problem in studying this effect in individual galaxies lies in the fact that we can only measure the instantaneous torques, but are interested in their long-term ($t_{dyn} \ll t < t_{Hubble}$) secular effect. Therefore, one would be forced to assume that the spiral and bar patterns seen today are typical of the past and future. However, for any given galaxy this is likely not the case.

Many people have turned to simulations since they allow us to follow a galaxy over time. Indeed many simulations (Zhang 1996, 1998, 1999; Debattista & Sellwood 2000 and Athanassoula 2002, 2003) have tried to address the strength and effect of bars and spiral arms over time. In a series of theoretical papers, Zhang showed that gravitational torques lead to stars being funneled inward within the corotation radius, moving outward beyond; for large spiral galaxies, $R_{co-rot} \approx 3\ r_{exp}$ (Kranz et al. 2003). The mass redistribution was shown to imply some development of the Hubble Sequence (Zhang 1996, 1998, 1999).

Following the analytical work of Lynden-Bell and Kalnajs (1972), Athanassoula (2002) used simulations to study the angular momentum transfer at resonances, specifically focusing on how the halo affects the amount of angular momentum transferred and subsequently the growth of the bar. These studies confirmed that within the inner Lindblad resonance, angular momentum is lost, while at corotation and the outer Lindblad resonance, angular momentum is gained.

The simulations of Sellwood & Binney (2002) and Roškar et al. (2008) showed that radial mixing due to angular momentum transfer occurs even in the case where little change is seen in the mass density profile. Disk stars were shown to migrate considerably over time due to resonant scattering. Therefore, the translation of angular momentum transport to changes in the stellar surface mass density profile is complex.

In general, angular momentum redistribution has been shown to lead to higher central mass density concentration, to the development of a two-component profile and the evolution of the inner disk scale length over time toward higher values (Debattista et al. 2006; Foyle et al. 2008).

While simulations and analytical studies have certainly provided much insight into the role

of resonances and angular momentum transfer, for our study we wish to focus on the strength of torques on stars by the stellar distribution itself and how these torques contribute to angular momentum transfer. For such a study, numerical simulations of disk galaxies are not ideal. The mass distribution and in particular the non-axisymmetric components (*i.e.* bars and spiral arms) are the key to the strength of the torques. Early numerical simulations have shown that spiral arms are transient features that dissipate after $\approx$ 10 rotations (Sellwood & Carlberg 1984). Even modern simulations that include many more physical processes confirm the short-lived and recurrent nature of spiral arms (Governato et al. 2007). However, as we saw in §1.4, it is unclear whether spiral arms are short-lived in nature. Lin & Shu (1964) and Bertin et al. (1989) have proposed long-lived spiral density waves.

Furthermore, an even greater challenge is that disk galaxy simulations embedded in a cosmological context are far from being able to produce realistic galaxies that match both the size-velocity-luminosity and color-luminosity relations (Courteau et al. 2007; Dutton et al 2007). These galaxies typically produce very high central mass concentrations due to angular momentum transfer (*i.e.* Navarro & Benz 1991; Navarro & White 1994; Navarro & Steinmetz 1999). In recent years, these cosmological simulations have greatly improved by including more physical processes and additional resolution (*i.e.* Thacker & Couchman 2001; Somerville 2002; Governato et al. 2007), but the problem is not fully resolved. In light of this, one can not rely on simulations alone to estimate the actual secular evolution rate in observed galaxies. Indeed, depending on the duration for which a simulation has run, simulations may show that the torques are either much stronger or weaker than those seen in nature. In our present study, we focus on a purely empirical assessment of the exerted torques and do not address the detailed physics of angular momentum transport. While we employ simulations, these are only used to provide mock observations to test various steps in our method and examine the effects of 'non-observables'.

In order to assess how important gravitational torques actually are for shaping galaxies over long times, studying individual galaxies is not ideal. In this case, in fact, we are forced to assume that for both the angular momentum, J and the torque, Γ, we have $J(R, t_{now}) \approx J(R, t_{later})$ and $\Gamma(R, t_{now}) \approx \Gamma(R, t_{later})$ respectively. G95 made this assumption, but acknowledged that the structure of the stellar distribution will change in any galaxy's past or future. For an ensemble of galaxies whose overall population properties are evolving slowly, we can say that $\langle J(R, t_{now})\rangle_{sample} \approx \langle J(R, t_{later})\rangle_{sample}$ and $\langle \Gamma(R, t_{now})\rangle_{sample} \approx \langle \Gamma(R, t_{later})\rangle_{sample}$. Thus, we propose to bypass this problem by averaging over a large sample of similar-sized galaxies not chosen based on similar spiral patterns or bar strengths. Bar and spiral arm features are not recent phenomena and many studies have found that the prevalence of bars and spiral features has not changed very much since z $\sim$ 0.7, a period that corresponds to $\sim$ 20 dynamical times for the half-mass radius of large disks (Jogee et al. 2005; Barden et al. 2005; Marinova & Jogee 2007 and Barazza et al. 2008). While some studies, including Sheth et al. (2008), found a decrease in bar fraction with redshift particularly for low-mass blue spirals, this effect may be

due to a decrease in resolution and obscuration by star formation and dust (Marinova & Jogee 2007). Thus, even if the bar fraction is not constant, it may only exhibit a moderate decline of a factor of 2. Our stacked ensemble is an average for low redshift galaxies and should not be considered an average extending to high ($z > 1$) redshift.

2.3 Determining the Angular Momentum Flow Timescale from Photometric Data

The first step of our experiment is to determine the instantaneous rate of angular momentum flow for any given spiral galaxy disk at each radial position. Ideally we would have the full 3D potential due stars, gas and dark matter, $\tilde{\Phi}_{tot}(r, \varphi, \theta)$ and the density distribution of the stars $\rho(r, \varphi, \theta)$. However, in practice we can at best have information on the projected stellar mass density and we employ an effectively softened potential that can be based on an observational estimate of the stellar mass surface density, $\Sigma_\star(r, \varphi)$. In §2.4 we will use simulations to test how well this works, by looking at the effects of dark matter and gas and the difference between employing the 3D and 2D potential.

There are two important steps in calculating angular momentum transfer from photometric data. The first step involves determining a map of the stellar mass distribution from surface photometry. We have looked at this problem closely (Zibetti et al. 2009; hereafter Z09), and we will summarize how this is done in §5.2; for now we will assume that we have the stellar mass distribution known.

The second step requires calculating the torques on the outer mass distribution ($r > R$) due to the inner mass distribution ($r < R$) in order to determine an angular momentum flow rate across radius R (see G95). We determine the z-component of the torque at each position R by summing the gravitational forces on the outer region due to the inner region and taking the cross product with the position vector:

$$\Gamma(R) = \tag{2.1}$$

$$G \int_{r_1>R} d^2\mathbf{r_1} \Sigma(r_1) \int_{r_2<R} d^2\mathbf{r_2} \times \Sigma(r_2) \frac{(\mathbf{r_1} \times \mathbf{r_2})_z}{[|\mathbf{r_1} - \mathbf{r_2}|^2 + \epsilon^2]^{\frac{3}{2}}},$$

where $\mathbf{r}$ is the projection vector on the equatorial plane and $\Sigma(r)$ is the stellar mass per unit area. We use a factor ϵ to account for disk thickness. G95 examined in detail how varying the treatment of disk thickness will affect the torque calculation and found it to be of little import. Thus, we adopt $\epsilon = \frac{0.7\ r_{exp}}{12}$ and examine the accuracy of this choice by testing it with the simulations (see §2.4).

The rate of angular momentum flow can be derived by comparing the torque across radius

R, $\Gamma(R)$, to the total angular momentum interior to R, $J(R)$, which is expressed as:

$$J(R) = \int_0^{2\pi} d\theta \int_0^R rdrrV_c\Sigma(r,\theta), \tag{2.2}$$

where V_c is the rotational velocity. Using the Tully-Fisher relation and an $arctan$ rotation curve parameterization (Courteau 1997) we are able to construct approximate rotation curves for each galaxy from photometry alone. The sign of rotation is determined by assuming the galaxies have trailing spiral arms (*e.g.* de Vaucouleurs 1958; Pasha & Smirnov 1982 and Pasha 1985). We define a torque-driven rate of angular momentum flow,

$$\nu_{inflow}(R) = \frac{\Gamma(R,t)}{J(R,t)}, \tag{2.3}$$

which has dimensions of time^{-1}. We can assess if torques are strong enough to be significant if the product of ν_{inflow} and a Hubble Time is greater than unity. We can re-interpret ν_{inflow} qualitatively as the rate of mass flow in the opposite direction. We determine ν_{inflow} at each position in the disk and then scale by disk scalelength. The scaled values of ν_{inflow} are then used to create a sample average profile by stacking the plots. This allows us to determine the mean rate of matter inflow for present day spiral galaxies.

However, the total angular momentum flux need not depend on the gravitational torques alone. In the case of a long-lived spiral structure, density wave theory predicts that angular momentum will also be advected (also known as 'lorry' transport). Advective transport is due to the bulk motion of the fluid and does not lead to matter flow. Depending on the pitch angle of the spiral and its longevity, advective transport may overwhelm the gravity torque by transporting angular momentum inward (G95 and BT08). However, almost all simulations show that spiral features are not long-lived but are recurrent transient features (Sellwood 2010; Sellwood & Binney 2002; Governato 2007 et al., etc.). There is also a substantial amount of observational evidence that support transient spirals (Sellwood 2000; Merrifield et al. 2006, etc.). If this is the case, the role of advective transport would be small as its effects are greatest in the case of a long-lived spiral structure with a constant pattern speed. There is no way to directly observe the strength of advective transport and so, our estimation here cannot account for it.

Also our measure of angular momentum flow need not translate straightforwardly into matter flow. Our torque measure represents the net change of the angular momentum distribution at each radial position. Changes in the angular momentum distribution may cause changes in the mass density profile of the disk, provided the stellar orbits are not too eccentric. Loss of angular momentum inside corotation causes the home radii of the stars to get smaller. If the orbits of the stars are very eccentric, the stars spend a disproportional amount of time away from the home radius and thus the mass profile changes are weakened (Sellwood & Binney 2002). The extent to which our measure of angular momentum flow can be translated into changes in the mass density profile is beyond the scope of this paper, but is certainly essential to under-

standing secular evolution. For our discussion, we caution the reader that we do not treat these complexities.

2.4 Testing Torque Estimates using Disk Galaxy Simulations

There are several challenges involved in using observations to derive an accurate torque map of a galaxy, where simulations can be used to test and refine the method. For instance, the gravitational potential of an observed galaxy cannot be strictly derived from observables (especially without detailed kinematics) and so one must make assumptions about the matter distribution. Here, we first use simulations to test how the accuracy of torque maps from projected stellar distributions is affected by the vertical extent of the stellar distributions. Second, we explore the role of gas and dark matter in exerting torques on stars. Making mass maps of the gas and dark matter component of the galaxies is difficult or impossible, respectively. Simulations with live halos and gas will allow us to determine the significance of their torques on the stars and potentially derive a correction factor for their effects.

In the following sections we show that a map of the projected stellar mass enables a sensible way to estimate the total torque on the stars; if one wants a correction for dark matter torques, we offer one.

2.4.1 Simulations

We use two simulated isolated model galaxies each with over 1.4 million particles ($N_{halo} = 6 \times 10^5$, $N_{disk} = 4 \times 10^5$, $N_{gas} = 4 \times 10^5$) from the work of Foyle et al. (2008) in order to conduct our tests. The simulations rely on the GADGET-2 code (Springel 2005) with star formation and feedback as described in Springel & Hernquist (2003). Table 2.1 lists the properties of the selected galaxies including the halo spin parameter, λ, halo concentration, c, mass or virial velocity, V_{200}, disk mass fraction, m_d, disk scale length, r_{exp}, the peak velocity of the rotation curve V_{peak} and the position of the velocity peak in terms of disk scale length (R_{peak}/r_{exp}). Fig. 2.1 shows the rotation curve for the two model galaxies. The dashed line marks the position of corotation of the spiral pattern. Corotation was calculated by measuring the angular speed of the spiral pattern and comparing with the rotation speed at that position. Fig. 2.2 shows images of the stellar mass density of the models. The models began with straight exponential profiles and were run for 10 Gyr. We chose snapshots after roughly 2 Gyr where the bars and spiral arms had formed, as these features are most relevant for the gravitational torques. We do not attempt to simulate realistic disk galaxies here. We require only 'plausible' models in order to test the method used on our observed galaxy sample. Further details of the simulations and star formation model are described in Foyle et al. (2008).

In the simulations, we calculated the torques due to the full potential throughout the galaxy and consider the potential due to the stars, gas and halo. This is somewhat different from the observationally robust approach described in §2.3, where we consider the torques on the

Table 2.1: Model Properties

	Model A	Model B
λ	0.08	0.08
c	15	10
V_{200} [km s^{-1}]	160	80
m_d	0.1	0.1
r_{exp} [kpc]	4.68	2.88
V_{peak} [km s^{-1}]	272	118
R_{peak}/r_{exp}	2.67	2.95

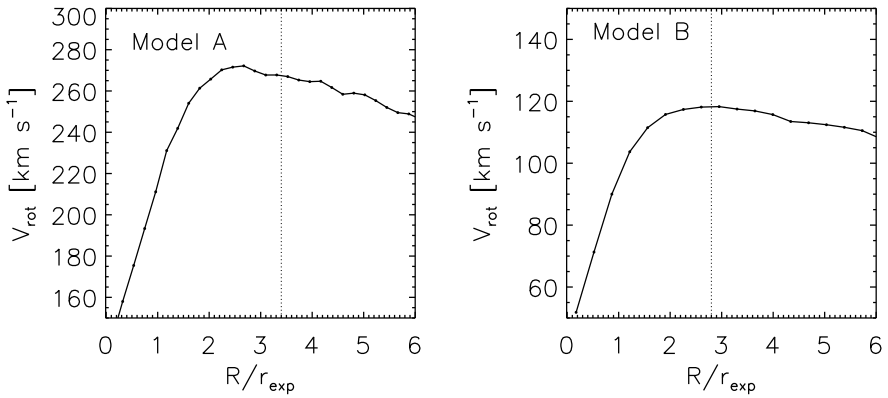

Figure 2.1: Rotation curve for models A and B after 2 Gyr of evolution. The dashed line shows the position of corotation of the spiral pattern in the model.

outer parts due to the stellar distribution in the inner parts. We also calculate the total angular momentum in an annulus as opposed to the total angular momentum within R. In order to distinguish these calculations in the simulations from those described in §2.3, we label them as Γ_z and J_z, as opposed to Γ and J (see Eq. 2.4). In order to estimate the strength of the simulation torques we divide $\Gamma_z(R)$ at each radial position by the total angular momentum in an annuli centered at R. We multiply by Δt, which is set to a time span of 1 Gyr. 1 Gyr is longer than a dynamical time, but much less than a Hubble Time, allowing us to ascertain the present strength of the torques in the simulation.

2.4.2 Projected Mass Densities and the 2D Potential

Previous works (Buta et al. 2004) have attempted to derive the 3D potential of the stellar disk directly by using Fourier techniques and assumptions about the vertical height distribution. Fol-

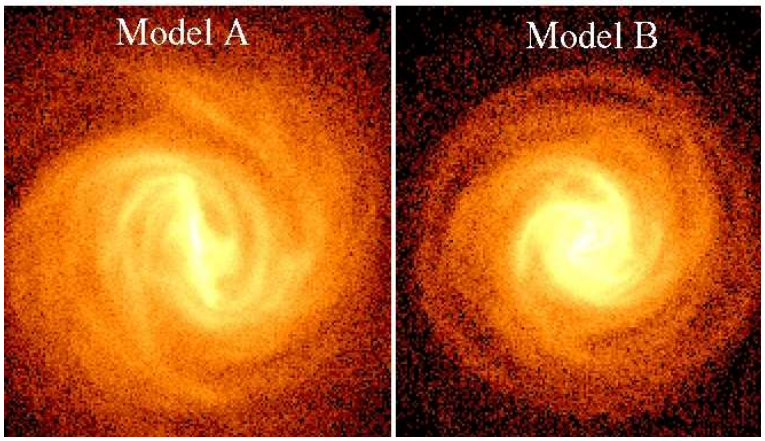

Figure 2.2: Snapshots of the stellar component of models A (left) and B (right), illustrating the stellar surface mass density 2 Gyr after the symmetric simulation start, when they showed a strong bar/spiral arm structure. Rotation is clockwise in both models, with spiral features trailing.

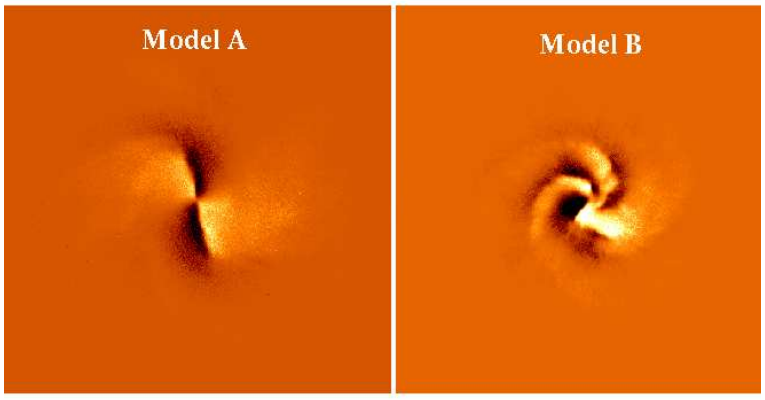

Figure 2.3: Snapshots of torques on stars by stars of models A (left) and B (right) after 2 Gyr of evolution when they showed a strong bar/spiral arm structure. Model A shows considerable symmetry in comparison to model B.

lowing G95, we choose to use a softened 2D potential and then calculated the torques directly by determining the pixel scale and adding a correction term based on the disk scale length of the galaxy ($\epsilon = \frac{0.7 r_{exp}}{12}$). G95 used a similar softening approach, but derived the potential using Fourier techniques.

Specifically, our torques are calculated as:

$$\Gamma_{z,pixel} = x_{pixel} F_{y,pixel} - y_{pixel} F_{x,pixel}, \tag{2.4}$$

where

$$F_{x,pixel} = m_{pixel} \sum_{j=0}^{n_p} \frac{G m_j (x_{pixel} - x_j)}{((x_{pixel} - x_j)^2 + (y_{pixel} - y_j)^2 + \epsilon^2)^{3/2}}$$

and

$$F_{y,pixel} = m_{pixel} \sum_{j=0}^{n_p} \frac{G m_j (y_{pixel} - y_j)}{((x_{pixel} - x_j)^2 + (y_{pixel} - y_j)^2 + \epsilon^2)^{3/2}},$$

where the sum index j runs through all pixels in the 2D image. Fig. 2.3 shows the $\Gamma_{z,pixel}$ for the torques due to the stellar distribution on the stars. Model A shows considerable symmetry in comparison to model B. When calculating the torques on stars by stars, the result is strongly affected by the symmetry of the distribution. When one azimuthally averages, considerable cancellation will occur in symmetric distributions. In Fig. 2.4, we plot the azimuthally averaged value of $\Gamma_z(R)/J_z(R) \times \Delta t$ for annuli of $0.05 r_{exp}$. J_z is the total angular momentum within the annuli. We see that, in the inner parts, the torques are strong and act on timescales significantly less than a Hubble Time (recall $\Delta t = 1$ Gyr). We see that for both model A and B, the softened 2D force (red dashed line) is indeed an accurate estimate of the full in-plane component of the 3D force (black solid line), with the average deviation between the two of only 4%. Therefore, knowing only the projected stellar mass distribution is not a serious limitation.

2.4.3 Torques on Stars from Stars versus Torques from the Gas & Dark Matter

Observations of stellar mass maps, as can be made available for large samples, will only allow us to measure the torques due to the stellar mass distribution. We use the simulations to test how significant we should expect the torques to be due to the gas and dark matter. In Fig. 2.12, the torques, $\Gamma_z(R)$, are divided by the total angular momentum in each annulus, $J_z(R)$, and multiplied by Δt, which is set to 1 Gyr, giving a dimensionless estimate of the strength of the torques. In Fig. 2.12 we consider the torques on the stars due to the stars (blue), gas (red) and dark matter (cyan). We see that the torques on the stars due to the gas are quite small and can be neglected in comparison to the other two. The dark matter torques are significant, but almost always act in the same direction as the stellar torques. Thus, a measure of the stellar torques gives us at least a minimum measure of the total torque.

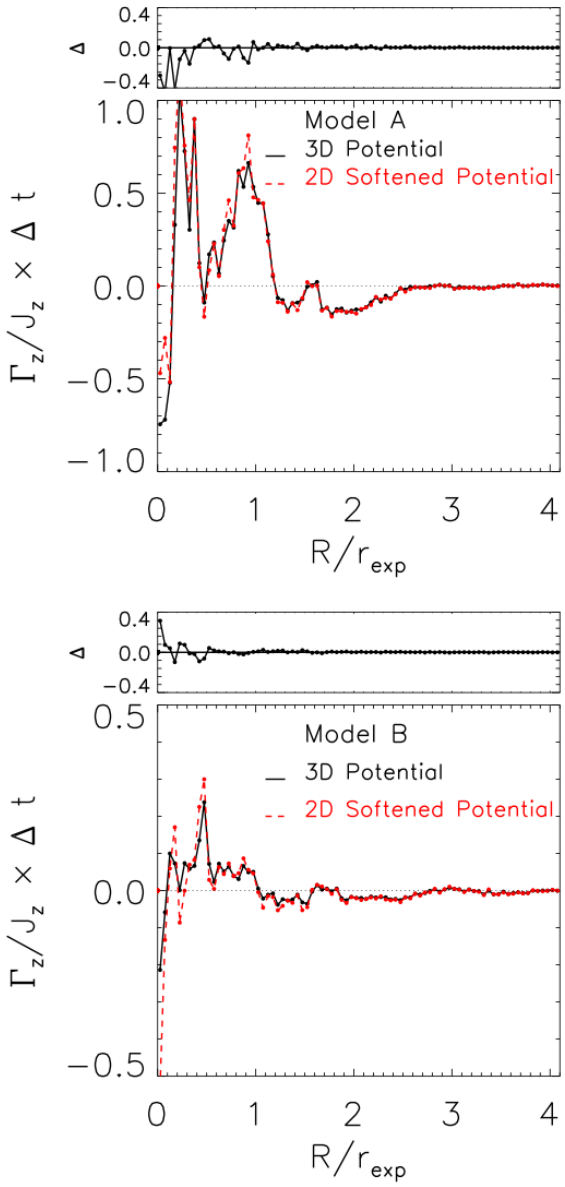

Figure 2.4: Accuracy of torques from projected mass densities in comparison to the 3D potential: the azimuthally averaged scaled torques due to the stellar particles where the distances are calculated from all three components (black line) and where the distances are calculated using only the x and y components and a correction factor for the z-component (red line) after 2 Gyr of evolution. The torques, $\Gamma_z(R)$, are divided by the total angular momentum in each annulus and multiplied by Δt, which is set to 1 Gyr, giving a dimensionless estimate of the strength of the torques. Using a softened 2D potential to calculate the torques yields an accurate estimate of those calculated using the full 3D potential. The upper panel shows the difference between the 2D softened potential and the 3D potential versus radius. Only a few peaks are stronger with the 2D potential and the average deviation between the two is 4%.

Fig. 2.6 shows the cumulative distribution of the ratio of the torques due to the stars versus the total torques of the stars and dark matter. The particles in the inner disk scale lengths have torques which are predominately due to the stellar distribution. Thus, if the torques are significant, we can conclude that the stellar torques dominate the total torques and, if anything, the dark matter torques enhance the stellar torques.

We can also use the simulations to derive a correction factor for the dark matter torques. We determine a linear enhancement function, by connecting the two median points in the inner ($r < 2r_{exp}$) region and outer ($2r_{exp} < 2 < 5r_{exp}$) region of the disk. Fig. 2.7 shows the fit for model A, which was selected as it had the strongest torques of the two models.

If we calculate the torque as we will for the observed galaxies, that is the torque on the outer stellar distribution ($r > R$) due to the inner stellar distribution ($r < R$) as described in §2.3, we see that for both models the peak of the torque curve lies interior to $1.5r_{exp}$, implying that the highest rates of inflow will be in the inner regions of the disk (see upper panel of Fig. 2.8). For both galaxies the inner regions show predominately angular momentum outflow. We also note that the peak value for the torque of model A is much greater than model B. This is mostly due to the fact that model A is a more massive galaxy with a V_{200} of 160 km s^{-1} as opposed to 80 km s^{-1} for model B and that the torque scales by the square of the mass. The quantity we need to consider when evaluating the strengths of the gravitational torques is the timescale for angular momentum flow. The timescale is given by ν_{inflow} which is the ratio of the torque, $\Gamma(R)$, to the angular momentum, $J(R)$, as calculated in Eq. 2.2. While the amplitude of the torque curves varies considerably between the models, a comparison of the timescales shows that these are roughly similar (see lower panel of Fig. 2.8).

The simulations have allowed us to show that the projected stellar mass can be used to accurately calculate the torques and the torques due to the stellar distribution on the stars, represent at least a minimum measure of the total torques due to the stellar, gas and dark matter distributions. We have been able to derive an enhancement function, which can be applied to the observed stellar torques to account for the torques due to the dark matter. Again, we wish to stress that when we compare the torques on the stars due to the stellar, gaseous and dark matter distributions, we have been calculating the torques due to the full potential of these distributions. This differs to what we do observationally (see §2.3). However, if the torques due to the dark matter are less than that of the stars when considering the full potential, it follows that they will also be less when considering the torque flow through a given radius.

2.5 The Role of Torques from Stars: a Pilot Study

2.5.1 Sample

The simulations allowed us to test our approach, but our goal is to investigate the strength of gravitational torques in an observed sample of galaxies and use a sample average in lieu of the time integral required to determine a timescale for secular evolution. As a pilot project, we

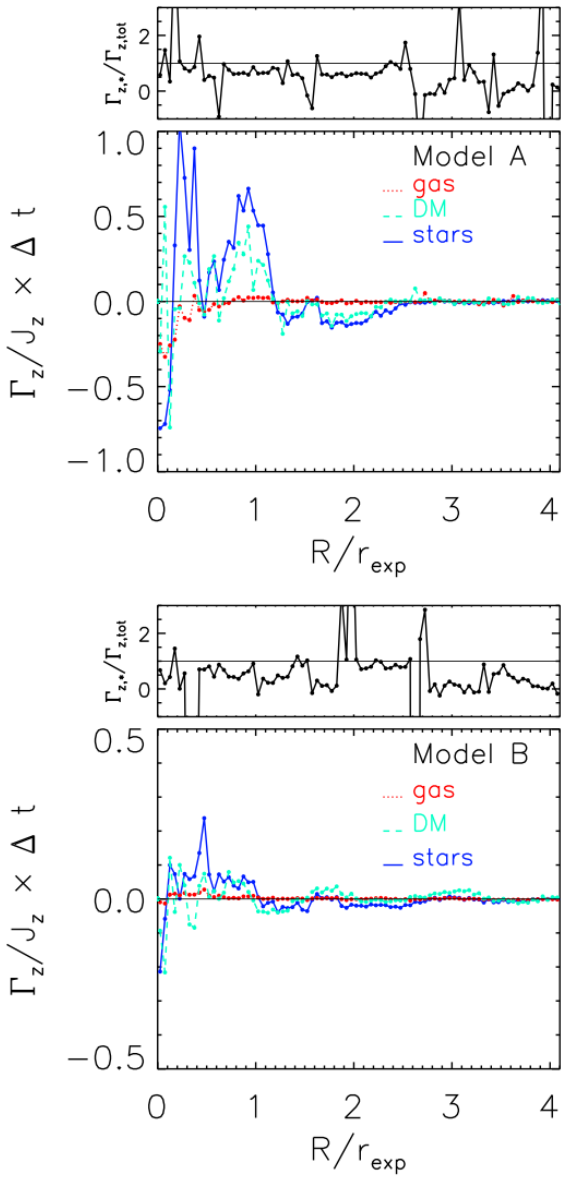

Figure 2.5: The relative importance of torques exerted by stars, gas and dark matter: a comparison of the scaled azimuthally averaged torque on the star particles due to the star (blue), gas (red) and dark matter (cyan) particles for models A and B. Model A shows considerably stronger torques than model B. In both cases the dark matter torques are weaker than that of the torques due to stellar distribution. Furthermore, the torques are such that they almost always act in the same direction. The torques due to the dark matter distribution serve to enhance the torques due to the stellar distribution. The upper panel shows the ratio of the stellar torques to the total torques. In only a few cases do the directions differ and over much of the disk the stellar torques make up the majority of the total torques.

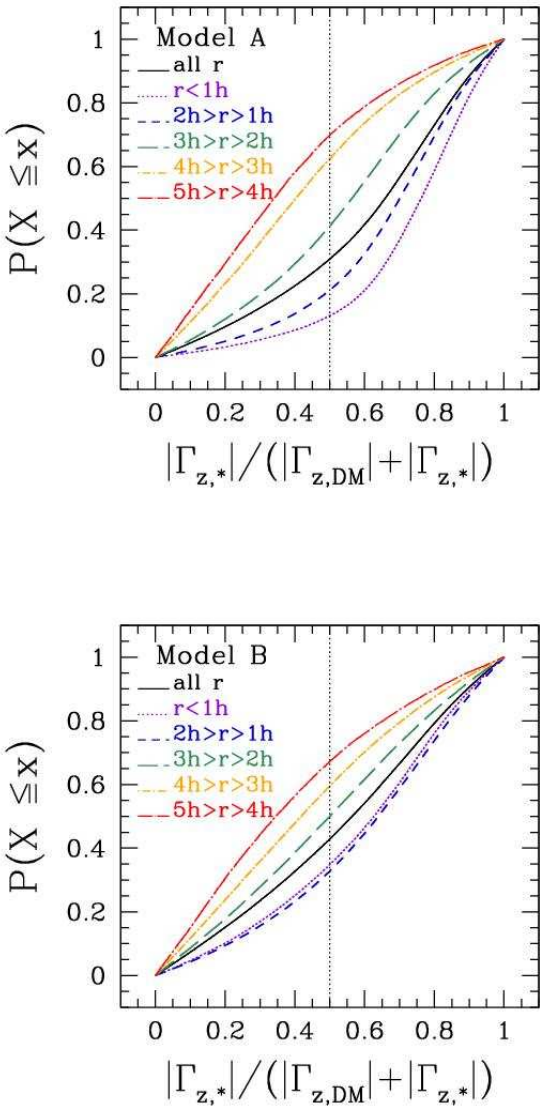

Figure 2.6: The cumulative distribution of the ratio of the total torques on stars due to the stars compared to the total torques arising from dark matter and stars for model A and B after 2 Gyr of evolution. $P(X \leq x)$ represents the percentage of particles with less than and including the respective value represented on the x-axis. The solid line represents the distribution over all radii and the colors correspond to the radial annuli listed. This figure illustrates that within $3r_{exp}$ the torques due to the stellar distribution dominate those of the dark matter distribution.

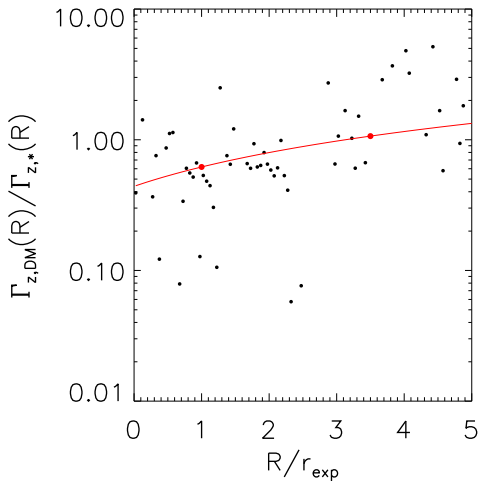

Figure 2.7: We fit an enhancement function by choosing the median of the ratio of dark matter torques to the stellar torques in the inner regions ($r < 2r_{exp}$) and the outer regions ($2r_{exp} < r < 5r_{exp}$). Between the median points in the inner and outer regions, we plot a straight line in linear scale.

selected 24 nearby galaxies from the 7th data release of SDSS (York et al. 2000) . We wanted the galaxies to be all roughly of the same mass (have the same rotational velocity) in order to use them to create a sample average. In order to reduce errors incurred by deprojection, we also wanted them to be roughly face-on, $\cos i > 0.6$. We required $m_H < 10$ mag with the H-band magnitudes taken from the 2MASS Large Galaxy Atlas (Jarrett et al. 2003). Using the distance from NED and the Tully-Fisher relation (Tully et al. 2008), we required that the rotation velocity lie between 180 and 250 km s^{-1}. The galaxies also required SDSS g and i band data in order to calculate the mass-to-light ratio and to make the mass maps. Galaxies where bright stars were superimposed on the image were rejected as residuals from such features would affect the mass and torque maps.

We return to the observationally robust method of calculating the torques, $\Gamma(R)$, which we described in §2.3 (in following G95) as opposed to those employed in the simulations, Γ_z. Table 2.2 lists the galaxy properties in this pilot study. In the following sections we outline how the mass maps and radial torque profiles were generated.

2.5.2 Stellar Mass Maps

An accurate map of the stellar mass distribution of the galaxies is essential to properly determine the torques. In particular, the contrast of non-axisymmetric features such as bars and spiral arms, must be known. Spiral arms will contribute disproportionally to the light at any wavelength, unless the effect is corrected.

We determine the mass distribution of the galaxies pixel-by-pixel, by combining g and i-band images from SDSS, as laid out in Z09. We summarize briefly the steps here and show the

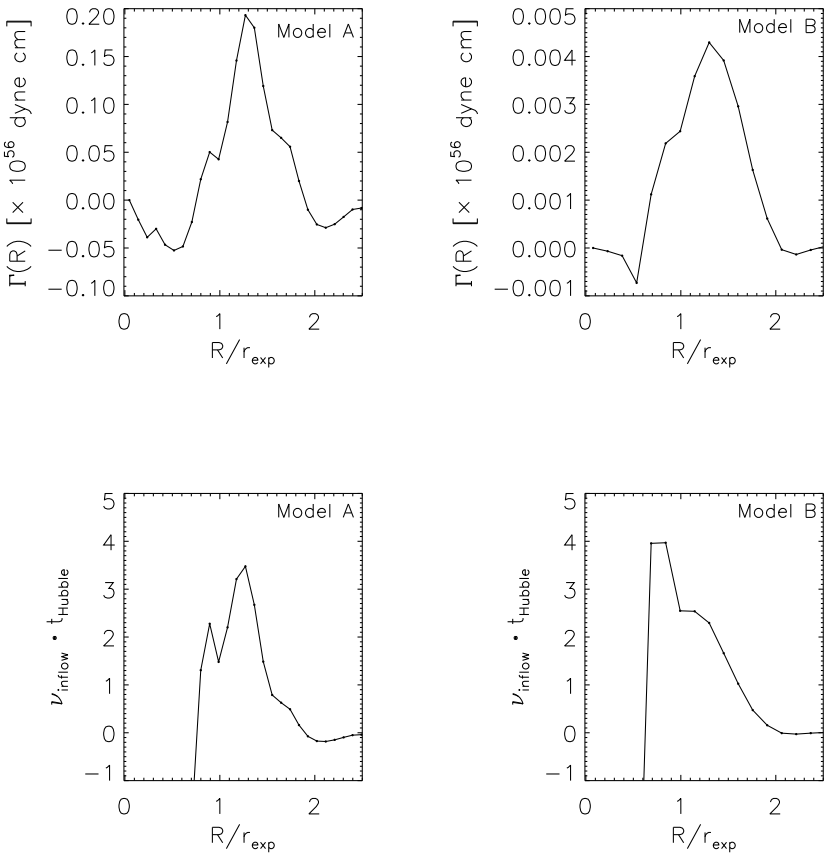

Figure 2.8: (Upper Panels) Torque across radius R, *i.e.* the torque on the outer stellar distribution ($r > R$) due to the inner stellar distribution ($r < R$) for models A (left) and B (right), as described in §2.3 in following G95. This quantity is more suited for application to real data; it describes the total instantaneous radial flow of angular momentum through R. For both models, the torque curve peaks between $1r_{exp}$ and $2r_{exp}$. (Lower Panels) Instantaneous torque across radius R, assumed to reflect the instantaneous angular momentum flow, put in the secular context by presuming $\nu_{inflow} \cdot t_{Hubble}$ for models A (left) and B (right) where $\nu_{inflow} = \frac{\Gamma(R)}{J(R)}$. We see that in the inner regions, $r < 2r_{exp}$, the torques imply a timescale short compared to t_{Hubble} so that there is significant matter inflow within a Hubble time. In the upper panel the amplitude of the torque curve of model A is much greater than that of model B. Now, having scaled by the angular momentum, we see that the overall strength of the torques is comparable.

Table 2.2: Sample Galaxies: Morphological classifications and distances are taken from NED. V_{rot} is determined via the Tully-Fisher relation and the sign distinguishes the galaxies, which rotate clockwise (negative) and counter-clockwise (positive), assuming they are trailing spirals. The PA, $\cos i$ and r_{exp} were fit using GALFIT (Peng et al. 2002). The peak value of the torque profiles $(\Gamma \cdot A)_{peak}$, where $A = \frac{Gt_{Hubble}}{r_{exp}^2 V_{rot}^3}$ making the torques scale invariant (see §2.6) are listed for reference.

Name	Type	Distance [Mpc]	PA [deg]	$\cos i$	r_{exp} [kpc]	V_{rot} [km s^{-1}]	$(\Gamma \cdot A)_{peak}$
M61	SAB(rs)bc	17.0	76.0	0.94	3.0	-222	0.4
M96	SAB(rs)ab	10.9	-15.	0.68	3.0	-234	1.9
M100	SAB(s)bc	17.0	42.0	0.84	5.3	242	0.3
M101	SAB(rs)cd	4.94	58.0	0.83	2.5	201	0.03
NGC 2775	SA(r)ab	16.7	-12.0	0.77	4.7	-210	0.05
NGC 3166	SAB(rs)0/a	16.6	85.0	0.64	4.0	-259	0.7
NGC 3169	SA(s)a	15.1	59.0	0.71	4.2	-242	6.4
NGC 3351	SB(r)b	9.3	10.3	0.75	2.6	185	0.7
NGC 3583	SB(s)b	29.9	-57.0	0.71	3.0	248	0.5
NGC 3631	SA(s)c	16.7	-66.3	0.83	3.3	-218	0.03
NGC 3642	SA(r)bc	22.9	-48.0	0.83	4.2	198	0.01
NGC 3718	SB(s)a	14.5	0.9	0.61	7.4	-218	0.06
NGC 3938	SA(s)c	11.6	34.0	0.93	2.0	-183	0.02
NGC 4145	SAB(rs)d	14.3	-78.7	0.59	3.0	179	0.04
NGC 4151	SAB(rs)ab	14.0	-20.0	0.94	3.6	-229	0.02
NGC 4314	SB(rs)a	13.2	-62.5	0.84	2.7	219	0.9
NGC 4450	SA(s)ab	17.0	-7.62	0.67	4.3	-219	0.03
NGC 4579	SAB(rs)b	17.0	-86.0	0.8	4.2	246	0.7
NGC 5317	SA(rs)bc	16.7	28.0	0.65	5.2	-231	0.02
NGC 5383	SB(rs)b	32.3	-80.6	0.65	5.7	-252	0.15
NGC 5713	SAB(rs)bc	25.9	21.0	0.91	2.8	238	0.4
NGC 5921	SB(r)bc	20.7	-35.0	0.85	4.0	232	0.08
UGC 5001	SB(r)0+	22.7	-84.0	0.85	7.2	246	0.04
VCC 1253	SB(s)0	17.0	56.6	0.89	2.67	204	0.3

importance of accurately determining the mass maps for the purposes of gravitational torque measures.

The $g-i$ colour image is used to infer stellar i-band mass-to-light ratios at each pixel, which are then multiplied by the i-band surface brightness, resulting in the stellar mass density. Look-up tables as a function of $g-i$ colour are used to determine the i-band mass-to-light ratio. These tables marginalize over a Monte Carlo library of 50 000 stellar population models by Bruzual & Charlot (2003, version 2007). A median adaptive smoothing technique is used to extract reliable flux and colour information at any position in the galaxy, while preserving the highest possible spatial resolution. Z09 have found that the set of pass-bands (g, i and H) works well to obtain mass maps with M/L uncertainties < 0.1 dex per pixel. Unfortunately, due to sky brightness and long integration times in the H-band, it is not possible to obtain images for a large sample of galaxies that extend beyond 2 r_{exp} using g, i and H. Z09 have shown that combining g and i alone is an adequate alternative, differing by typically < 0.03 dex from mass maps made with all three pass bands.

In practice, the maps for the 24 sample galaxies are made, as follows:

i) g and i band images of the galaxies are made from the 7th data release of SDSS (Abazajian et al. 2009; York et al. 2000) by combining the scans as our galaxies are all quite large;

ii) the sky-background was subtracted by determining the median background;

iii) median adaptive smoothing with a maximum smoothing radius of 10 pixels was conducted on both images individually and $S/N > 20$ was required at each pixel (ADAPT-SMOOTH: Zibetti 2009);

iv) adaptive smoothing was run again to match the smoothing in the g and i band;

v) $g-i$ was used to define colours for each image and a stellar mass-to-light ratio was determined via a look-up table at each pixel;

vi) the mass-to-light ratio image and the i-band image were combined into a stellar mass map.

Further details of this procedure can be found in Z09.

It had been argued previously, that 'red' images (Elmegreen & Elmegreen 1985) or near-IR images (Rix & Zaritsky 1995) by themselves might be close enough approximations to the surface mass density. Following examples from Z09, we show this is not the case, at least for the i-band, in the context of stellar torques. To illustrate this, we compare the mass maps outlined here with those generated by multiplying an i-band image with a global M/L. This global M/L was determined from the total $g-i$ colour using the constants of Bell et al. (2003). Fig. 2.9 shows the mass and torque maps generated with these two approaches. A comparison of the

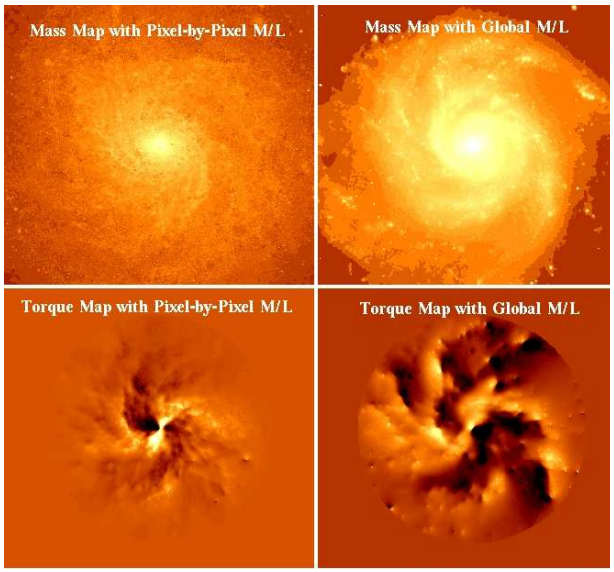

Figure 2.9: Mass maps (upper panels) made from the pixel-by-pixel method of Z09 using g and i-band image from SDSS (left) and that using a one global mass-to-light ratio à la Bell et al. (2003) using an i-band image for M101 (right). The torque maps for each respective mass image are shown in panels 3 and 4 (from the left). The global mass-to-light ratio using the Bell et al. (2003) methodology enhances the spiral arms and the torques associated with them. We have chosen to use the pixel-by-pixel method as it avoids over-enhancing the spiral arms, which leads to torque overestimates.

mass maps shows that the spiral arms appear more prominent in the $(M/L)_{global}$ mass map (the scaled i-band image) as opposed to the g and i band pixel-by-pixel mass map. The effect of this is clearly seen in the torque map, where strong torques are seen along the spiral arms in the i-band mass map. It is clear from the torque maps, that accurate mass maps are central in order to correctly estimate the strengths of the torques.

As pointed out by Z09, there also is a strong difference in the inferred mass density profiles between the two approaches. The scaled i-band image (solid) in Fig. 2.10 tends to underestimate the mass in the interior and overestimate the mass in the outer parts. The pixel-by-pixel method ensures we have correctly estimated the mass and most importantly, mitigates the problems associated with over-weighting regions like the spiral arms due to young, luminous populations (Z09). Fig. 2.11 shows the final mass maps for the sample of 24 galaxies.

2.5.3 Making Radial Torque and Angular Momentum Profiles

After we created the mass maps using the g and i-band images from SDSS, we removed stars by interpolation and deprojected the galaxy in order to calculate the torques as follows:

i) We removed foreground stars using the IMEDIT task in IRAF, which replaced the stars by the average mass density in the surrounding background region;

ii) The center of the galaxy was found using CENTER and represents the peak of pixel

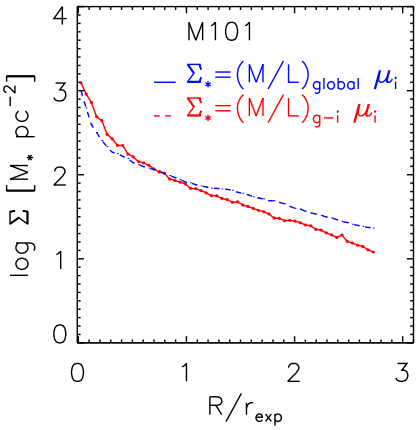

Figure 2.10: Comparison of the mass density profiles using the mass maps made by a pixel-by-pixel method with g and i-band images (blue dashed line) and that using a global mass-to-light ratio and the Bell et al. (2003) recipe with an i-band image (red solid line). In the inner regions the Bell et al. (2003) recipe underestimates the mass, while in the outer regions it overestimates the mass.

intensities in the central region;

iii) We used GALFIT (Peng et al. 2002) on the i-band images to fit a simple exponential disk profile to the outer parts of the galaxies, in order to determine the galaxies' orientation, which included the inclination, $\cos i$, position angle, PA, and disk scale length r_{exp}. Since the bar/bulge region can often lead to wrong fits of these values, the inner regions were masked. The size of the masks were gradually increased until the orientation parameters converged.

iv) The center values and the PA and i from GALFIT were used to deproject and rotate the mass maps for all galaxies.

The deprojected mass maps were then used to create a torque profile of the galaxy. For each pixel we calculated the force on that pixel due to all other pixels beyond radius R with an outer limit, which was set to be a maximum limit where all pixels in the annulus had sufficient signal-to-noise.

This force included the softening correction $\epsilon = 0.7 r_{exp}/12$ in order to account for disk thickness (see §2.4.2 for further details). The x and y gravitational acceleration components of the pixels beyond radius R, due to the mass distribution of the pixels within radius R, were used to determine the total z-component of the torque beyond radius R. We express this as:

$$\Gamma(R) = \sum_{r>R} m_{pixel}(x_{pixel} f_y - y_{pixel} f_x), \tag{2.5}$$

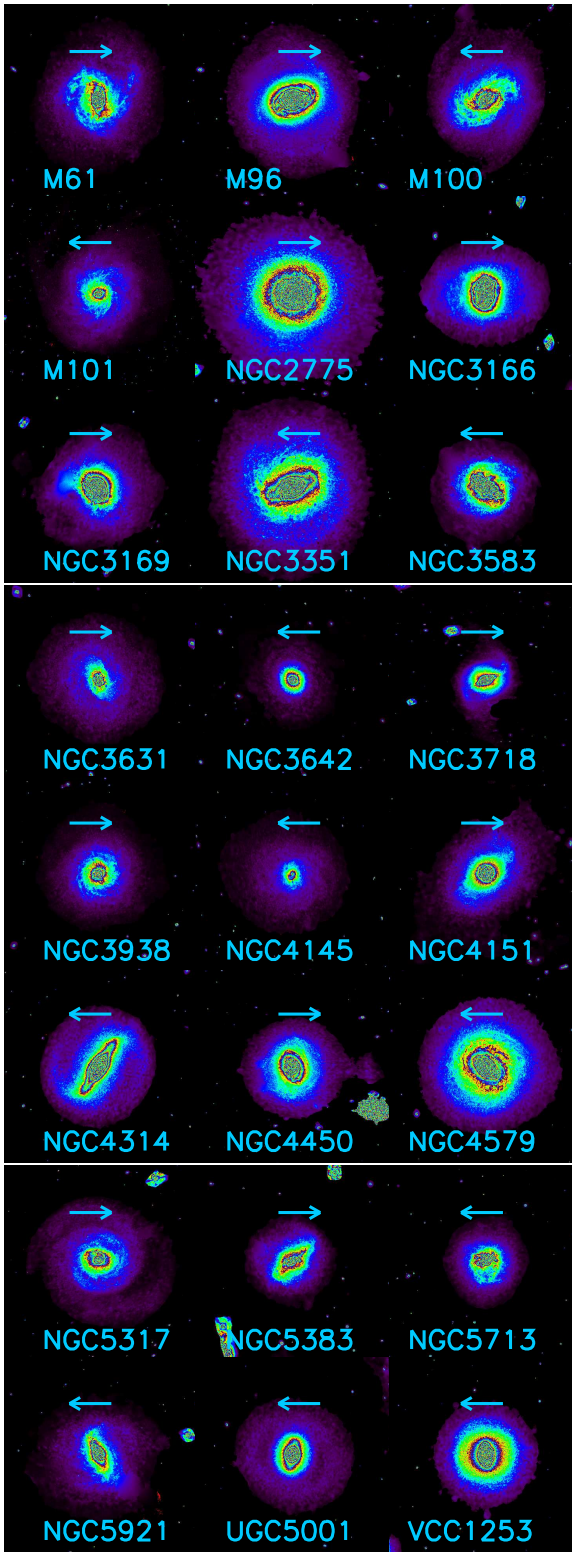

Figure 2.11: Mass maps after deprojection for the sample of 24 galaxies. The arrows denote the direction of rotation chosen based on the assumption of a trailing spiral.

where $\sum_{r>R}$ is the sum over all pixels beyond radius R, m_{pixel} is the pixel mass of the pixels beyond radius R, x and y are the pixel positions and f_x and f_y are the x and y-components of the gravitational acceleration due to the mass distribution of the pixels within radius R respectively. We calculated the torque, $\Gamma(R)$, in radius increments of 5 pixels. The galaxies have a deprojected pixel size between 60 and 120 pc.

In order to determine the angular momentum, we require the rotational velocity at each pixel. While many of the galaxies in the sample do have kinematic measurements, we wish to outline the method we will use for a much larger sample when we will not have such information. Thus, we construct an approximation from the image only. The rotational velocity for each pixel was found by generating a rotation curve,

$$V_{rot}(R) = \frac{2}{\pi} V_{max} \arctan(\frac{R}{0.1 r_{exp}}) \tag{2.6}$$

(Courteau 1997), where V_{max} was found from the Tully-Fisher relation (Tully et al. 2008) and the galaxy's absolute magnitude. The transition radius of $0.1\ r_{exp}$ was chosen based on the mean value of 300 Sb-Sc spirals from the Courteau (1997) sample. Given that the vast majority of spiral galaxies exhibit a trailing spiral pattern (de Vaucouleurs 1958; Pasha & Smirnov 1982 and Pasha 1985), we assume that all galaxies in our sample rotate in this way. The sign of V_{rot} was decided by assuming a trailing spiral structure in a right-handed system, where clockwise is negative. Table 2.2 provides the rotation velocity and gives the sense of rotation. In Fig 2.11 we show the mass maps of the 24 galaxies and the arrows denote the direction of rotation. For a number of galaxies, we have compared the rotation curve models to kinematic data from Sofue et al. (1999). While the models only approximate the data, they are accurate to within 20%. This is sufficient for our purposes, since our results depend linearly on V_{rot}. Note also, we are assuming that the material in the center also exhibits circular disk rotation. While it is true that there might be considerable deviations from this in the central regions, particularly in the case of barred galaxies where the velocities will be higher, these deviations would only make the timescales faster. Thus, our schematic model rotation curves provide at least a minimum measure of the torque timescales.

The angular momentum inside radius R, $J(R)$, was found by summing the angular momentum of each pixel where $r < R$ as:

$$J(R) = \sum_{r<R} m_{pixel} V_{rot,pixel} r_{pixel}, \tag{2.7}$$

where $\sum_{r<R}$ is the sum over all pixels interior to R, m_{pixel} is the mass of each pixel interior to R, $V_{rot,pixel}$ is the rotational velocity and r_{pixel} is the distance to the center.

Thus, at each radial position, R (in increments of 5 pixels), we have the torque, $\Gamma(R)$, on the stars beyond R exerted by the stellar distribution within R; and we have an estimate of the total angular momentum within R, $J(R)$. This defines a rate of angular momentum flow as

$\nu_{inflow} = \Gamma(R)/J(R)$ (recall that we do not include the effects of advective transport). In order to ascertain whether gravitational torques are strong enough to have a measurable effect within a Hubble Time, we scale this to the Hubble Time as $\nu_{inflow} \cdot t_{Hubble}$ where $t_{Hubble} = 13.6$ Gyr. We create radial profiles of this quantity for each galaxy in the sample.

In order to see how sensitive the torque maps were to the steps in the image analysis, we used one galaxy to test the effects of not properly selecting the center of the galaxy and errors in the position angle, inclination and disk scale length. We allowed the center position to vary by 4 pixels in both the x and y direction, which was twice the typical uncertainty in x and y from CENTER in IRAF. The position angle was given a range of $\pm$ 10 degrees, the inclination angle was given a range of $\pm$ 7 degrees, and the disk scale length was given a range of 10 % (tophat range). Using Monte Carlo samplings of these error ranges, we found that while some variation is seen in the position of the peaks of the torque profiles, the amplitude remained quite similar. We found that the torque profiles were most sensitive to the deprojection parameters (PA and i) and thus we investigated this further.

The position angle of the major axis of relatively face-on galaxies is often difficult to obtain accurately from photometry. The challenge here is that often the faint outer regions of galaxies are not detected in surveys like SDSS, leading to photometric fits of the inner oval region. While for a small sample of nearby galaxies it is possible to obtain kinematic measures of the deprojection parameters, for a larger sample this will not be possible. Thus, we examined the effect of using GALFIT deprojection parameters based on photometry as opposed to kinematic estimates. In our sample of 24 galaxies, 12 galaxies were identified with position angles measured from kinematics and in five cases the inclinations were also fit using kinematics. Table 2.3 lists the GALFIT deprojection parameters (PA_{GALFIT} and $\cos i_{GALFIT}$) and those from kinematics ($\mathrm{PA}_{literature}$ and $\cos i_{literature}$). We quantify the difference between these two sets of deprojection parameters by the angle α, which is the angle between the kinematic and photometric deprojection vectors. The median value of α is 14°. α is quite small even when there is a large discrepancy between the position angles. This is because the galaxies are all relatively face-on and even large changes of the position angle have little effect on the overall deprojection vector, or stretch.

We show how the torque profiles compare based on the different deprojection parameters in Fig. 2.12. The torque profiles where GALFIT deprojections were used are shown in black and those where kinematic measures were used are shown in red. The torque profiles are scaled by a factor $A = \frac{Gt_{Hubble}}{r_{exp}^2 V_{rot}^3}$ to make them scale invariant (see §2.6). While the profiles do change in shape, the overall amplitude remains the same and the errors are not systematic. Furthermore, the changes are small compared to the object-to-object variance. The root median squared difference between the torques of the 12 galaxies based on the two sets of deprojections is 0.03. Thus, provided the larger sample is restricted to relatively face-on galaxies, photometric deprojection parameters can be used with confidence.

Table 2.3: Deprojection parameters of 12 galaxies with kinematic measures in the literature

Galaxy	PA_{GALFIT} [deg]	$PA_{literature}$ [deg]	$\cos i_{GALFIT}$	$\cos i_{literature}$	α [deg]	reference
M61	76.0	138.0	0.94	0.91[1]	22.8	Cayatte et al. 1990
M96	165.0	168.0	0.68	none given	2.3	Schneider 1989
M100	42.0	153.0	0.84	0.89[1]	48.8	Knapen et al. 1993
M101	58.0	39.0	0.83	0.95	17.6	Bosma et al. 1981
NGC 3631	113.7	150.0	0.83	0.96[1]	22.7	Knapen 1997
NGC 3642	132.0	122.6	0.83	0.94[1]	14.5	Verdes-Montenegro et al. 2002
NGC 3718	0.9	200.0	0.61	0.64	15.0	Sparke et al. 2009
NGC 3938	34.0	20.0	0.93	0.98	10.8	Van der Kruit & Shostak 1982
NGC 4450	172.4	175.0	0.67	0.71[1]	3.7	Cayatte et al. 1990
NGC 4151	-20.0	20.0	0.94	0.98	13.3	Bosma et al. 1977
NGC 4579	94.0	95.0	0.80	0.81[1]	1.1	Cayatte et al. 1990
NGC 5383	99.4	85.0	0.65	0.77[1]	14.3	Sancisi et al. 1979

[1] inclination measured from photometry

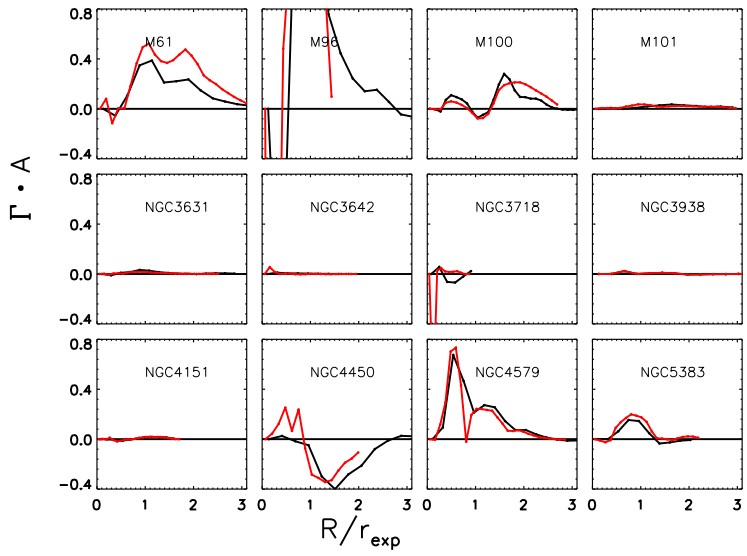

Figure 2.12: Comparison of the effect of the deprojection values measured from GALFIT (black) to the literature values (red) on the torque profiles scaled by a factor $A = \frac{Gt_{Hubble}}{r_{exp}^2 V_{rot}^3}$. While the shape of the profiles change in some cases, the overall amplitude remains much the same. The root median squared difference is 0.03.

2.5.4 M100 - Comparison with the analysis Gnedin, Goodman & Frei (1995)

We repeated the analysis of G95 on M100 in order to compare our analysis with their results. While we did not use Fourier decompositions, our approach was conceptually identical in that we determined the torque on the inner region of the stellar distribution due to the outer region of the stellar distribution at each radius R (see Eq. 2.1). G95 expressed the torques in $cm\ dynes$ and we do so here for ease of comparison. We used both the i-band image used by G95 (Frei et al. 1996) deprojected using their PA and i and their method to convert to mass using a constant mass-to-light ratio of 2.85 for the i-band as well as our mass maps made from the pixel-by-pixel method with g and i-band images from SDSS. In the first case we confirmed that the total stellar mass within $160''$ was the same as that found by G95. Despite this agreement, we found substantially different results for the torque. While our torque profile was very similar in shape (cf. their Fig. 7), the strength of the torque was found to be a factor ~ 5 less than that cited by G95. We tested our code with point masses and symmetrical distributions and confirmed that the code was indeed producing the torque amplitudes accurately. It remains unclear as to the cause of this discrepancy.

As we saw in §2.5.2, accurate mass maps are central for properly estimating the torques. Using our g and i-band images to create pixel-by-pixel mass maps, we found that the stellar mass was less than that assumed by G95 (by a factor of 2; see Z09 about the systematic difference with respect to earlier determinations, e.g. Bell et al. 2003). In Fig. 2.13 we show the torque curve as calculated using the image of Frei et al. (1996) and their mass-to-light ratio (solid line). We scaled the torque curve to enclose the same total mass as that found by the pixel-by-pixel (dot-dashed). Since the torques are proportional to the square of the mass, this implies a decrease in the torque curve by a factor of 4. Furthermore, using the pixel-by-pixel method - as opposed to a global mass-to-light ratio - even further alters the torque profile (dashed line, §2.5.2). This again illustrates how crucial it is to properly calculate the mass using a pixel-by-pixel method if one wants an accurate estimate of the torque.

2.6 Results & Discussion

In the previous section, we have derived the instantaneous torques exerted by stars on stars across different radii, $\Gamma(R)$, for the 24 galaxies in the sample. For ease of comparison we scaled the torque profiles by a factor $A = \frac{Gt_{Hubble}}{r_{exp}^2 V_{rot}^3}$, where $t_{Hubble} = 13.6$ Gyr. Galaxies are self-similar in terms of their disk scalelength and rotational velocity. This scaling factor assumes the torques are self-similar and allows the torque profiles to be dimensionless. Fig. 2.14 shows all 24 profiles. While each individual galaxy shows a unique profile, a number of similarities can be identified. The galaxies show predominately positive torques, which imply angular momentum outflow and hence matter inflow. Thus, in much of the inner parts, angular momentum is flowing outward in these galaxies. Furthermore, the peak of the torque curves almost all lie within $1.5\ r_{exp}$. This agrees with our simulations, where we also found the peak of the torque curve

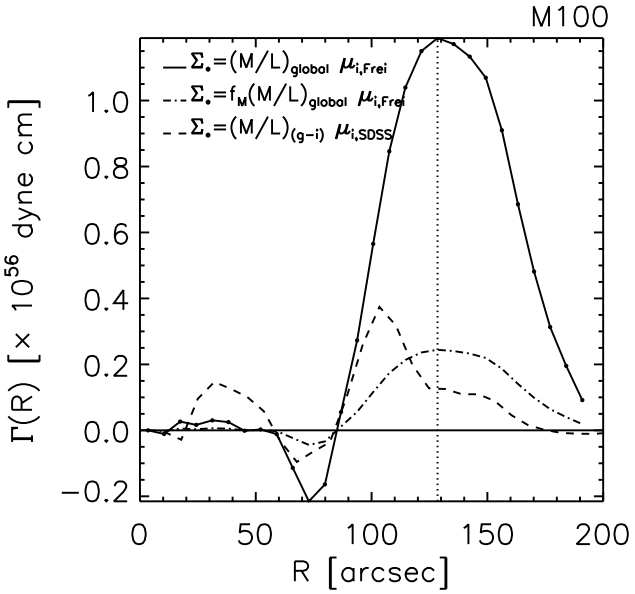

Figure 2.13: Radial profiles of the torque for M100 using the i-band image of Frei et al. (1996) and a constant mass-to-light ratio (solid), the mass map made from g and i SDSS images using a pixel-by-pixel method (long dash) and the mass map made from the i-band image of Frei et al. (1996) and a constant mass-to-light ratio scaled to include the same total mass as that of the mass map made using the pixel-by-pixel method (dot-dash). Despite repeating the same process as G95 the torques are much less than those found by them (cf. the solid line with Fig. 7 in G95). Furthermore, there are two other issues associated with the torques calculated from the Frei et al. (1996) image. Their total mass was a factor of 2 greater than that calculated by the pixel-to-pixel method, which means the torques are a factor of 4 greater. We scaled the torques of the image by $f_M = 0.25$ for comparison (dot-dash). Using the more accurate pixel-by-pixel mass map, even further alters the torque profile as it avoids over-enhancing the spiral arms. Simply using 'red' images as proxies for mass maps is insufficient in this context.

to lie within 1.5 r_{exp}. Thus, both the simulations and observations show that, instantaneously, angular momentum is flowing outward in the inner disk and the peak value lies at approximately one disk scale length. As we have seen in §2.3, how gravitational torques lead to matter flow is complex, but at least qualitatively angular momentum flow is related to matter flow.

In Fig. 2.14 we see that a third of the galaxies display strong torques in the inner regions (the peak values of these curves are listed in Table 2.2). By strong, we mean torques that have inflow timescales shorter than a Hubble Time. One may note as well that those galaxies with strong torques also show strong bars. There are two possible interpretations here; either only barred galaxies have strong torques and these galaxies have bars, which are permanent features that do not dissolve over time or we can interpret the relative abundance of galaxies with strong torques as an estimate of their duty cycle. In the case of the latter, we see that most of the time the galaxies are in a state such that the torques are not significant, however at some times the torques are very strong. In order to quantify the length of time in periods of strong and weak torques, one would need to turn to a much larger sample. Given that barred and unbarred galaxies have similar dynamical and structural parameters (Courteau et al. 2003) it seems sensible to treat them as a single group. However, since the dissolution of bars remains a topic of debate (*e.g.* Berentzen et al.1998; Bournaud & Combes 2002; Bournaud et al. 2005; Debattista et al. 2006; Curir et al. 2008) we intend to examine sub-samples of barred and non-barred galaxies with a larger sample. If it is the case that a fraction of galaxies are always barred, while others, with similar global properties, never or rarely are, it will be interesting to examine whether secular changes due to the bars, leave that sub-population indistinguishable in their gross profiles.

We note, that M100, in contradiction to what G95 found, does not exhibit strong torques such that they would be significant within a Hubble Time. As we saw in §2.5.4, when we repeated the analysis of G95, our calculations show significantly weaker torques and longer timescales than theirs. G95 found a timescale of $\sim$ 5-10 Gyr, while we find a timescale of $\sim$ 25-30 Gyr, which is significantly longer than a Hubble Time. This implies that angular momentum redistribution is not important for M100 at this point in time.

While it is interesting to look at the individual galaxy profiles, they only reflect instantaneous torque curves and one cannot assume that the torques of the past and future will be the same, since the spiral and bar features may change over time. Thus, in order to draw conclusions on the overall strength of the gravitational torques in spiral galaxies, we must turn to an ensemble average, as a proxy for the observationally infeasible time integral required to derive a mean rate of secular evolution. Given that direct observations (Jogee et al. 2005) suggest that the characteristic strength of spiral arms and bars has not changed in the last 5-8 Gyrs, or, if it has, the effect has been moderate (by a factor of 2), we can assume for an ensemble that $\langle \Gamma(R, t_{now} \rangle_{sample} \approx \langle \Gamma(R, t_{later}) \rangle_{sample}$. In this approximation, sample stacking becomes a substitute for time-averaging. In order to average the galaxies, we scaled them first by disk scale length. Alternative methods, which we explored, involved scaling by bar length or the distance

of the torque profile peak, r_{peak}. Bar length is known to be proportional to disk scale length (Pérez et al. 2005) and may thus be equivalent. However, in the case of unbarred galaxies, it is not clear how to scale them. Scaling by r_{peak} will by definition create a peak in the averaged torque plot. We aimed to have an independent means to scale the galaxies and have thus selected disk scale length.

Fig. 2.15 shows the results of averaging the torque profiles over the sample of 24 galaxies, after scaling the torques by $A = \frac{Gt_{Hubble}}{r_{exp}^2 V_{rot}^3}$. For the purposes of a time average, it is essential to use the mean instead of the median of the sample. The median provides the most common state a galaxy is in, whereas the mean provides an average over time. The qualification of the uncertainties (as indicated by the error bars) bears careful consideration. We have used the jackknife method to determine the uncertainties on the mean torque profile. The red curves show the jackknife iterations for the mean of the sample and the blue curves show the jackknife iterations for the median. The solid black line shows the mean of the entire sample. The long error bars in Fig. 2.15 show the jackknife standard deviation of the mean, $\sigma_{J,mean}$ which is calculated as

$$\sigma_{J,mean}(R) = \sqrt{\frac{N-1}{N}\sum_{i=1}^{N}(x_{J,i}(R) - \bar{x}(R))^2}, \tag{2.8}$$

where N is the number of galaxies, $x_{J,i}(R)$ is the mean torque for each jackknife iteration at the position R and $\bar{x}(R)$ is the mean torque for the entire sample. The short error bars replace σ by the 68 % confidence range multiplied by $\sqrt{N-1}$. If the distribution were gaussian, we would expect that these two sets of error bars would be the same. This implies that the statistic is affected by a small number of objects, which may reflect rare stages of galaxy evolution or more mundane data issues.

The blue curves which represent 24 median jackknife iterations show substantially lower torques than the red curves, which represent the mean. This implies that much of the time the galaxies are in a state where the torques are relatively weak, but for some periods of the time, the torques are much stronger. In order to determine how long the torques are strong, one would need a much large sample.

Fig. 2.15 shows that there is a characteristic profile for the angular momentum flow within 3 r_{exp}: the torques are positive implying that angular momentum is transported outward. Previous works (Kranz et al. 2003 and Tamburro et al. 2008) have shown that the co-rotation pattern of spiral arms lies at 2.7 r_{exp}. Taken together, this constitutes direct observational proof that for disk galaxies as a class angular momentum is indeed transported outward, as expected from theoretical studies. This observational result is independent of whether spiral arms are quasi-stationary as we have used the sample average.

If one examines closely the 24 red mean curves of the jackknife iterations one notes that two curves deviate significantly from the mean of the entire sample. This implies that two galaxies are contributing strongly to the mean torque curve. These galaxies are M96 and NGC

3169. It is possible that these galaxies represent time spans in an average galaxy's life where the torques are significantly different and thus they should be kept in the sample. However, they may also be peculiar cases. NGC 3169 had a bright foreground star superimposed, which proved challenging to subtract. There is concern that poor subtraction of this star may have caused anomalies in the final mass map. Furthermore, NGC 3169 is an interacting galaxy that has clearly been disturbed. Due to the large bar in M96, it was difficult to converge on values for the position angle and inclination during the GALFIT iterations. Given these issues, we show in the right panel the sample average calculated by removing these two galaxies. In order to determine if the torque profiles of these galaxies are truly representative of periods of strongly deviating torques, one requires a much larger sample.

Fig. 2.16 quantifies the rate of angular momentum transport. Again we show the 24 jackknife iterations (red curves) and the mean curve of all 24 (black). On the right we have removed M96 and NGC 3169 from the sample, leaving 22 galaxies. For both cases in the very inner regions ($r < 1\ r_{exp}$), the torques on the stars due to stellar distribution lead to a flow rate which is less than a Hubble Time. We remind the reader that we have simplified this picture and that gravitational torques do not trivially translate into matter flow (see §2.3 for a discussion of this). It is plausible, however, that the corresponding matter inflow is such that the radial profile will change over time. In the inner regions, the timescale for secular evolution is ~ 4 Gyr. The timescale depends linearly on V_{rot} and, as explained in §2.5, our model rotation curves differ in some cases by 20% to those found in the literature, which would lead to a 20% enhancement or reduction of the timescale.

The timescale is based solely on the torques due to the stellar distribution. In §2.4 the simulations showed that the dark matter distribution can also exert torques in the same direction as the stellar distribution. In the inner regions, the torques may be enhanced by as much as 20% and in the regions beyond $2\ r_{exp}$, the enhancement may be as much as 50%. The dashed line in Fig. 2.16 shows the effect of the dark matter enhancement using the enhancement factor derived from a fit of $\frac{\Gamma_{z,DM}}{\Gamma_{z,*}}$ in §2.4. Beyond $1\ r_{exp}$, the rate of angular momentum flow becomes considerably longer than a Hubble Time (Fig. 2.16). Thus, we expect that the radial profile will remain as formed beyond this position.

Given that the stellar profile in the inner regions may change as stars are funneled inward, our findings suggest that such a process may be effective in creating so-called pseudo-bulges (*e.g.* Kormendy & Kennicutt 2004), while the outer regions change little. In the simulations of Foyle et al. (2008) it was found that if a two-component profile develops in a galaxy, the outer disk scale length will remain true to the initial value, while the inner disk scale length will evolve over time to lower values as matter funnels inward to the bar and bulge. These observations substantiate the findings of their simulations. Simulations of Valenzuela & Klypin (2003) also showed that the matter exchange occurred solely in the very central regions of the galaxies (within 2 kpc).

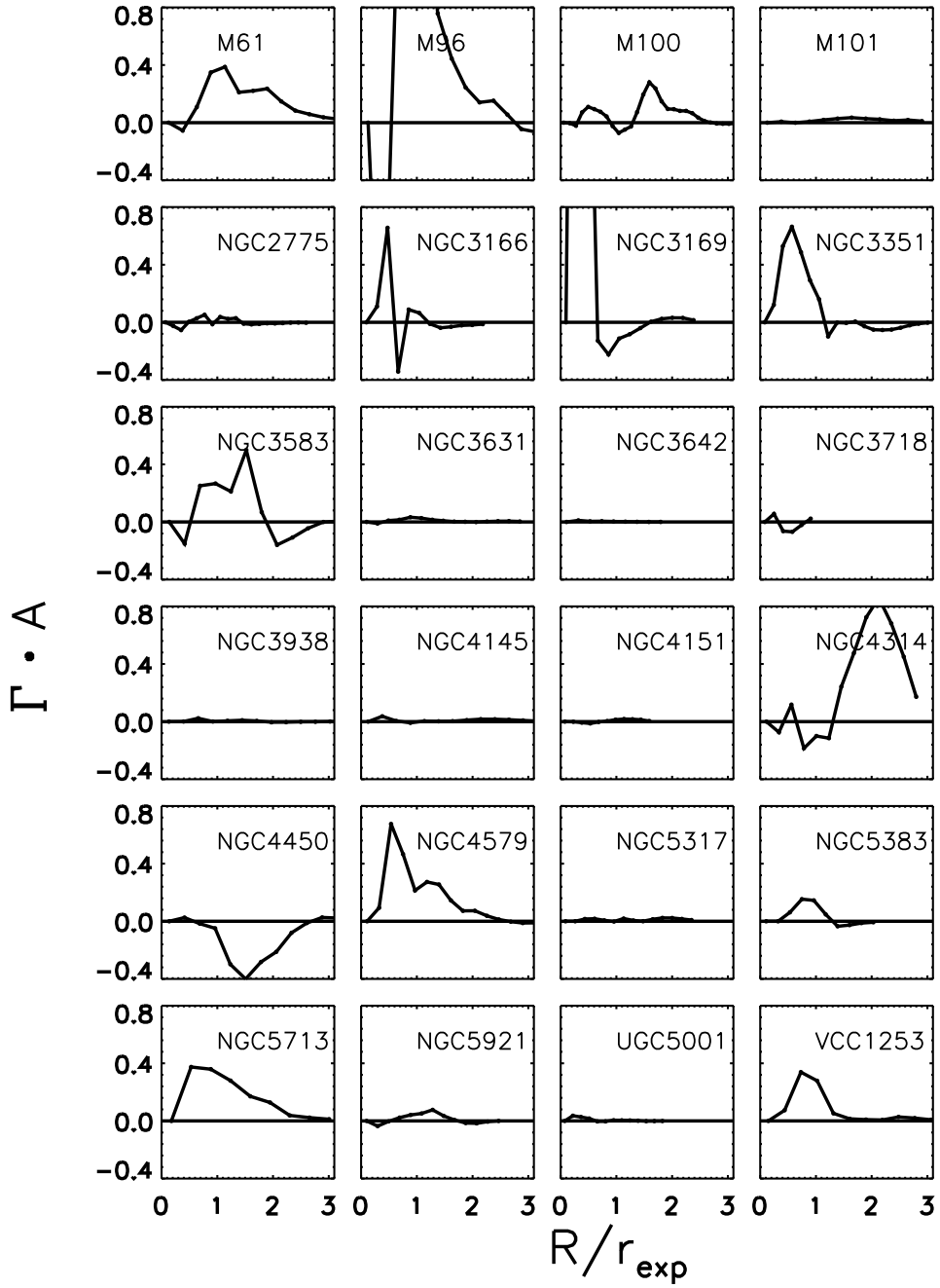

Figure 2.14: Torque profiles scaled by A, where $A = \frac{Gt_{Hubble}}{r_{exp}^2 V_{rot}^3}$. The peak values are listed in Table 2.2

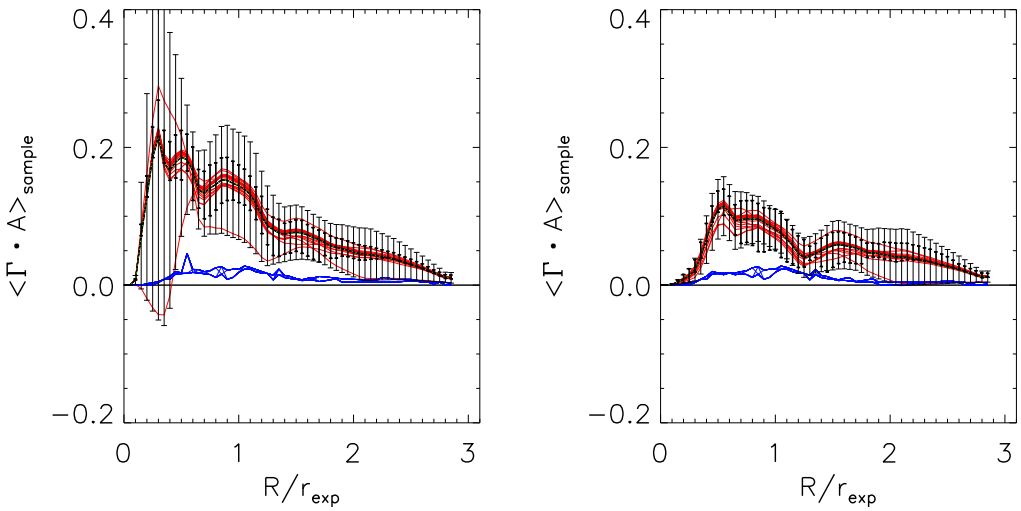

Figure 2.15: Mean torque profiles for the sample of 24 galaxies calculated (left) and for 22 galaxies (right). The red curves denote the jackknife iterations of the mean and the blue curves denote the jackknife iterations of the median. The long error bars show the jackknife σ and the short thick error bars show the 68% confidence limit. We see that the torque peaks in the inner part of the disk and that there is consistent angular momentum outflow and matter inflow within $3r_{exp}$.

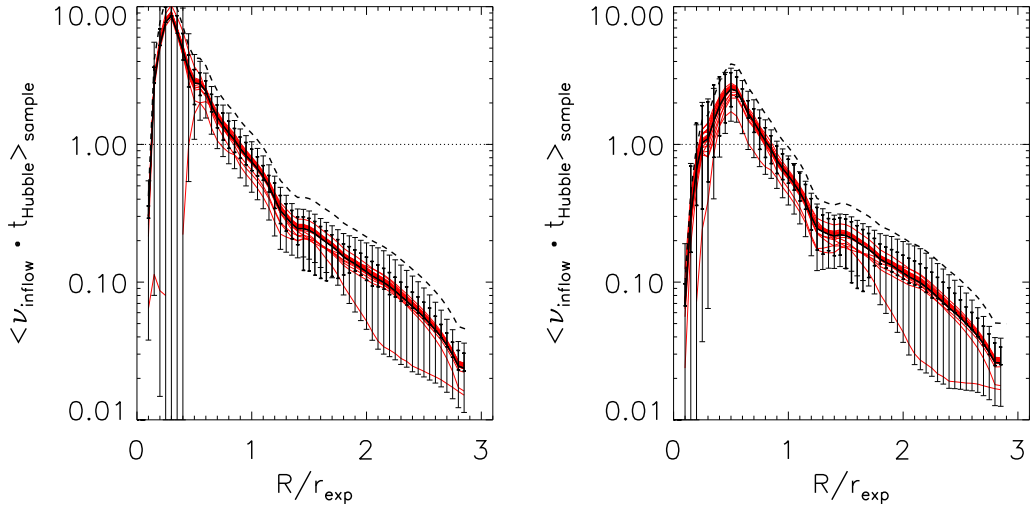

Figure 2.16: Mean $\nu_{inflow} \cdot t_{Hubble}$ profile for the sample of 24 galaxies (left) and for 22 galaxies (right). The red curves denote the jackknife iterations of the mean. The long error bars show the jackknife σ and the short thick error bars show the 68% confidence limit. We see that within $1r_{exp}$ the timescale for matter inflow is less than a Hubble Time. The dashed line shows the enhancement in the inner regions due to the dark matter torques, determined from the simulations in §2.4.

2.7 Conclusion

Previous studies that have addressed the significance of secular evolution due to gravitational torques have taken either a computational or theoretical approach (*i.e.* Lynden-Bell & Kalnajs 1972; Bertin 1983; Sellwood & Binney 2002, etc.). We present here a direct observation-based estimate for the long-term torque-driven angular momentum transport . We have extended and improved upon the work of G95, by using a larger sample of 24 galaxies and constructing accurate mass maps using g and i-band images from SDSS and a pixel-by-pixel mass-to-light ratio (Z09). These mass maps allowed us to derive instantaneous torque maps based on the stellar mass distribution and compute radial matter inflow profiles. We stacked the 24 inflow profiles scaled by disk scale length in order to use an ensemble average to bypass the time integral required to investigate the long-term strength of secular evolution.

We tested the validity of this approach using N-body/SPH simulations, where we verified that the torques due to the stellar distribution are stronger than those from the dark matter distribution. Thus, torques derived only from the stellar distribution are a conservative (lower) bound for the total torque and we derived a correction for the torques due to the dark matter distribution. We also verified that the uncertainties in deprojecting the galaxies, finding the centroid and determining the disk scale length were moderate.

For each galaxy in the sample we derived instantaneous torque profiles scaled by disk scale length. We translated these into angular momentum flow profiles. However, we did not include the effects of advective transport, since there is no way to measure these effects observationally. For the individual galaxies we found that there was consistently angular momentum outflow in the inner regions and the peak of each torque curve was within $1.5\ r_{exp}$. The ensemble properties of the stacked sample of 24 galaxies show that for typical present day spiral galaxies:

i) angular momentum is transported outward within $3\ r_{exp}$;

ii) within $1\ r_{exp}$ the torques lead to an angular momentum outflow timescale much less than a Hubble Time;

iii) the average angular momentum flow timescale in this inner region is ~ 4 Gyr;

iv) beyond $1\ r_{exp}$ the timescale is much longer than a Hubble Time, implying that the stellar radial profile has largely remained unchanged.

In conducting this study we have found that accurate mass maps are central in properly determining the torques due to the stellar distribution. Global mass-to-light ratios (*e.g.* scaled i-band images) are not sufficient and pixel-by-pixel mass-to-light ratios ensure that the total mass is properly estimated and that regions with young, blue, luminous populations, like spiral arms are not over-weighted (Z09).

Our results show that for spiral galaxies as a class, secular evolution is *observed* to be important within one disk scale length and may lead to the formation of pseudo-bulges. Beyond

one disk scale length however, the timescales are such that little to no change in the radial profiles should be expected. We stress that our simple picture must be qualified since advective transport and the fact that angular momentum flow does not directly translate into matter flow has not been treated.

Chapter 3

Arm & Interarm Star Formation

This chapter is based on the paper "Arm & Interarm Star Formation" by K. Foyle, H.-W. Rix, F. Walter and A. Leroy, submitted to ApJ.

Abstract

*We investigate the relationship between spiral arms and star formation in the grand-design spirals NGC 5194 and NGC 628 and in the more flocculent spiral NGC 6946. Filtered maps of near-IR (3.6μm) emission allow us to identify "arm regions" that should correspond to regions of stellar mass density enhancements. The two grand-design spirals show a clear two-armed structure, while NGC 6946 is more complex. We examine these arm and interarm regions, looking at maps that trace recent star formation — far-ultraviolet (GALEX NGS) and 24μm emission (*Spitzer *SINGS) and cold gas — CO (HERACLES) and HI (THINGS). We find the star formation tracers and CO more concentrated in the spiral arms than the stellar 3.6μm flux. If we define the spiral arms as the 25% highest pixels in the filtered 3.6μm images, the majority (60%) of star formation occurs in the interarm regions. However, even with a generous definition of the arms, interarm regions still contribute at least 30% to the integrated star formation rate tracers. We look for evidence that spiral arms trigger star or cloud formation using the ratios of star formation rate (SFR, traced by a combination of FUV and 24μm emission) to H_2 (traced by CO) and H_2/HI. Any enhancement of SFR / M(H_2) in the arm region is very small (less than 10%) and the grand-design spirals show no enhancement compared to the flocculent target. Arm regions do show a weak enhancement in H_2/HI compared to the interarm regions, but at a fixed gas surface density there is little clear enhancement in the H_2/HI ratio in the arm regions. Thus, there is little evidence that spiral shocks play a key role in aiding molecular cloud formation beyond the mere concentration of gas to the arms.*

3.1 Introduction

Optical images clearly reveal that spiral arms in present-day disk galaxies harbour a concentration of young stars, implying that star formation rate densities must be higher in the arm regions

than elsewhere in the galaxy. There have been many attempts to understand the connection between star formation and spiral arms and, given the variety of spiral structures observed, it is likely that more than one model may be required to explain observations. We can distinguish between two types of spiral structure. In the first, the entire disk participates in the spiral pattern and is thus well-defined in all bands so that it is not only associated with young, star-forming regions, but also the underlying mass density (Eskridge et al. 2002; BT08). The second type has a spiral pattern that is not well-defined and is seen only in the optical bands, with little presence in redder bands commonly used to probe the stellar mass density (Elmegreen & Elmegreen 1984; BT08; Zibetti et al. 2009). Typically one finds the former in so-called 'grand-design' spirals with two-arm symmetry and the latter in flocculent spirals with multiple, short, spiral segments.

In the case of the grand-design spirals, the underlying variations in the stellar mass density may simply lead to the reorganization of the ISM (*e.g.* Elmegreen 1995 and Elmgreen & Elmgreen 1986). The gas is drawn toward the mass enhancements, which define the arm areas and is retained for a longer time due to Coriolis forces. High star formation rates in the arm areas may only be due to the higher gas densities and the star formation rate per unit gas mass, or star formation efficiency is the same throughout the disk. However, spiral arms could conceivably do more. As first proposed by Roberts (1969) and extended by others (*e.g.* Roberts et al. 1975; Gittins & Clarke 2004), the spiral arm mass density enhancement could act to directly trigger star formation by a shock forming along the trailing edge of the spiral arm inside corotation when the relative velocity between the interstellar medium and the density wave is supersonic. The shock compresses the gas, which leads to star formation and one would expect the star formation rate per unit gas mass to be higher in the spiral arms than the interarm regions. We will refer to this last scenario as the 'triggering model'.

In the more flocculent spirals without a pattern in the stellar mass density, or only a very weak one (Thornley 1996; Kuno et al. 1997), much of the spiral pattern seen in optical images is a consequence of sheared, stochastic star formation (*e.g.* Seiden & Gerola 1979 and Elmegreen et al. 2003). In this way, star formation causes the spiral pattern to emerge. Stars form in small patches and are sheared into a spiral pattern by differential rotation.

Our ability to decipher which of these scenarios is most important is complicated by several factors. It is difficult to define the spiral arm regions and it is still unclear whether they are long-lived, quasi-stationary structures or short-lived, transient structures (Sellwood 2010). Moreover, the timescales for the stages of star formation are not well-known and we do not have direct measures of the star formation rates and star formation efficiencies.

To assess empirically how spiral arms affect star formation, we provide two key pieces of information; first, the fraction of star formation that occurs in the arms, as opposed to the interarm regions; second, whether the star formation efficiency (SFE) is higher in the arms as opposed to the interarm regions. Few studies have attempted to address the former and have focused on the latter. The amount of star formation in the interarm region is very important in order to assess how relevant spiral arms are in the overall production of stars in galaxies.

If the fraction of star formation in the arms were modest, the effect of spiral arms on the net production of stars would still be small irrespective of any triggering. Our sample includes three galaxies, two grand-design spirals and a more flocculent spiral, allowing us to explore the range of possible models. We first review some of the previous works, which have largely focused on grand-design spirals and whether or not the spiral arms directly trigger star formation.

Elmegreen & Elmegreen (1983) examined 34 spiral galaxies in the blue and near-infrared bands and found that the blueness of the arms was independent of the arm amplitude. The triggering model would predict that higher arm strengths and hence shock strengths should lead to higher star formation rates and thus more young, blue stars. The lack of such a correlation supports the reorganization model. However, Seigar & James (2002) used individual galaxy estimations of the spiral arm shock strengths and found a coupling with the Hα-based star formation rates (SFR).

The triggering model also predicts that grand-design spirals should have higher star formation rates than their non-grand-design counterparts and that the properties of the arms, including width and pitch angle, should be correlated with Hubble Type. Elmegreen & Elmegreen (1986) found that the galaxy-averaged star formation rates determined from Hα and UV fluxes showed no difference for galaxies with or without grand-design spirals. However, for M51, Vogel et al. (1988), found that the SFE in terms of Hα and CO was higher in the arm region, but that only 25% of the CO emission was found in the arms. As a result of this small fraction of gas in the arms, even a strong enhancement in the on-arm SFE will weakly affect the integrated SFE of the galaxy. Kennicutt & Hodge (1982) and Seigar & James (1998) found that correlations between arm properties and Hubble type did not match the predictions of the triggering scenario.

There have been many studies of the arm versus interarm star formation efficiency, particularly for M51. Studies of M51 by Lord & Young (1990) have found that the star formation efficiency expressed as Hα/CO was higher in the arm regions versus the interarm regions. Conversely, Garcia-Burillo et al. (1993) claimed that arm-interarm contrasts of CO in M51 can be explained by orbit crowding and that triggering need not be invoked. Rand & Kulkarni (1990) studied giant molecular associations via CO measurements in the arm and interarm regions of M51 and found that these associations were found in both regions, but only those in the arms were bound. This suggests that the density wave may trigger the formation of molecular gas, but may not trigger star formation or enhance the SFE. Koda et al. (2009) also detected molecular gas throughout the disk and the giant molecular associations were interpreted to be forming due to streaming motions as they approached the arms and were then fragmented due to shear as they left the arms.

Beyond M51, a handful of other galaxies have also been studied. Knapen et al. (1996) found that the arm regions had SFEs three times higher than the interarm regions for NGC 4321 in terms of Hα/CO. Cepa & Beckman (1990) reported higher star formation efficiencies in the arm regions for NGC 6946 and NGC 628 using Hα and HI maps. It is important to note though that the SFE in terms of HI and CO (molecular gas) are likely to be quite different. Leroy et al.

2008 (hereafter L08) and Bigiel et al. 2008 (hereafter B08) have found that the star formation rate is not correlated to the HI distribution but rather the molecular gas. Thus, it is important to distinguish whether the SFE is associated with the total gas, HI or H_2. When comparing these studies, it is also important to examine closely how the spiral arms are defined. In some cases, dust lanes are used and in other cases optical or near-infrared images are used. Clearly, defining the spiral arms using a tracer sensitive to regions of recent star formation may lead to erroneous measures of high SFE. Thus, it is important to probe the underlying density enhancement when defining the spiral arms.

The recent work by L08 and B08 has shown that the star formation efficiency of H_2(SFE= SFR/M(H_2)) alone is constant to first order for nearby disk galaxies on a pixel-by-pixel basis. However, they did not explore specifically whether the SFE might vary in the arm versus interarm regions. In light of the recent increase in multiwavelength data for nearby galaxies from surveys including GALEX (Gil de Paz et al. 2007), SINGS (Kennicutt et al. 2003), THINGS (Walter et al. 2008) and HERACLES (Leroy et al. 2009), it is timely to explore how much and how efficiently star formation happens in the arm and interarm regions.

Looking at the nearby galaxies with prominent spiral arms, we first focus on observable tracers of star formation and gas and ask what fraction of them lies near spiral arms. We then use the tracers to estimate the SFR and SFE and examine if there are any differences in the arm and interarm regions. We also examine whether the fraction of molecular gas, (M(H_2)/M(HI)), is enhanced in the arm and interarm regions in order to determine if the arms are triggering molecular gas formation. In §3.2 we describe how the images are processed and how the spiral arms are defined. In §3.3 we examine how concentrated the star formation and gas tracers are in the spiral arms relative to the stellar mass density and infer the amount of interarm star formation. In §3.4 we transform our observables into estimates of the star formation rate and star formation efficiency in the arm and interarm regions and compare these regions. In §3.5 we compare the fraction of molecular gas in the arm and interarm regions and specifically if it is enhanced relative to other gas of similar surface density. In §3.6 we calculate the fraction of diffuse 24μm emission for our sample. We summarize our conclusions in §3.7.

3.2 Analysis

We chose three galaxies, two grand-design (NGC 628 and NGC 5194) and one more flocculent (NGC 6946) on the basis of their proximity, orientation and multiband data. These have coverage in GALEX (NUV+FUV) (Gil de Paz et al. 2007), THINGS (Walter et al. 2008), SINGS (Kennicutt et al. 2003) and HERACLES (Leroy et al. 2009).

In order to quantify the amount of star formation in the arm and interarm regions, we focus on a series of observables: 24μm emission, which traces young, dust-enshrouded stars; UV emission, which traces young, unobscured stars; CO, which traces molecular gas that is presumably organized into giant molecular clouds; and HI gas, which is presumably a mixture of

Table 3.1: Sample Properties: The inclination and position angles used to deproject the galaxies and the inner and outer radii in $''$ and kpc defining the region of the analysis are listed.

Name	inc	PA	R_{in}	R_{out}	R_{in}	R_{out}
	[°]	[°]	[$''$]	[$''$]	[kpc]	[kpc]
NGC 5194	20	172	20	95	0.8	3.7
NGC 628	7	20	30	76	1.1	2.7
NGC 6946	33	243	20	107	0.6	3.1

warm and cold, atomic, diffuse gas. Each of these probes a different stage in the star formation process. However, none of them uniquely define the star formation rate as other sources may contaminate or attenuate the emission. The 24μm emission, especially in the interarm regions, may also arise from diffuse emission not associated with recent star formation (cirrus 24μm emission) (Helou 1986; Calzetti et al. 2007). The FUV, on the other hand, may be attenuated by dust in the arm regions (Kennicutt 1998; Calzetti et al. 2007). Taken together, these two effects could potentially boost the relative amount of star formation in the interarm regions. Fortunately, CO measurements, which trace the molecular gas component, *i.e.* the fuel for star formation, can also be used to further probe the amount of star formation in the interarm regions, if we assume that the relations found by B08 and L08 indeed hold. We first describe the steps taken to render the images for our analysis as well as how the arm and interarm regions are defined in the following subsections.

3.2.1 Images

All of the images are aligned to the THINGS astrometric grid and degraded to a common resolution of 13$''$ FWHM, which is the resolution of the HERACLES CO images. Before this degradation, we remove foreground stars from the far-UV, 24μm and 3.6μm images using their UV colour. Pixels, with an NUV-to-FUV intensity ratio between 9 and 25, depending on the galaxy, are blanked. We also require that the cut pixels have values greater than 5σ in the NUV map. The companion of NGC 5194 is removed by-eye, and is beyond the radius considered in the analysis. All images are eventually deprojected to face-on according to the values found in Walter et al. (2008) and listed in Table 3.1.

UV, 24 μm & SFR Maps

As in L08 and B08, we remove a residual background from the FUV and 24μm images, measured as a median value in an off-galaxy box. Stars are removed using the NUV-to-FUV ratio and the UV images are corrected for galactic extinction (Schlegel et al. 1998) using the E(B-V) values listed in NED, which are 0.07, 0.035 and 0.342 for NGC 628, NGC 5194 and NGC 6946, respectively. The UV and 24μm images are then combined to produce SFR maps (see Appendix of L08):

$$\Sigma_{SFR} = (8.1 \times 10^{-2} I_{FUV} + 3.2 \times 10^{-3} I_{24}), \tag{3.1}$$

where Σ_{SFR} has units of $M_\odot$ kpc^{-2} yr^{-1} and the FUV and 24 μm intensity are each in MJy ster^{-1}.

HI, CO & Gas Maps

We use 21 cm line emission from THINGS to trace the atomic gas. We convert the integrated intensity to a surface density and include a factor of 1.36 to account for helium, following L08. We use integrated CO $J = 2 \rightarrow 1$ intensity maps from HERACLES (Leroy et al. 2009) to estimate the distribution of H_2. For M51 this is a reprocessing of the maps presented by Schuster et al. (2007) and Hitschfeld et al. (2009) (the reprocessing does not significantly alter the map). To estimate the surface density of H_2 from CO we use a constant conversion factor. As in L08 we adopt:

$$\Sigma_{H_2}[M_\odot pc^{-2}] = 5.5 I_{CO}(2 \rightarrow 1)[Kkms^{-1}] \tag{3.2}$$

The maps are deprojected and added together to form total gas density maps.

The CO-to-H_2 conversion factor is a source of uncertainty. It should, in principle, be a function of (at least) metallicity, radiation field, density, and temperature and at least some of these conditions may change between the arm and interarm regions. However, direct evidence for conversion factor variations in our targets is mixed and often contradictory (*e.g.* Garcia-Burillo et al. 1993). For a detailed discussion see Schinnerer et al. (2010). The fact that the studies of L08 and B08 showed striking agreement of different galaxies in the 'Schmidt Law' plot (plotting SFR surface densities vs. gas surface densities) provides further confidence that the X_{CO} conversion factor is roughly constant for the systems studied here. Thus, we use a constant X_{CO} in our analysis.

3.2.2 Defining Spiral Arms

It is clear that we should define the arm and interarm regions in a way that is least biased by the young stellar population. Ideally, we wish to define the spiral arms using the stellar mass density, or at least the old stellar population. Near-infrared images have commonly been used for this purpose (*e.g.* Elmegreen & Elmegreen 1984; Rix & Zaritsky 1995; Seigar & James 1998; Grosbøl et al. 2004 and Kendall et al. 2008). We use the 3.6μm images from the IRAC instrument on Spitzer (Kennicutt et al. 2003) to trace the underlying old stellar population. In this band most of the emission is due to old stars although there is some patchy contamination from hot dust and PAH features (*e.g.* Kendall et al. 2008). Zibetti et al. (2009) provide a much improved algorithm for mapping out the stellar mass density, which makes use of multi-band images. However, here we do not require the exact amplitude of stellar mass density variations,

but only the location of mass density enhancements to define the *location* of spiral arms.

Foreground stars in the processed 3.6μm images are removed according to the UV color cut described above and the images are deprojected according to the values in Table 3.1. In order to make the 3.6μm surface brightness variations a better approximation to the *location* of stellar mass density enhancements, we apply some spatial filtering. The 3.6μm images are first median-filtered over 20 pixels ($\approx$1 kpc) to remove bright spots and features. The filtered image is then Fourier-decomposed in ϕ with radial bins that overlap to obtain a version of the image that consists of the m=6 component divided by the m=0 component. This spatially filters the images, which are shown in Fig. 3.1. We note that the grand-design spirals, NGC 5194 and NGC 628, have spiral arms that were well-defined using only the m=4 component divided by the m=0 component and that moving up to m=6 leads to little, if any, difference. However, in the more flocculent spiral, NGC 6946, the 3.6μm structure is more complex, requiring an extension to m=6.

The inner bulge regions, where no spiral arms are evident, are masked out in each galaxy. The outer limit is set by the area over which the CO maps detect emission. The inner and outer limits for each galaxy are listed in Table 3.1. The image is then divided into radial annuli each of 7.5$''$ width. We chose a width below the resolution of the image in order to ensure overlapping radial bins, which produce a more continuous spiral arm structure in the masks. In each annulus, the 'arm region' is defined to be the area covered by a certain percentage of the highest-value pixels (*e.g.*, the brightest 30%). In a similar fashion, the 'interarm region' is defined as the area covered by the same percentage of the lowest-value pixels. We will vary the exact percentage used to define these regions over the range 10–50% to ensure conclusions robust to the precise arm definition. We refer to the percentage used to define the arms as the 'arm pixel fraction'. Once both the arm and interarm regions each consist of 50% of the pixels, the entire surface area is covered.

Fig. 3.1 shows the 3.6μm image (far left) and the Fourier reconstructed m=6 image divided by the m=0 (second from left) with contours overlaid showing the arm regions (white). The spiral arm masks (second from right) for our sampl,e where the arm regions are defined from the 45% highest pixels per radial bin, are also shown as is the 24μm image with arm contours overlaid for comparison.

3.3 Star Formation & Gas Tracers in the Arm and Interarm Regions

Having defined the arm and interarm regions, we now can assess what fraction of star formation tracers is found in the respective regions. To do so, we measure the fraction of the total emission from gas and star formation tracers that are contained in the arm regions for the area considered (see Table 3.1 for inner and outer radii). We make this measurement for a variety of arm pixel fractions. We examine the HI, H_2 (as traced by CO), total gas, FUV, 24μm, SFR and the stellar

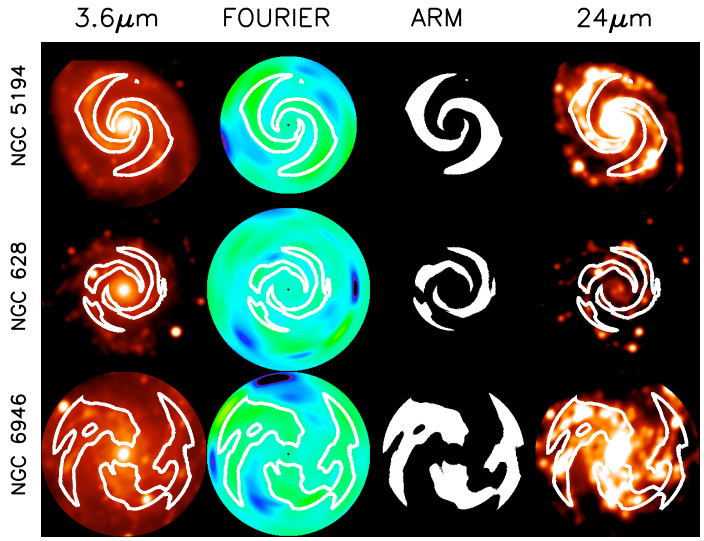

Figure 3.1: Identification of arm and interarm regions. The 3.6μm image (left) and the Fourier reconstructed m=6 image divided by the m=0 component (second from left) with contours showing the arm (white) regions for NGC 5194, NGC 628 and NGC 6946. The arm (second from right) regions are defined by the 45% highest pixels in radial annuli of the m=6 component divided by the m=0 component of the Fourier reconstructed 3.6μm image. The 24μm image (right) is shown with the arm contours of overlaid (white).

mass surface density. The plots in Fig. 3.2 show the fraction of the overall emission found in the arm regions, as a function of the arm pixel fraction.

Fig. 3.2 a) shows the flux fraction for different tracers that occur in the arm region as a function of the pixel fraction used to define the arm region. To emphasize the difference between the curves, we have divided by the expectation of a spatially uniform distribution and shown them in b). The 3.6μm image is included in all panels for ease of comparison. The thin black line in a) denotes what would be expected for an azimuthally uniform distribution. In b), an azimuthally uniform tracer would be a horizontal line (flux enhancement = 1). For ease of comparison in our discussion we use a fiducial pixel fraction of 45% to define the arms.

Fig. 3.2 shows that all tracers are much more concentrated to the spiral arms than a uniform distribution (*i.e.* all values are above unity in panel b)). For the 3.6μm image this is by construction, as the wavelength was used to define the arm regions. However, Fig. 3.2 shows that all the tracers of star formation are even more concentrated. Once a sufficient fraction of pixels in the arm regions is enclosed, the 24μm emission is more concentrated to the spiral arms than the UV emission. UV emission is presumably less concentrated in the arms than 24μm, because dust extinction suppresses UV emission in the arms and because UV is a more 'long-lived' SFR tracer than 24μm. The effect is most pronounced for the two grand-design spirals, NGC 5194 and NGC 628. Similarly, the H_2 (CO emission) is more concentrated to the spiral arms than the HI. The HI is the least concentrated to the arms.

Figure 2 a) shows that, even for high arm pixel fractions, at least 30% of emission from star formation tracers are found in the interarm regions for galaxies which were chosen for the prominence of their spiral arms. We also note that both NGC 628 and NGC 5194 are grand-design spirals, which should, in principle, exhibit the highest fraction of star formation in the arms, if grand-design spirals have the strongest arms and shocks. Assuming that the combination of 24μm and UV emission is an accurate description of the star formation rate, these plots also show that at least 30% of the star formation is occurring in the interarm region, even if the definition of the spiral arm encompasses 45% of the total area in a radial bin. Thus, while spiral arms are important sites of star formation, star formation occurs throughout the disk in the interarm regions as well.

One concern is that the interarm SFR tracer emission is due to stars which have drifted from the spiral arms. If this were the case, one would expect offsets between the different star formation tracers, which reflect the timescales in the star formation process. In Chapter 4, we examine whether there are angular offsets between these tracers. For these three galaxies we found no evidence for such offsets between any of the tracers considered here. Previous works, including Tamburro et al. (2008), found offsets to be very small, between HI and 24μm (five degrees), which imply timescales between these two stages of less than 4 Myr (Tamburro et al. 2008). Given this, any drifted emission would be well within our broad definition of spiral arms, which encompasses and ever-increasing area.

Another concern is that given the resolution of 13″, some flux physically arising in the arm region may cause the arm flux to infiltrate the interarm flux. In Fig. 3.3 we examine how resolution may affect our results. We apply our analysis to 24μm maps of NGC 5194 at 6″ and 13″ resolution to examine the strength of this effect. We find that at small radii, this may lead to an overestimate of the star formation by as much as 10%, depending on the choice of arm mask; at larger radii, the effect rapidly diminishes. Due to this, for most comparisons we choose a pixel fraction of 45% to define the arms. Unless otherwise stated, one can assume this.

We also examine the effects of possible pointing errors in the CO maps. The HERACLES maps have been found to have offsets from BIMA SONG maps by less than $\pm 2''$ in RA and DEC. In Fig. 3.4 we compare the results of a CO map shifted by 3″ in both x and y to the original map. We find that the differences are minor and certainly less than those incurred by the resolution.

3.4 The Star Formation Efficiency in the Arm and Interarm Regions

Having addressed the relative fractions of arm and interarm star formation, we now turn to exploring whether the SFE of H_2 differs in the arm and interarm regions. L08 found that the SFE of H_2 of spirals was roughly constant with a median of $5.25 \pm 2.5 \times 10^{-10}$ yr^{-1}. Furthermore, L08 found no trends of the SFE with any macroscopic properties considered, including radial

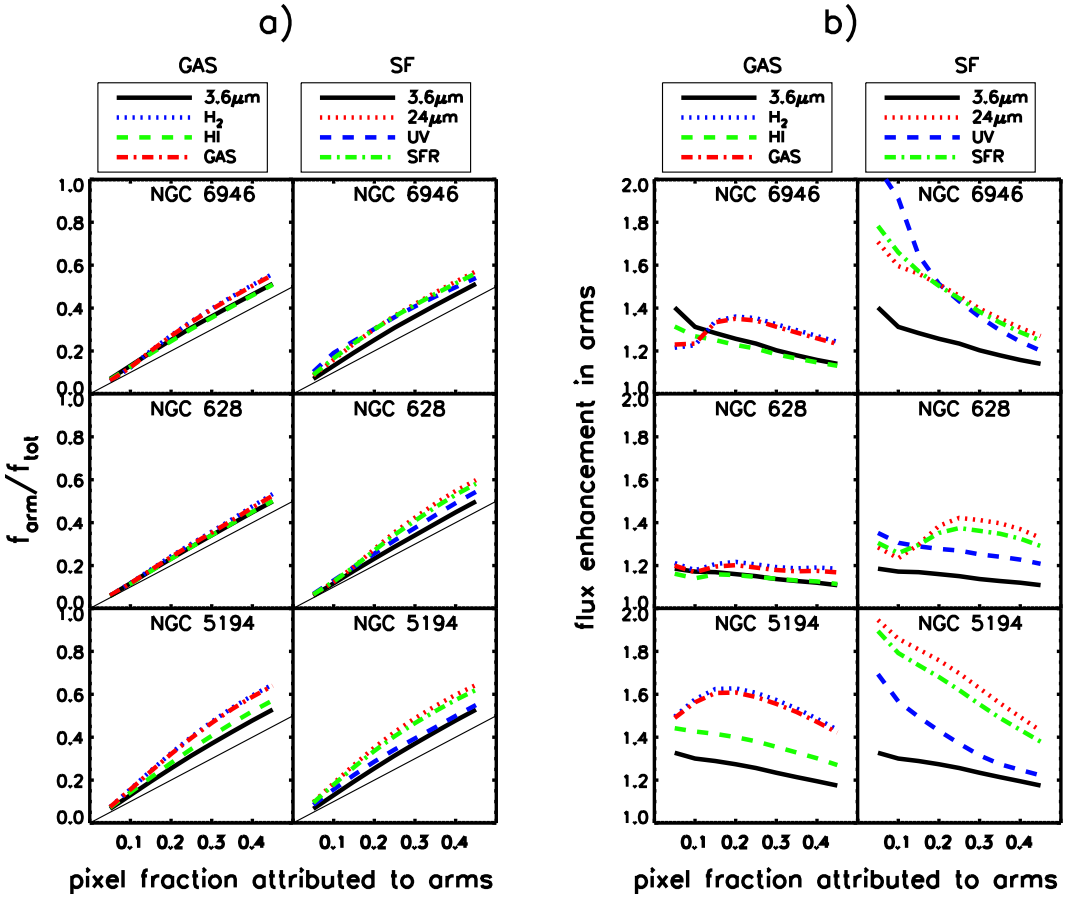

Figure 3.2: Concentration of 3.6μm light, gas and SFR towards spiral arms. Fraction of total flux in each tracer in the arm regions (a) and the enhancement over a smooth distribution (b) (*i.e.* the curves in panel (a) divided by the thin black line). The gas distributions are shown on the left columns of both panels and the star formation tracers are shown on the right columns for NGC 6946 (top), NGC 628 (middle) and NGC 5194 (bottom). A uniformly distributed tracer is represented as a the thin black line in a); in b), such a distribution would be a horizontal line at value 1.0. The tracers are concentrated to the spiral arms, yet an appreciable fraction of the flux must lie in the interarm region (at least 30% even when 45% of the pixels, the last plotted pixel fraction in these plots, are enclosed in the spiral arms). The 24μm emission is more concentrated to the spiral arms than the UV emission and the H_2 emission is more concentrated to the spiral arms than the HI emission.

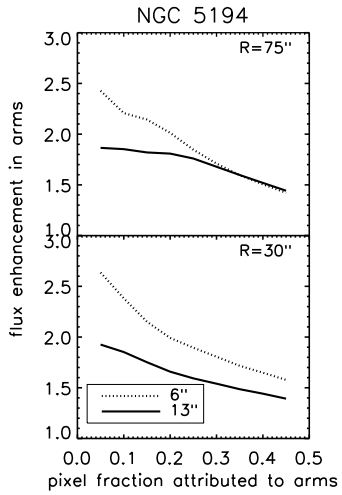

Figure 3.3: The effect of spatial resolution on our estimates of interarm star formation tracers. We use 24μm maps of NGC 5194 at a resolution of 6$''$ and our common image resolution 13$''$. We measure the enhancement of 24μm in the arms to the total versus the fraction of pixels enclosed in the maps. At small radii (bottom), the lower resolutions bleed into the interarm area ($\approx$ 1kpc). At larger radii (top), the effect quickly weakens once a sufficient number of pixels are part of the arm definition ($\approx$ 2.5 kpc).

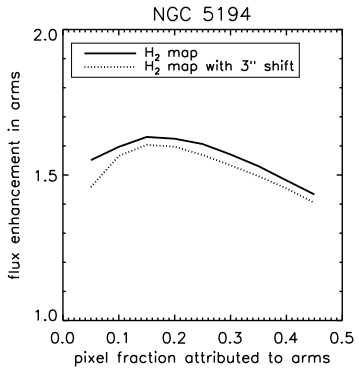

Figure 3.4: The effect of finite pointing errors on H_2 maps. We compare the results for the original H_2 map for NGC 5194 with one that has been shifted by 3$''$ in both x and y. We find that the effects of pointing errors are small and less than resolution effects.

position, gas and stellar surface density, orbital timescale, gas pressure and the slope of the rotation curve. Previous studies by Lord & Young (1990), Cepa & Beckman (1990), Seigar & James (2002), etc. found evidence for triggering in spiral arms based on color differences, enhanced star formation rates or star formation efficiencies. If spiral arms were shocking the molecular gas to produce stars with increased efficiency, then one would expect an increase of the SFE of H_2 in the arm region in comparison to the interarm region. As L08 did not explore possible differences in the SFE(H_2) in these regions, we examine this question here.

We first created molecular SFE maps using our SFR maps and H_2 maps for our sample (see Fig. 3.5, where we have blanked pixels where the H_2 map has values less than 4σ). For display purposes, we have increased the contrast of these images as much as possible and have overlaid in green the spiral arm regions as defined by 45% of pixels. It is important to note that in the inner regions the SFR is dominated by the contribution from 24 μm emission and even in the outer parts it is dominate for M51. Since we have restricted our analysis to the inner regions of the galaxies (see Table 3.1), our SFE is mostly determined from the CO and 24μm emission. The SFE maps in Fig. 3.5 exhibit no obvious spiral pattern.

Fig. 3.6 compares the SFE(H_2) in the arm and interarm regions for our sample. We compare the median values of the SFE(H_2) at different radial annuli for the arm and interarm regions. For NGC 628 and NGC 5194, the variation is very small between the arm and interarm regions and is certainly less than the variation across the radial annuli. For NGC 6946, the arm region has a higher SFE than the interarm region, particularly at larger radii (less than a factor of 2).

In Fig. 3.7 we show histograms of the pixel values in the total image (dotted), arm (solid) and interarm (dashed) regions. Once again, we find that there is little difference between the arm and interarm regions for NGC 5194 and only a slight difference for NGC 628. However, NGC 6946 shows an excess of higher SFE(H_2) pixels in the arm regions (*i.e.*, there are 33% more pixels with a SFE value higher than 6×10^{-10} yr^{-1} in the arm regions versus the interarm regions).

One would expect that the grand-design spirals would show the highest SFE in the arms as opposed to flocculent galaxies, as here the spiral shocks should be strongest. It is interesting then that NGC 6946, the most flocculent galaxy in this study, seems to show a higher SFE in the arms. While the source of this is not clear, one possible explanation is that our spiral arm definition is not probing the underlying density enhancement for this galaxy, since it is very weak. Instead the spiral arm mask has isolated regions of high star formation. Looking at the spiral arm masks (see Fig. 3.1), it is clear that the spiral arm structure is much more complex than the grand-design structures of NGC 628 and NGC 5194. If the arms were defined based on young, recent star forming regions, then it would be biased towards high SFRs and hence show seemingly higher SFE in the arm regions for NGC 6946. In order to be able to compare the SFE in the arm and interarm regions it is essential to have a definition of the arms that is not determined by episodes of recent star formation.

Thus, at least for the two grand-design spirals, NGC 628 and NGC 5194, we find that the

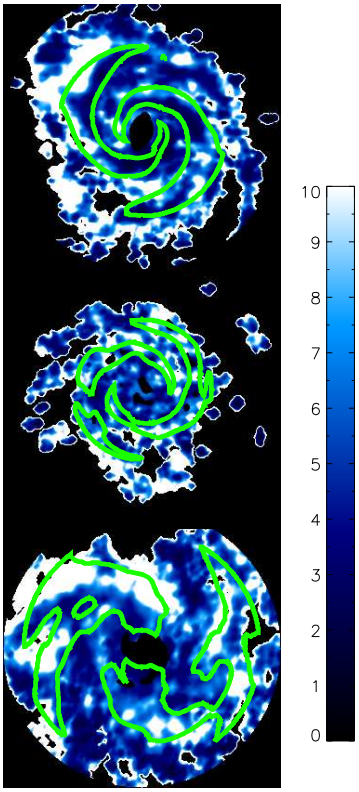

Figure 3.5: The SFE for H_2 for NGC 5194 (top), NGC 628 (middle) and NGC 6946 (bottom). Regions of high SFE are shown in white and low SFE are shown in blue. The green contours show the spiral arm regions defined by 45% of pixels. Pixels where the H_2 maps had values less than 4σ were blanked. The colorbar has units of 10^{-10} yr^{-1}.

SFE based on the molecular gas component is not enhanced in the arm region. Previous studies (*e.g.* Vogel et al. 1988; Lord & Young 1990; Cepa & Beckman 1990; Seigar & James 2002) claim to find an enhancement of the SFE in the arm region, but they used a different definition of the SFE than the SFR/H_2 than we use here. Most studies have looked at the SFE in terms of Hα and HI. As we saw in the previous section, the HI is far less concentrated in the spiral arms and is much closer to an even distribution. Thus, it is not surprising to find an enhancement in the SFE in the arms, based on such a measure.

Combined with our previous result that at least 30% of star formation occurs in the interarm regions, we find no significant evidence for shock-triggered star formation by spiral arms. The high star formation rates in the arms can be attibuted to the reorganization model. However, this does not preclude the possibility that the transition between atomic, neutral gas to molecular gas may be triggered by the passage of the spiral arm. Indeed, the fact that the molecular gas is much more concentrated than the HI, suggests this to be the case. Thus, we now examine if there are differences between the arm and interarm molecular gas fraction.

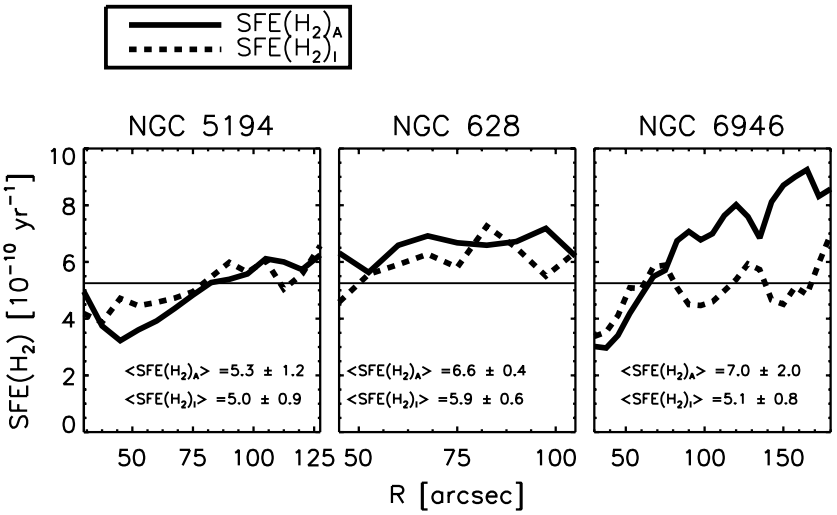

Figure 3.6: The median value of the molecular SFE at different radii in the arm (solid) and interam (dashed) regions for NGC 5194 (left), NGC 628 (middle) and NGC 6946 (right). The median values over the whole galaxy are listed at the bottom of the figure. The arm and interarm regions were chosen using the masks enclosing 45% of pixels. The line shows the median value found by L08.

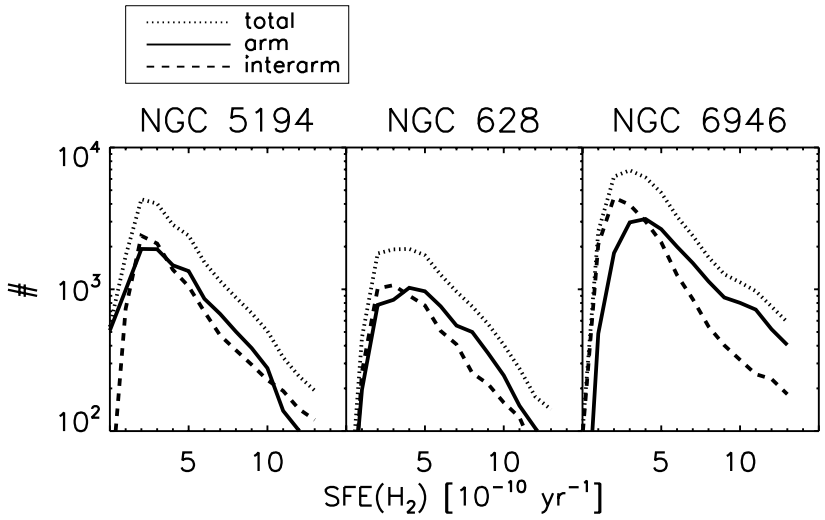

Figure 3.7: Distribtuion of the pixel-by-pixel molecular SFEs for the total image (dotted), arm (solid) and interarm (dashed) regions for NGC 5194 (left), NGC 628 (middle) and NGC 6946 (right). The arm and interarm regions were chosen using the masks enclosing 45% of pixels. We see that NGC 6946 shows an excess of higher SFE pixels in the arm regions.

3.5 Molecular Gas Fraction

Although we do not find an enhancement in the SFE of H_2, especially for the grand-design spirals, Fig. 3.2 does show an enhancement of H_2 relative to HI in the arms. This could be the result of molecular cloud formation triggered by spiral arms, but this does not have to be the case. Arms represent concentrations of total (H_2+HI) gas. The fraction of gas in the molecular phase is a strong function of both the total gas surface density and the midplane average volume density (*e.g.*, Blitz & Rosolowsky 2006; L08; Krumholz & Matzner 2009). We now examine if there is evidence for an enhancement in the molecular gas in the arms and if this enhancement is independent of higher total gas surface densities in the arms.

Fig. 3.8 shows how the fraction of molecular gas, H_2/HI, varies with radius when considering all pixels (black), those attributed to the arms with the 45% mask (red) and those attributed to the interarm regions (blue). For each galaxy and radius, we find the median H_2/HI ratio in the arm regions is enhanced compared to both the interarm regions and overall trend. The magnitude of this enhancement is small, less than a factor of 2.

Is this mild enhancement in the H_2/HI ratio the result of shock-triggered molecular cloud formation or simply the enhancement of the local gas content? Fig. 3.9 shows the fraction of molecular gas, but this time in terms of the total gas surface density. We see that the arm regions have molecular gas fractions that extend up to very high total gas fractions and that the interarm regions have molecular gas fractions only at the lower end of the total gas surface density. However, the two overlap and there is no obvious enhancement of the molecular gas fraction in the arms for a given total gas surface density.

Thus, arms appear to concentrate gas to higher surface, and presumably volume, densities. However, there is not strong evidence that arms trigger the formation of H_2. Moreover, at a given gas surface density, the molecular gas fraction in the arm and interarm regions is about the same. Combined with our SFE results, this suggests triggering by arms is not critical to the main star formation processes. Arms may drive the formation of molecular gas by bringing the total cold gas to high surface densities, but we do not see clear evidence that spiral shocks are contributing to form either clouds or stars.

3.6 Conclusion

We have used three spiral galaxies (NGC 5194, NGC 628 and NGC 6946) to determine the fraction of star formation and cold gas found in the interarm regions of spiral galaxies. We based our definition of the spiral arm areas on stellar mass density enhancements traced by 3.6μm images. We find that at least 30% of the emission of star formation tracers (far-UV and 24 μm images) must be located in the interarm region, showing that interarm star formation is significant even in grand-design spirals.

We examined the star formation efficiency based on H_2 in the arm and interarm areas. We confirmed the results of L08 that this quantity is constant on average and any enhancement in

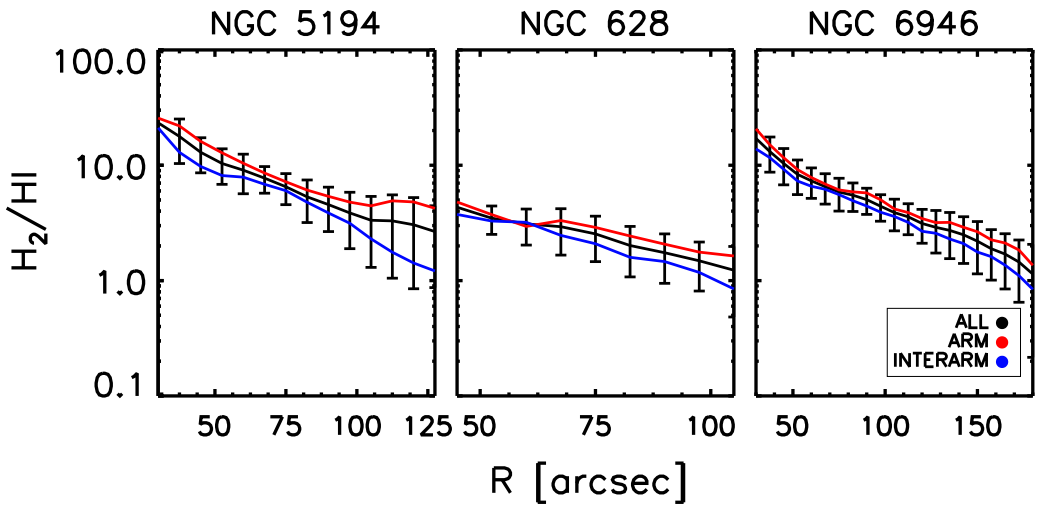

Figure 3.8: Mean fraction of molecular gas (H_2/HI) in radial annuli for all pixels and their scatter (black) and arm (red) and interarm (blue) regions. We find that any enhancement in the arm region is less than a factor of two.

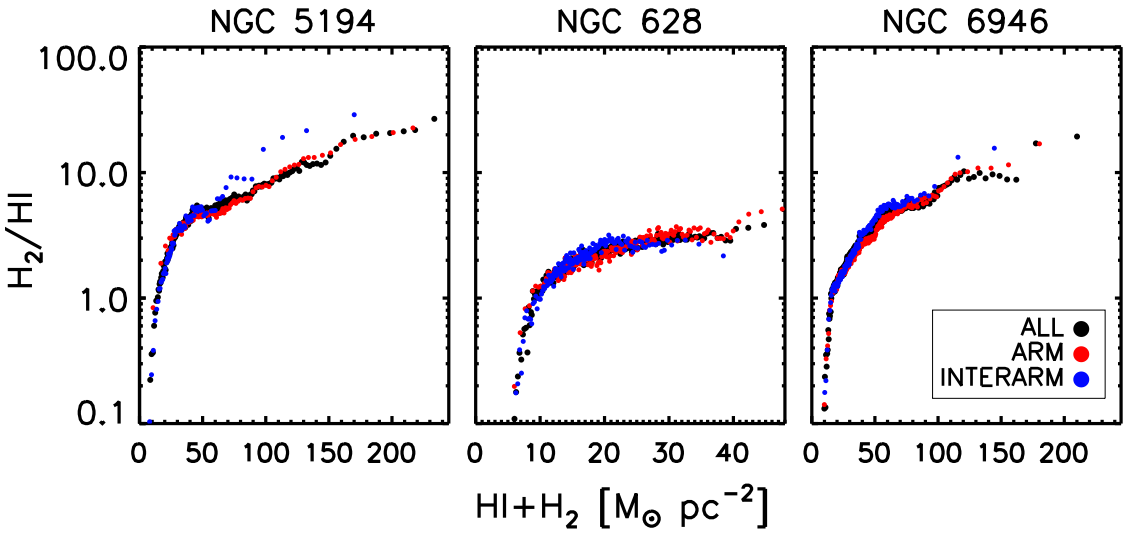

Figure 3.9: Molecular gas (H_2/HI) as a function of the total gas surface density for all pixels (black) and arm (red) and interarm (blue) regions. In all three cases, there is no enhancement of the molecular gas fraction in the arms versus the interarm regions in terms of the total gas suface density.

the arm areas is less than 10% for the grand-design spirals, NGC 628 and NGC 5194. The flocculent spiral, NGC 6946, does show an enhancement of the SFE in the arm region, but this may be caused by an underlying weak spiral density wave, which has caused our spiral definition to be associated with isolated regions of high SFR.

We then explored whether the arms were triggering the formation of molecular gas by comparing the fraction of molecular gas in the arm and interarm regions. The arms showed a higher molecular gas fraction, but this was found to be due to higher gas surface densities in the arms.

Taken together these results show that interarm star formation is significant and that the spiral arms gather the gas into regions of higher surface densities, which leads to an enhanced molecular fraction, but they do not "shock trigger" star formation nor molecular gas formation. Thus, spiral arms act only to reorganize the material in the disk out of which stars form.

Chapter 4

Testing Spiral Structure Theories

Abstract

*We look for evidence for a long-lived, quasi-stationary spiral structure that is shock triggering molecular gas and star formation in disk galaxies, based on density wave theory. This model predicts angular offsets between star formation tracers, due to the onset time of star formation and the pattern speed of the spiral structure, as well as the dispersion of the star formation tracers downstream from the spiral arms. Using 12 spiral galaxies with high resolution maps of the far-ultraviolet (GALEX NGS) and 24μm emission (*Spitzer *SINGS) and cold gas — CO (HERACLES) and HI (THINGS) we algorithmically measure angular offsets between these tracers via the cross-correlation of the images in the way proposed by Tamburro et al. (2008) and we examine the azimuthal profiles of the tracers for evidence of their dispersion downstream from the arms. Despite using the highest resolution maps to date, we could find no systematic ordering of angular offsets or the dispersion of star formation tracers downstream from the arms. This raises serious questions for the simplest version of this model. These findings point to either a spiral structure that reorganizes the ISM rather than directly triggering star formation or one that is more complex than a long-lived structure with a constant pattern speed.*

4.1 Introduction

In §1.4 we reviewed the dominate theories of spiral structure and discussed how proving or falsifying these theories is difficult. Like many problems in astrophysics, no single observation can truly falsify a theory because, not only do observations have many uncertainties, but theories can always be further complexified. Thus, we must resort to using observations to limit the probability of a given theory and in so doing increase the probability of others (*e.g.* Hogg 2009).

In Chapter 3, we examined star formation in both the arm and interarm regions of spiral galaxies and found little evidence supporting an enhancement of the star formation efficiency that would be associated with shock triggering of star formation in the arms. In this chapter, we dig deeper into the most widely supported theory of spiral structure namely that it is a

long-lived, stable phenomenon, which is actively participating in star formation through shock triggering. We specifically look for evidence that spiral arms are long-lived with a constant pattern speed and that they are shock triggering star formation. We investigate two important predictions of this model, namely that star formation tracers should exhibit angular offsets due to the onset time of star formation and the constant pattern speed of the spiral structure and that the tracers should show dispersion downstream from the arms. We first review in greater detail the assumptions and predictions of this theory as well as subsequent studies, both observational and computational, that have provided evidence for or against it. We then use a simple toy model of a disk galaxy to examine these two predictions and how they should manifest themselves in observations. In the subsequent sections of this chapter, we conduct a series of observational tests to draw inferences on the plausibility of this model.

4.1.1 Long-Lived Spiral Arms & Shock Triggered Star Formation

Roberts (1969, hereafter R69) and Fujimoto (1968) developed a large-scale shock scenario for star formation in spiral arms based on the density wave theory of Lindblad (1960) and Lin & Shu (1964, 1966). It relies on the assumption of a large scale, bisymmetric, spiral structure that is rigidly rotating in a quasi-stationary state. The spiral pattern is seen to orbit at a constant global pattern speed which results from excitations of global modes. Inside corotation the disk moves faster than the pattern such that the gas and stars drift through it (the opposite is true beyond corotation). If the relative velocity between the density wave and the ISM is supersonic, the gas can respond in a non-linear fashion and a shock can form on the inside edge of the trailing spiral arm. The shock compresses the HI gas, leading to the formation of molecular gas and subsequently star formation. In this way, observed spiral arms are produced by the continual triggering of star formation through compression in the gas peak (Lubow et al. 1986).

The theory of a long-lived, quasi-stationary spiral structure that is shock triggering star formation makes several predictions that can be used as tests for both simulations and observations. As originally explained by R69, angular offsets of the young stars from the HI and molecular gas and age gradients in the stars across the arms should be expected. Roberts et al. (1975) found evidence for such offsets and posited that the shock strength and spiral strength could account for the ordering of spiral disks into Hubble type and luminosity class. As described by Gittins & Clarke (2004), one expects to find at least three spiral patterns. The first is traced by the stellar mass density and the location of the density wave or potential minima. The second spiral pattern is due to the shock and is traced by the dust, which is known to be in locations of compressed gas and the third marks the location of the young stars. Due to the onset time of star formation, each of these arms should lie downstream from the previous one (inside corotation). The left panel of Fig. 4.1 taken from R69 illustrates the positions of the gas shock and young stars inside corotation of a trailing spiral pattern. The relative offset of the spiral patterns depends on the timescales of the stages of star formation and the relative speed between the pattern and the disk. This theory, therefore, also predicts colour and stellar age gradients across

the arms. Within corotation, the disk travels faster than the pattern so when stars form in the arms, they gradually drift away as they age producing colour gradients. Beyond corotation the gradient will be in the opposite direction. In a similar fashion one also expects an asymmetry of star formation tracers across the arms. Within corotation the steeper side should be on the concave side of the arm. The direction of the color gradients, the skewness of the star formation tracers and the change in the sign of the angular offsets can be used to locate corotation (Gittins & Clarke 2004).

However, typically these predictions have been based on studies which have used a number of simplifying assumptions. Many, including R69, have used one-dimension simulations and the assumption of an isothermal gas (*e.g.* Woodward 1975; Lubow et al. 1986; Wada & Koda 2004). However, this picture has also been updated to include a stratified ISM and two and three dimensions (*e.g.* Levinsion & Roberts 1981; Balbus 1988; Dobbs & Bonnell 2007; Kim et al. 2008; Kim et al. 2010). The main difference with these models is that the shock regions tend to be more ragged in definition, the spiral arms tend to be broader and molecular gas can also be found in the interarm regions. Clearly, this more ragged definition will make it more challenging to observationally measure the predictions we have outlined.

Recently Dobbs & Pringle (2010) have looked in detail at the distribution of cluster ages across spiral arms in realistic simulations. In their sample they included a galaxy with a fixed spiral potential which mimics a long-lived spiral with a constant pattern speed. The right panel of Fig. 4.1 shows the cluster age distribution in this galaxy. If one compares this to the illustration of R69 (left panel) one sees that the distribution is more complex. However, the clusters are still ordered in the way expected. Other simulations using rigid spiral potentials have also demonstrated predictions of this model including angular offsets between the spiral potential and the gas and stars. The distribution of the giant molecular clouds (GMCs) have also shown a sharp edge on the upstream side of the arms where fresh material is flowing in and a dispersed, smooth downstream side (Dobbs et al. 2006).

However, rigid potentials are not realistic and as soon as this assumption is relaxed and an active spiral potential that is allowed to change over time is used, the offsets and skewness are no longer seen. Dobbs & Bonnell (2008) used an active galactic potential and have shown that no offsets should be found between the stars and gas with respect to the spiral potential minima. Gas accumulates in the potential minima of the forming spiral as it develops and thus the young stars and gas are coincident. Using an active galactic potential means that the original assumptions of the theory are put into question. As we have seen in §1.4 such simulations are notorious for having rapidly dissipating spiral structures and indeed the simulations of Dobbs & Bonnell (2008) produced a spiral structure that was changing over time and had no fixed pattern speed or corotation radius. Thus, either we lack the resolution or the necessary physics to properly simulate a long-lived structure or one needs to turn to a transient spiral structure model. It is necessary then to turn to observations in order to find evidence for these predictions. In this present work we focus primarily on the predictions of angular offsets and skewness of

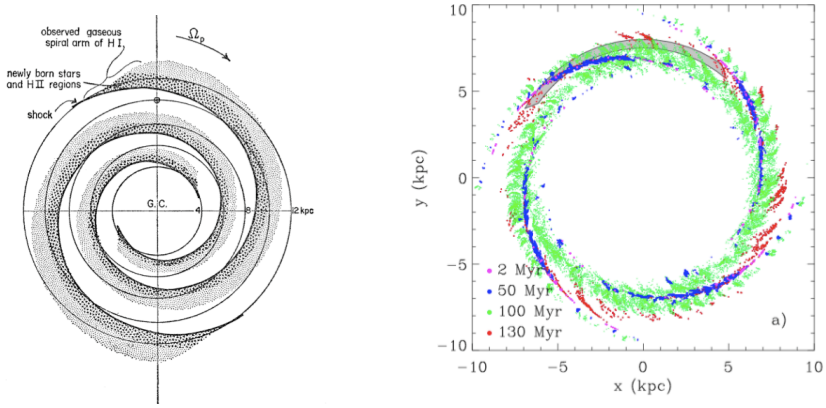

Figure 4.1: Illustration of the relative location of gas shock, sharp HI peak and newly formed stars in HII regions in the gaseous spiral arms of a trailing spiral pattern (left) (Figure 7 of R69). Distribution of stellar cluster ages in the spiral arms of a long-lived spiral potential with a constant pattern speed (right) (Figure 2 of Dobbs & Pringle (2010)).

the star formation tracers in the arms. We now examine the evidence found so far for these predictions in observations.

The few studies that have examined the skewness of star formation tracers near spiral arms have provided unconvincing results. Schweizer (1976) examined azimuthal profiles in optical bands and found no convincing evidence for an asymmetry in spiral arms. Del Rio & Cepa (1998) used an algorithmic method to measure skewness and in so doing established a front that changes from one side to the other in the arms which one could use to identify corotation.

A number of observational studies have looked for qualitative evidence for angular offsets of star formation tracers. Early observations showed dust lanes on the inside part of the arms with respect to HII regions (*e.g.* Lynds 1970). The first study which showed more detailed observational support for this picture was Mathewson et al. (1972) who conducted a radio survey of M51 and found that radio arms were on the inside edge of the optical arms in line with dust lanes, corroborating gas compression in arms. Rots (1975) found similar results in a radio study of M81. A detailed study of M33 by Humphreys & Sandage (1980), however, presented a more complex picture. While two of the arms did show dust lanes on the inner edge of the arm and bright young stars on the outer part of the arm, the third arm showed no such features or ordering.

Ideally one would like to examine offsets between the gas and young stars. Due to the lack of HI in the inner part of the disk and the fact that the molecular gas forms GMCs out of which stars form, it is natural to look for offsets between CO and Hα or 24μm emission. A number of studies have looked for such offsets and examined the streaming motions near the arms, especially in M51 and M81 (*e.g.* Vogel et al. 1988; Rand & Kulkarini 1990; Lord & Young 1990; Garcia-Burillo et al. 1993; Rand 1995; Loinard et al. 1996; Shetty et al. 2007; Egusa et al. 2009). However, all such studies used by-eye determinations of these offsets by selecting individual patches of a single arm. Such methods can easily introduce potential biases.

Recently Tamburro et al. (2008, hereafter T08) developed an algorithmic technique to measure offsets between star formation tracers and in so doing also measured the timescale of going from HI atomic gas to dust-enshrouded massive stars (as traced by 24μm emission). They measured angular offsets by locating the peak of the cross-correlation function between HI and 24μm emission in radial annuli for 14 disk galaxies. They then modeled the angular offsets and fit the pattern speed, Ω_p, and the timescale, $t_{HI\rightarrow 24\mu m}$, assuming that both of these were constant. Their findings were in agreement with the simple prescription of R69. They found corotation radii at $\sim$2.7r$_{exp}$, which is consistent with other works (*e.g.* Kranz et al. 2003) and short timescales of 1-4 Myr. Indeed the angular offsets were found to be very small (5°) between the tracers. T08 also used BIMA SONG CO maps (Helfer et al. 2003) to measure angular offsets between the molecular gas and 24μm. The low resolution of these images, however, provided too few points to make accurate estimates of the timescale and they were only able to conclude that the CO offsets were less than that of HI in comparison to the 24μm emission, which supports the evolutionary progression. T08's work is the first to approach offset measurements using an algorithmic method as opposed to by-eye determinations and they used the highest resolution images to date. Since we will be employing the method developed by T08, we now describe it in greater detail.

4.1.2 Method of Tamburro et al. 2008

Angular offsets between HI and 24μm emission allow one to measure the timescale between gas compression and massive star formation because peaks of HI formation are known to be the sites of forming molecular clouds and the 24μm emission traces the young dust enshrouded stars. The time between these two events, $t_{HI\rightarrow 24\mu m}$, the local circular velocity, $v_c(r)$, and a pattern speed, Ω_p, for the spiral arms, lead to an angular offset between these two tracers of:

$$\Delta\phi(r) = (\Omega(r) - \Omega_p)t_{HI\rightarrow 24\mu m}. \tag{4.1}$$

The angular offset varies with radius. When the disk rotates faster than the pattern (inside corotation) we expect $\Delta\phi > 0$ and when the pattern rotates faster than the disk (beyond corotation) we expect $\Delta\phi < 0$. At corotation $\Omega(R_{cor}) = \Omega_p$, the sign changes and $\Delta\phi = 0$.

In order to measure $\Delta\phi$, T08 divided the images into radial annuli and cross-correlated them to find the relative offset with the best match. The best match between the two images is found by minimizing the following quantity as a function of the shift, l (lag):

$$\chi^2_{x,y}(l) = \Sigma_k[x_k - y_{k-l}]^2. \tag{4.2}$$

The sum is carried out over all elements N of x and y, where these each represent one of the two tracers at a given radius as a function of azimuth, ϕ, such that:

$$x_k = f_{HI}(\phi_k|\hat{r}) \text{ and } y_{k-l} = f_{24\mu m}(\phi_{k-l}|\hat{r}). \tag{4.3}$$

By minimizing χ^2 one maximizes the following quantity:

$$cc_{x,y}(l) = \Sigma_k[x_k \times y_{k-l}], \tag{4.4}$$

defined as the cross-correlation coefficient. T08 used the normalized version such that:

$$cc_{x,y}(l) = \frac{\Sigma_k[(x_k - \bar{x})(y_{k-l} - \bar{y})]}{\sqrt{\Sigma_k(x_k - \bar{x})^2 \Sigma_k(y_k - \bar{y})^2}}, \tag{4.5}$$

where $\bar{x}$ and $\bar{y}$ are the means of x and y respectively. In this way, perfectly identical patterns have a cross-correlation coefficient of unity and highly dissimilar patterns have a value much less than one. At each annulus, T08 searched for a local maximum of the $cc(l)$ around $l \simeq 0$. The location of the maximum, l_{max}, defines the angular offset between the two tracers such that $\Delta\phi(r) = -l_{max}(r)$.

With the angular offset, $\Delta\phi(r)$, and the rotation curve, $v_c(r)$, one can write Eq. 4.1 as:

$$\Delta\phi(r) = \left(\frac{v_c(r)}{r} - \Omega_p\right) t_{HI \to 24\mu m}. \tag{4.6}$$

T08 used χ^2 fitting of the above with the measured angular offsets and derived best fits for $t_{HI \to 24\mu m}$ and Ω_p. This method can be used for any two tracers and we shall use this method to repeat the work of T08 and also determine the angular offsets between 24μm and CO, which traces H_2 gas. We also look for offsets between the SFR, defined as a combination between UV and 24μm (see Chapter 3), and CO and the SFR and 3.6μm images, which trace the old stellar population.

4.1.3 Toy Model

Eq. 4.6 allows us to measure angular offsets between tracers based on the onset time between the tracers, the rotation curve of the galaxy and the position of corotation of the pattern. Such angular offsets and the dispersion of the tracers downstream of the arm pattern within corotation are the two predictions of the R69 model that we seek to investigate. Before turning directly to observations, we first examine how these predictions manifest themselves in a simple toy model of a spiral galaxy.

We assume the model galaxy has a flat rotation curve (see upper left panel of Fig. 4.2) and a two-arm spiral pattern with a corotation radius of 2.7R_{exp} (*i.e.* Kranz et al. 2003). We consider two star formation tracers with an onset time of 3 Myr, which is in the range found by T08. The upper right panel of Fig. 4.2 shows the radial profile of the angular offsets calculated from Eq. 4.6. In the inner regions large positive offsets are expected and beyond corotation the offsets become negative. The lower panels show the position of the tracers in the spiral arms in polar (left) and cartesian (right) coordinates. The variation in the angular offsets of the tracers with radius, produces a spiral pattern that is effectively more tightly wound. The offsets are

small except in the very inner regions and thus the arm patterns of the two tracers will likely overlap, depending on the amount of dispersion and width of the tracers. This could make by-eye determinations of offsets challenging.

We also examine the azimuthal profiles of the tracers. We saw in Chapter 3 that a substantial fraction of star formation tracer emission was also found in the interarm regions (at least 30%) and thus we include this interarm star formation. Half of all star formation tracer emission is produced in the arms, which are given a width of 15°, and the rest is considered to be stochastic throughout a fiducial annulus. The emission has a decay time which is expressed in terms of the orbital time (1/10th (dashed) and 1/5th (solid) in this case). Such tracers mimic 24μm and UV emission, which have decay times of roughly 40 and 80 Myr respectively. The model galaxy rotates towards positive angular values as does the spiral pattern. We see that for both relative decay times, the angular profile of the star formation tracers is clearly skewed downstream of the arms (lower panel of Fig. 4.3) and has a much sharper upstream side.

In the upper panel of Fig. 4.3 we show the autocorrelation functions of each tracer (dashed and solid). The autocorrelation functions are calculated as in Eq. 4.5, but both x and y represent the same tracer. Because x and y are then identical, we expect the autocorrelation function to be centered at zero and with a maxima of unity, which by definition is the case for identical patterns. Indeed, this is the case. We also note, that unlike the profiles of the tracers, the autocorrelation functions are not skewed and are perfectly symmetrical, which means that such functions cannot be used to detect the dispersion of the tracers.

We also examine the cross-correlation function of the two tracers (dotted curve in the upper panel of Fig. 4.3). Here the patterns, while coincident, are not identical and thus the maxima is less than unity. We also see that the function is skewed in the direction of the dispersion. Interestingly, the maxima is not perfectly centered at zero despite the fact that the two tracers are coincident (see vertical dotted line). This may be due to the skewness and the width of the arms. The effect is small, but since the offsets are likely to be less than 5°, it could introduce uncertainties.

The toy model has shown us that the angular offsets are small and that dispersion of the tracers can complicate locating the peak of the cross-correlation function. We have also seen that detecting the dispersion of the tracers can only be done directly from the azimuthal profiles of the tracers themselves and not from the autocorrelation function, which remains symmetrical.

Having described in detail the model of spiral structure that posits a long-lived pattern shock triggering star formation, we now turn to a series of observational tests to examine the predictions of angular offsets between star formation tracers and the skewness of these tracers in the arms. We use high-resolution images of HI, CO, 24μm and UV for a sample of 12 galaxies. We first examine whether there are angular offsets between star formation tracers ordered in a regular way in accordance with a constant spiral pattern speed and star formation timescale. We then examine whether there is evidence for downstream dispersion of these tracers as one would expect in the case of shock triggered star formation by a rotating pattern. In order to do so, we

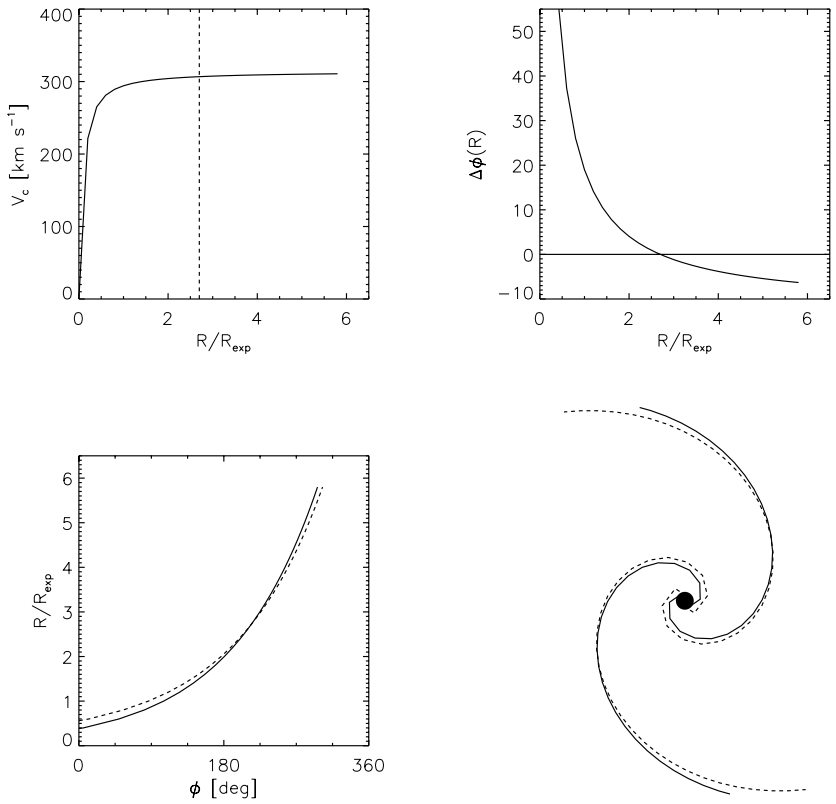

Figure 4.2: Toy model properties showing the relative position of two star formation tracers with an onset time of 3 Myr. The rotation curve of the galaxy modeled with an arctan function (upper left) and corotation of the spiral pattern is at 2.7R$_{exp}$ (dashed line). With a t$_{SF}$ of 3 Myr, Eq. 4.6 determines the radial profile of the angular offsets between the two tracers (upper right). The relative positions of the spiral patterns of each tracer are shown in polar (lower right) and cartesian coordinates (lower left).

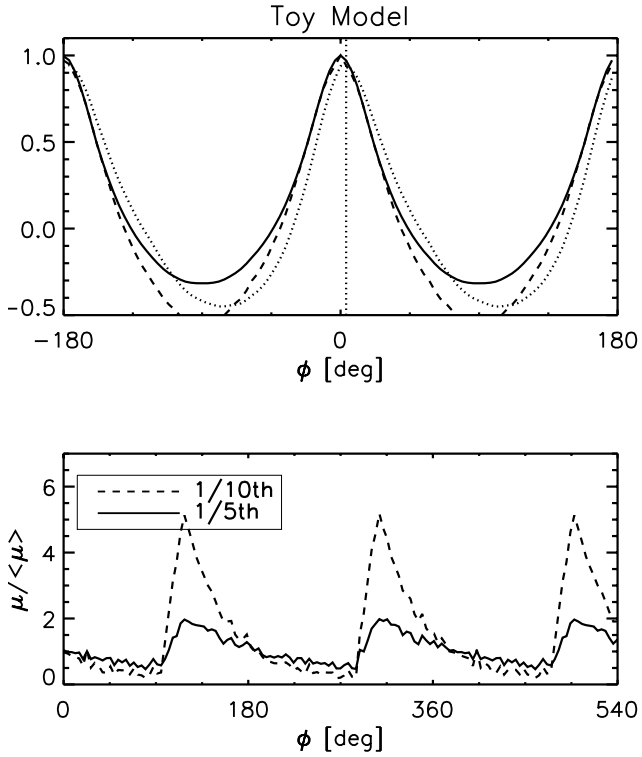

Figure 4.3: Model of the azimuthal profile of two star formation tracers in a galaxy where half of the star formation emission, μ, is produced in two spiral arms, 180° apart (bottom). The tracers each have a decay time which is a fraction of the orbital time (*i.e.*, 1/5th of the orbital time (solid) and 1/10th of the orbital time (dashed)). The model galaxy rotates toward increasing angles (right). In both cases the tracers are skewed in the direction downwind of the arms. The auto correlation function is shown for each tracer (*i.e.*, 1/5th of the orbital time (solid) and 1/10th of the orbital time (dashed)) as well as the cross-correlation function of the two tracers together (dotted) (top panel). The autocorrelation functions are symmetrical and have a maxima of unity, centered at zero, as one would expect. The cross-correlation function of the two tracers is skewed downstream and does not have a maximum precisely at zero as shown by the dotted line.

repeat the study T08 and also include CO maps from HERACLES (Leroy et al. 2009) in order to probe the timescales between molecular gas and 24μm emission with higher resolution. In §4.2 we describe our sample and how the images are processed. In §4.3 we compare our results to those of T08 by looking at the offsets between 24μm emission and HI. We also examine an alternative approach using the 2D cross-correlation function in order to model the corotation radius and timescales in §4.4. In §4.5 we measure offsets between other star formation traces including H_2 as traced by CO and 24μm and 3.6μm images and the SFR as inferred from 24μm and Far-UV emission. In §4.6 we use two grand-design spirals from our sample (NGC 5194 and NGC 628) to look for evidence of skewness of these tracers as one would expect in the advent of a shock front and in §4.7 we summarize our conclusions.

4.2 Analysis

We chose 12 galaxies in common with the sample of T08 that have coverage in THINGS (Walter et al. 2008) and SINGS (Kennicutt et al. 2003). Eight of these galaxies also have coverage in HERACLES (Leroy et al. 2009). For some galaxies, GALEX (NUV+FUV) (Gil de Paz et al. 2007) images were also used to define the SFR with the 24μm images as described in Chapter 3. We also use 3.6μm images (IRAC) to trace underlying old stellar mass density.

The galaxies were deprojected according to the values of T08, with the exception of NGC 2841, NGC 3521 and NGC 5194, which were found to have different parameters (see Table 4.1). Fig. 4.4 shows deprojected 3.6μm images for our sample as well as the direction of rotation, which is defined by assuming a trailing spiral pattern.

The images were aligned to the THINGS astrometric grid and were degraded to a common resolution of either 6″ for our analysis of HI and 24μm images or 13″ for our analysis of CO and 24μm images. Chapter 3 describes in detail the processing of the HI, 24μm, UV, CO and 3.6μm images. Using the method described in §4.1.2, we cross-correlated the images and located the peak of the cross-correlation function, corresponding to the angular offset between the tracers.

4.2.1 2D Cross-Correlation

An alternative method to that presented in T08 (see §4.1.2) is to search through the parameter space of $t_{HI\rightarrow 24\mu m}$ and R_{cor} and find the combination that provides a set of $\Delta\phi(r)$ giving the maximum 2D cross-correlation. In order to do so, we first require a model of the rotation curve. While one could use kinematical measurements, we use a simple model approximation. As in Chapter 2, we can model the rotation curves using an $\arctan$ function such that:

$$V_{rot}(R) = \frac{2}{\pi} V_{max} \arctan(\frac{R}{0.1 r_{exp}}) \tag{4.7}$$

(Courteau, 1997), where V_{max}, the maximum rotation curve value and r_{exp}, the disk scale

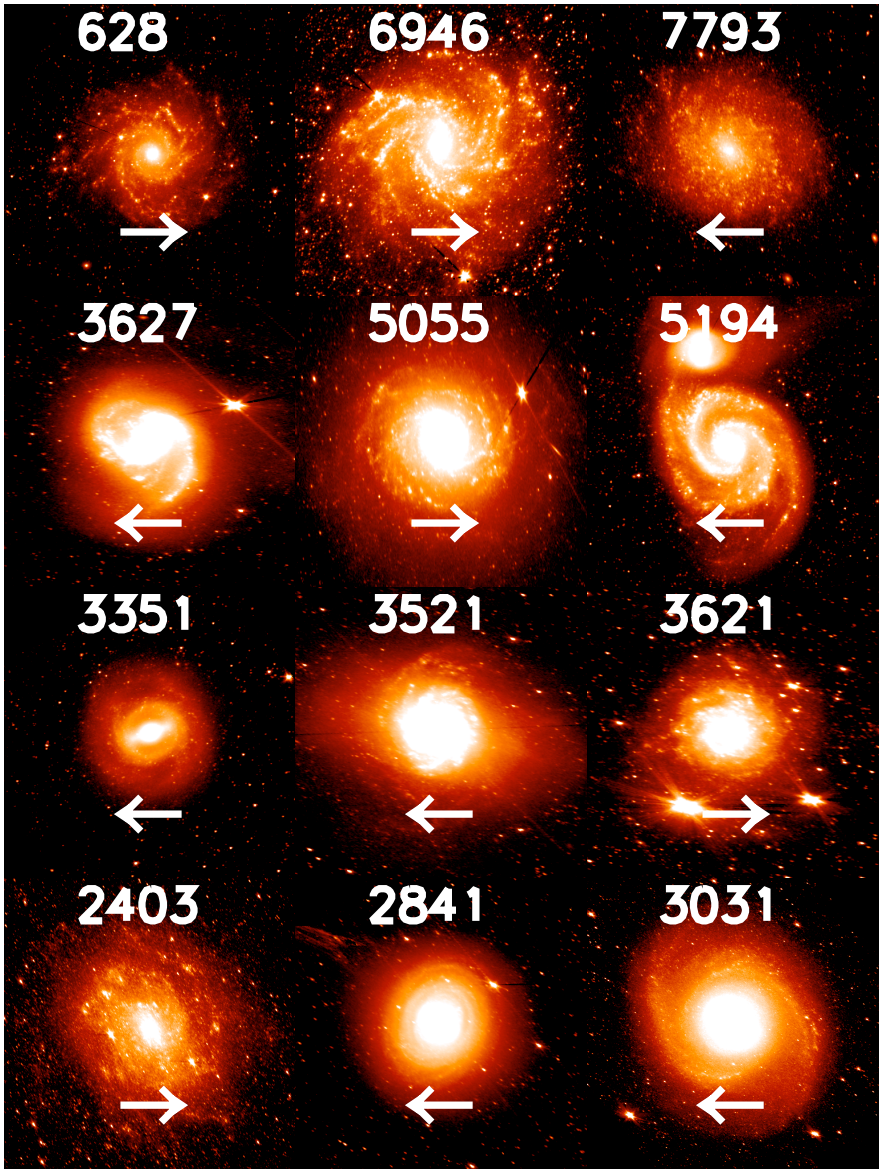

Figure 4.4: Sample of 12 galaxies. We show the deprojected 3.6μm images with arrows denoting the direction of rotation based on the assumption of a trailing spiral pattern.

Table 4.1: Sample Properties: The inclination and position angles used to deproject the galaxies, their adopted distance, scale length and maximum amplitude of their rotation velocity. With the exception of NGC 2841, NGC 3521 and NGC 5194, all values are those from T08.

Name	inc	PA	D	r_{exp}	V_{max}
	[°]	[°]	[Mpc]	$''$	[km s^{-1}]
NGC 2403	63	124	3.22	1.3	128
NGC 2841	63	148	14.1	0.92	331
NGC 3031	59	330	3.63	3.62	256
NGC 3521	65	162	10.05	0.74	242
NGC 3621	65	345	6.64	0.8	144
NGC 3627	62	173	9.25	0.95	204
NGC 5055	59	102	7.82	1.16	209
NGC 5194	20	172	7.77	1.39	242
NGC 628	7	20	7.3	1.1	220
NGC 6946	32.6	242	5.5	1.73	201
NGC 7793	50	290	3.82	1.16	109

length, are the values in T08.

A pair of $t_{HI\rightarrow 24\mu m}$ and R_{cor} provides a series of $\Delta\phi(r)$ at radial positions, r, as:

$$\Delta\phi(r) = \left(\frac{V_{rot}(r)}{r} - \frac{V_{rot}(R_{cor})}{R_{cor}} \right) \times t_{HI\rightarrow 24\mu m}. \tag{4.8}$$

The $\Delta\phi(r)$ values can be easily translated into $l_{max}(r)$. We then calculate the following 2D cross-correlation coefficient as:

$$cc_{x,y}(r,k) = \Sigma_r \Sigma_k [x_{r,k} \times y_{r,k-l_{max}(r)}], \tag{4.9}$$

where r is summed over the radii considered. Similarly, the normalized 2D cross-correlation is given by:

$$cc_{x,y}(r,k) = \frac{\Sigma_r \Sigma_k [(x_{r,k} - \bar{x_r})(y_{r,k-l} - \bar{y_r})]}{\sqrt{\Sigma_r \Sigma_k (x_{r,k} - \bar{x_r})^2 \Sigma_r \Sigma_k (y_{r,k} - \bar{y_r})^2}}, \tag{4.10}$$

where $\bar{x_r}$ and $\bar{y_r}$ are the means of x and y at the given annulus r. By finding the maximum $cc_{x,y}$ and then gradually refining the parameters of $t_{HI\rightarrow 24\mu m}$ and R_{cor} in smaller increments, one can find the combination that best matches the data. We employ this method in §4.4 using HI and 24μm images.

4.3 Comparison with Tamburro et al. 2008

We use the 12 galaxies in our sample to investigate possible angular offsets between HI and 24μm emission and compare our results to T08. After initial processing, the images are translated from rectangular to polar coordinates, (r, ϕ), and divided into annuli of 5$''$ width. Fig. 4.5

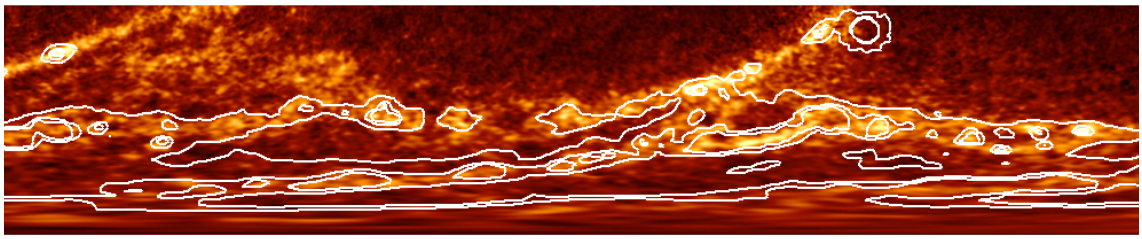

Figure 4.5: HI Emission of NGC 5194 in polar coordinates with contours of the 24μm emission overlaid. Any angular offsets are small between the arm patterns of these two tracers.

shows the HI emission in polar coordinates for NGC 5194 with the contours of 24μm emission overlaid. One notes that the arm patterns of these tracers, which cross the image diagonally from the lower left to the upper right, are nearly coincident. Thus, any offsets between these tracers must be small.

The cross-correlation coefficients were calculated for angular offsets from -180° to +180° in increments of $\sim 0.1°$. We restrict the search for the peak between $\pm 30°$, because the offsets must be at least this small (see Fig. 4.5) . We fit the region of the maxima with a four degree polynomial as T08 and calculate its peak value. The angular position of the peak is the chosen angular offset, $\Delta\phi(r)$, between the tracers at each radius. Any local maxima with a cross-correlation coefficient less than 0.3 is rejected. The sign of the angular offsets is corrected for the direction of rotation of the galaxy. One expects to find positive angular offsets smoothly decreasing with radius and crossing zero at corotation.

Fig. 4.6 shows the angular offsets (black points) versus radius for all twelve galaxies. The colors reflect the value of the cross-correlation with low values (≈ 0.3) being blue and high values (≈ 0.8) being red in the neighborhood of the chosen offset corresponding to the peak value ($\pm 20°$). We see that around the peak value, there is a broad region where the $cc(l)$ is high.

The radial profiles of the angular offsets do not show any smooth trend of going from positive to negative values and show considerable scatter. Comparing these profiles to that of the toy model in Fig. 4.2, we see that these profiles do not correspond in any way to the model predictions. Our profiles also do not agree with the profiles found by T08, who found offsets that agreed with the picture of shock triggering of star formation in spirals arms with a constant pattern speed. We investigated the cause of this in greater detail. Fig. 4.7 and 4.8 shows the cross-correlation coefficient functions at several radial annuli for NGC 5194 and NGC 3627. The left panels show the full range from -180° to +180°. We also zoom in on the peak of the function in the boxed regions and display these on the right. The zoomed regions reflect the range of -30° to +30°. The red curve shows the fourth degree polynomial fit.

The top panel of Fig. 4.7 exhibits what one would hope to find when seeking the maximum of $cc(l)$. At this radius a single, narrow peak is found. The other panels and those of Fig. 4.8, show, however, that at most radii, the $cc(l)$ is more complex, with a very broad peak and uneven

features. The polynomial fit is sensitive to the range over which one fits and selecting this range can be subjective. We tried a number of variations of T08's method, including smoothing and filtering of the images, variations of the cross-correlation calculation and restrictions of narrow regions around the arms and were unable to reproduce the findings of T08.

T08 kindly provided their data for NGC 628 in order for us to do a more careful inspection. While we were able to reproduce some of their offsets, the offsets measured were sensitive to small changes in the polynomial fit and the way in which the cross-correlation function is calculated (*i.e.* use of mean or median for $\bar{x}$ and $\bar{y}$ in Eq. 4.5). Fig. 4.9 shows the offsets found by T08 (black) and two of our attempts using different fitting ranges for the polynomial (blue and red). While T08's offsets show a clear progression from high values to low values, which cross zero, our points are much more scattered. In part, we can attribute this to the fact that T08 selected the peak to fit and chose the range over which they fit by-eye. We also tried to choose specific fitting ranges at each radius, but found the choice to be subjective and we do not know the specific angular range they chose.

Beyond the sensitivity of the peak position to the range of the polynomial fit, resolution may be a cause for the lack of agreement with T08. The angular resolution varies with radius and the thin black line in Fig. 4.9 shows that all of the offsets found by T08 are below the resolution of the image. The common image resolution is $6''$ and at a radius of $30''$ this corresponds to an angle of 11°. Most of the offsets found by T08 were less than 5° except in the very inner regions, where resolution concerns are even greater. However, given that the cross-correlation function is calculated considering all azimuthal positions, it is possible that one can probe below the resolution limit to measure the offsets. The fact that T08's offsets are not randomly scattered points to this possibility. T08 does not address how resolution might affect their results.

It is not clear how resolution might affect the cross-correlation function and the determination of the peak. We first examine how resolution affects the autocorrelation function of two HI maps at a resolution of $6''$ and $13''$ using NGC 5194. The autocorrelation function is calculated like the $cc(l)$ (Eq. 4.5), but in this case both x and y represent the same HI map. For both resolutions, we expect the peak of the autocorrelation function to be centered at zero with a maximum of unity as we saw in the case of the toy model (see Fig. 4.3). Fig. 4.10 shows the autocorrelation function for a series of annuli. Since the azimuthal resolution varies with radius, we list the azimuthal resolution for each pair of images in the upper left of the panels. We see that, as expected, the autocorrelation functions have a peak at zero and maxima of unity. However, one notes that as the resolution size increases, the autocorrelation function broadens and has a higher coefficient over a greater range of angles. We divided each annulus into units smaller than the resolution. Thus, as the resolution size increases, the fraction of pixels with identical values increases. This provides a better agreement in the cross-correlation, which broadens and increases the peak.

In order to examine how the peak position might vary with resolution, we consider the cross-correlation of HI and 24μm at two different resolutions in Fig. 4.11. We use pairs of images

at our common resolution of 6″ (black), and 13″ (blue). Like the autocorrelation function, as the resolution size increases, the $cc(l)$ broadens and has a higher value. The functions are very similar in shape, but as one can see in the zoomed in regions, when the resolution size is large (small radii), the shape of the peak can change substantially. This affects the polynomial fit and ultimately the position of the peak center. In the inner regions, where the resolution effects are greatest, we found that the peak positions varied by as much as 8°. However, at larger radii the difference was less than a degree and the median deviation was 0.5°. Thus, while the peak position remains roughly the same, it is important to consider the uncertainties introduced by resolution in determining its precise position.

In summary, we can attribute our lack of agreement with T08 to one of three possible causes: 1) the offset value is very sensitive to the polynomial fitting of the peak and we do not know the specific angular ranges of the fits used by T08; 2) the offset value is very sensitive to small changes in the way the $cc(l)$ function is calculated; and 3) almost all of the offsets are below the resolution limit of the images and we have found that changes in the resolution of the image do affect the shape of the $cc(l)$ function particularly at small radii.

4.4 Fitting Offsets using the 2D Cross-Correlation

We also tried to find evidence for angular offsets using the 2D cross-correlation as described in §4.2.2. For each galaxy, we modeled the rotation curve using an $\arctan$ function (see Eq. 4.7) and derived a series of angular offset radial profiles for different combinations of the timescale, $t_{HI\rightarrow 24\mu m}$, and the corotation radius, R_{cor} (see Eq. 4.6). Since we know the offsets must be small, we restricted our search to $t_{HI\rightarrow 24\mu m} < 4$ Myr in increments of 0.01 Myr and to $R_{cor} < 4r_{exp}$ in increments of $0.01r_{exp}$. Since we do not wish to assume a particular evolutionary progression, we allow the timescales to be both positive and negative. We correct for the direction of rotation so negative offsets imply that the HI lies ahead of the 24μm emission. For each combination of $t_{HI\rightarrow 24\mu m}$ and R_{cor} we use the angular offsets, $\Delta\phi(r)$, to offset the 24μm emission from the HI at each radial annulus. We then calculate the 2D cross-correlation as in Eq. 4.10.

Fig. 4.12 shows the results of the 2D cross-correlation for two galaxies in the sample, NGC 5194 and NGC 628. We plot the parameter space of the corotation radius in terms of disk scale length versus the timescale. At each combination ($t_{HI\rightarrow 24\mu m}$, R_{cor}/r_{exp}), a colored point reflects the value of the cross-correlation. The red colors show the highest cross-correlation values and the blue colors show the lowest. The contours delineate regions of increasingly high cross-correlation values with thicker lines. The highest cross-correlation coefficient is marked by a red diamond. In both galaxies, the area in the parameter space with the highest cross correlation coefficients is tight around $t_{HI\rightarrow 24\mu m} = 0$. High cross-correlations are found at both positive and negative values of $t_{HI\rightarrow 24\mu m}$, which suggests this may simply be noise as opposed to a genuine offset reflecting an evolutionary progression. Furthermore, even the highest cross-correlation values suggest dissimilar patterns. For all galaxies, the maximum 2D

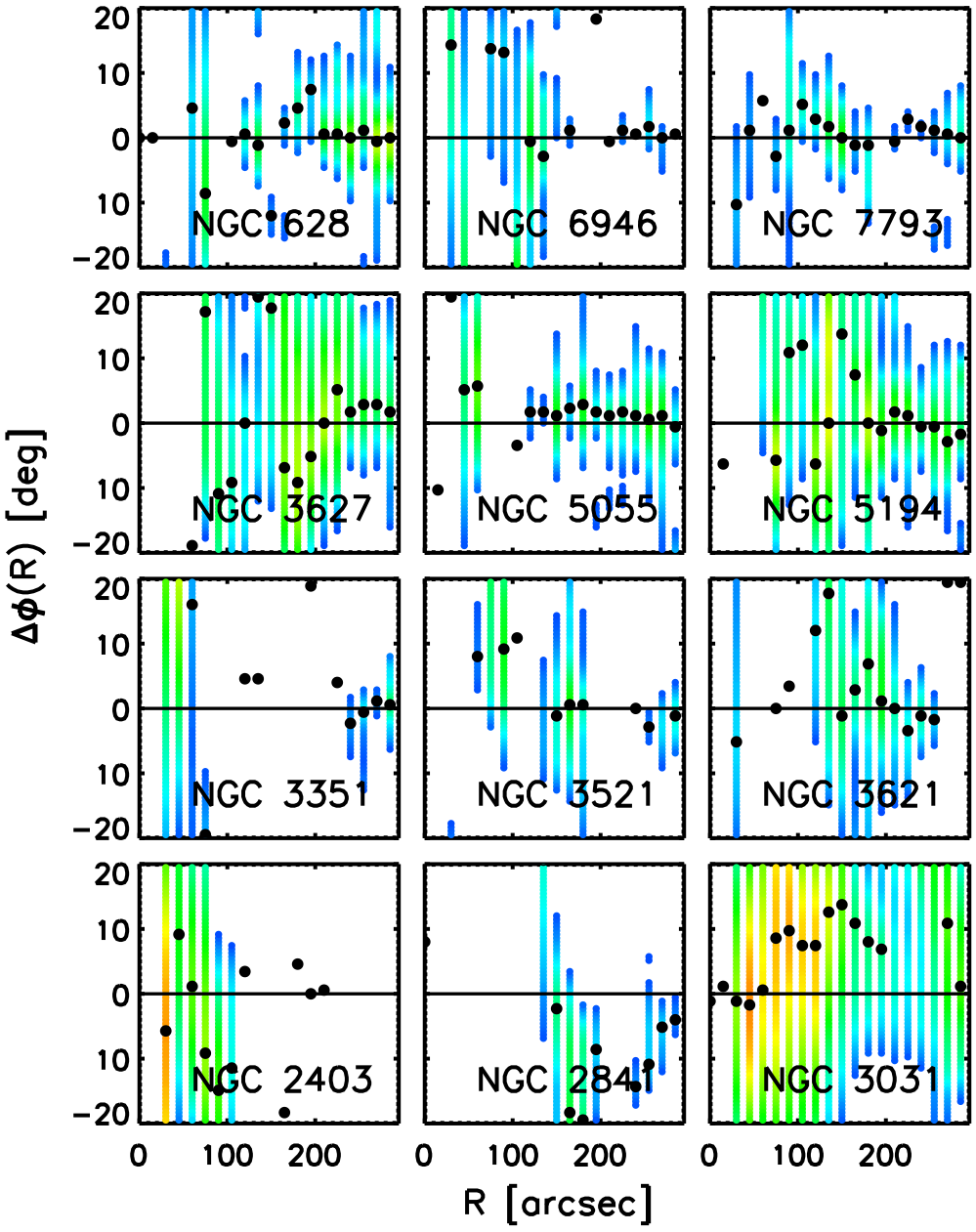

Figure 4.6: Radial profiles of the angular offsets based on the location of the peak of the cross-correlation function between HI and 24μm versus radius (black dots). The colored points reflect the value of the cross-correlation coefficients from high (red) to low (blue) in the range of $\pm 20°$. Values below 0.3, our chosen cutoff, are not shown. The angular offsets are corrected for the direction of rotation.

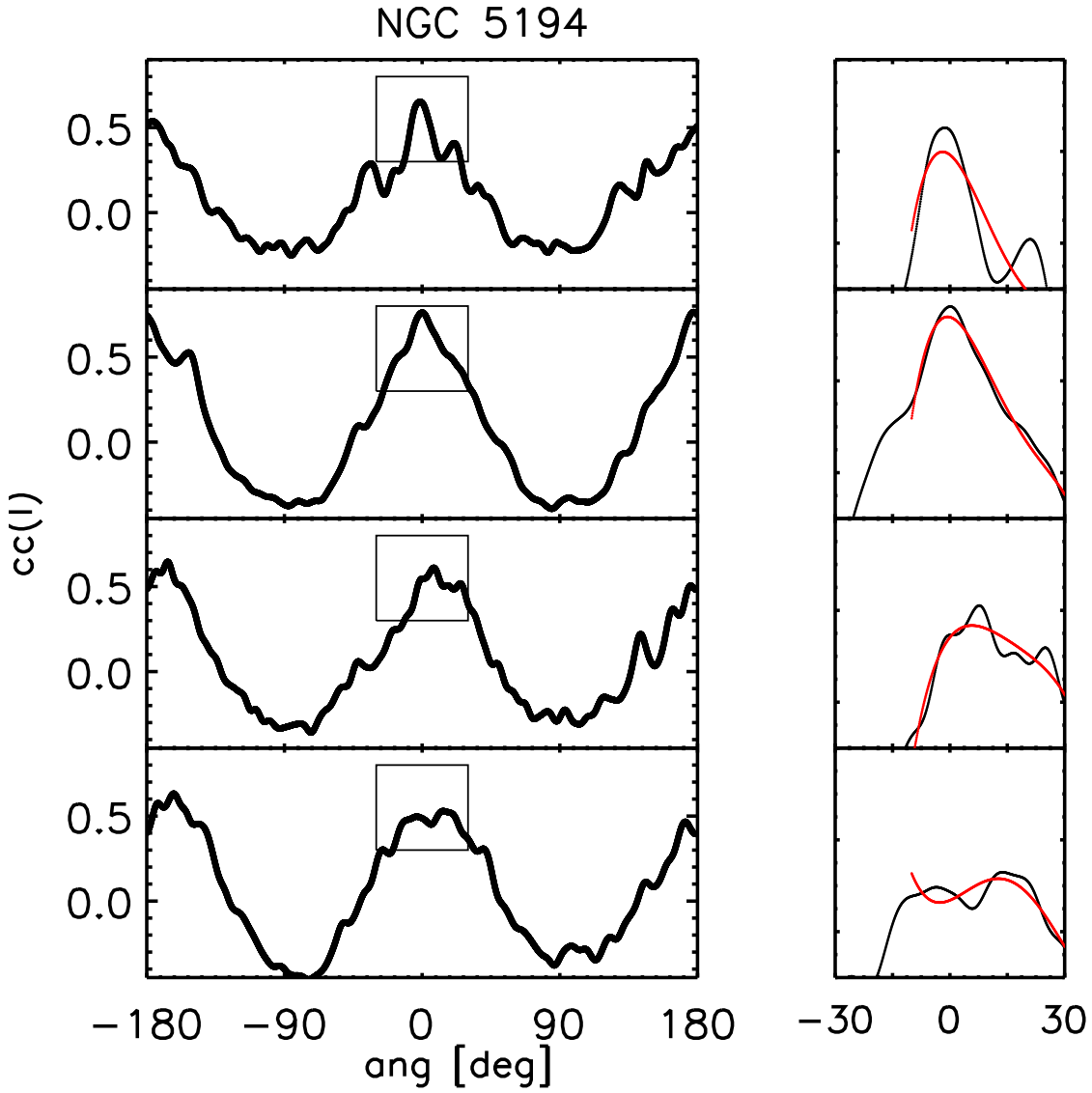

Figure 4.7: Cross-correlation functions $cc(l)$ as a function of azimuth offset for NGC 5194. Each panel represents neighboring annuli from 60″ (bottom) to 80″ (top). The right column shows the boxed region zoomed in ($\pm 30°$). The fourth degree polynomial fits are overlaid in red. The peak is often quite broad and bumpy and the polynomial peak depends heavily on the range of points selected.

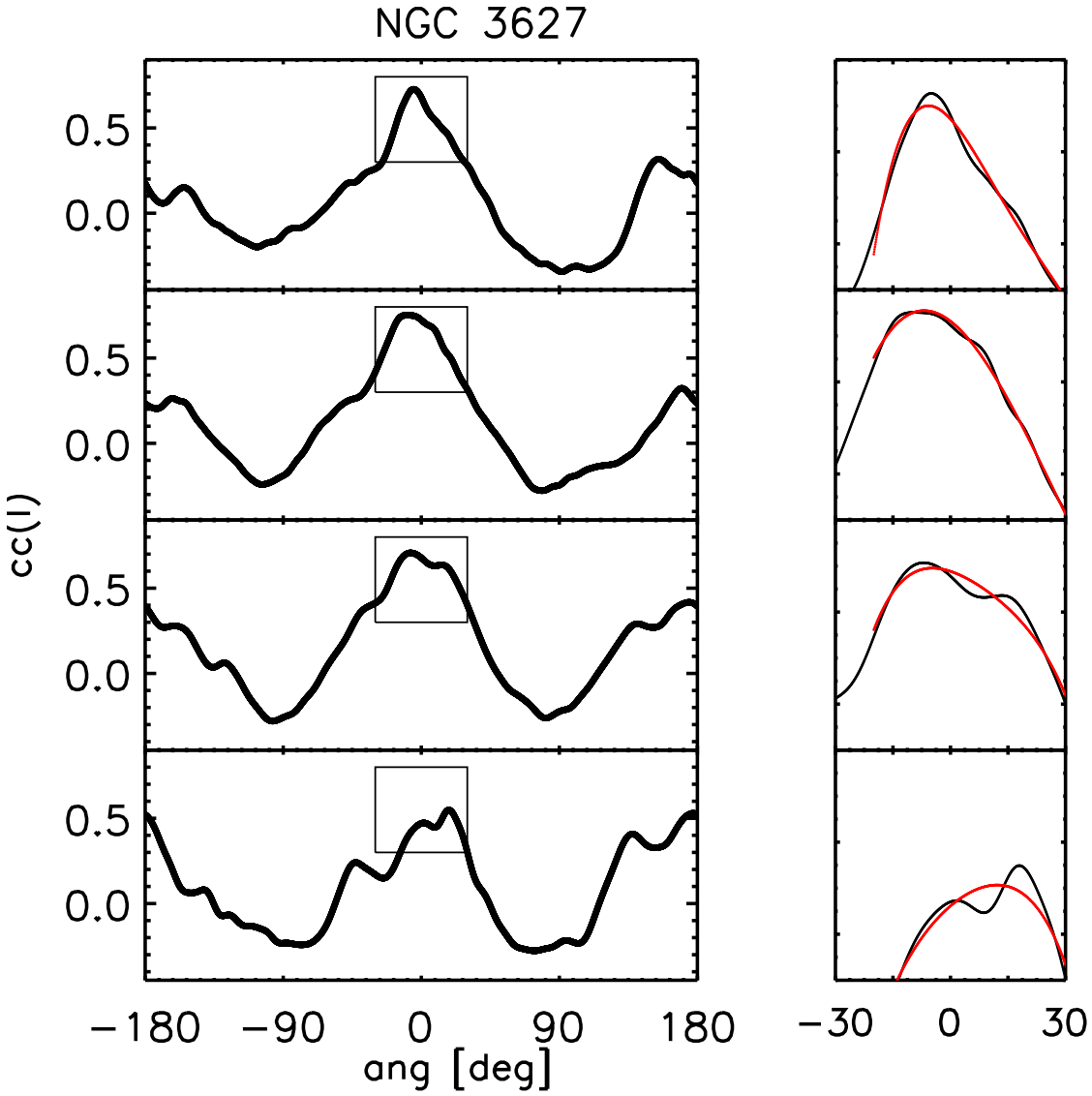

Figure 4.8: Cross-correlation functions $cc(l)$ as a function of azimuth offset for NGC 3627. Each panel represents neighboring annuli from 60″ (bottom) to 80″ (top). The right column shows the boxed region zoomed in ($\pm 30^\circ$). The fourth degree polynomial fits are overlaid in red. The peak is often quite broad and bumpy and the polynomial peak depends heavily on the range of points selected.

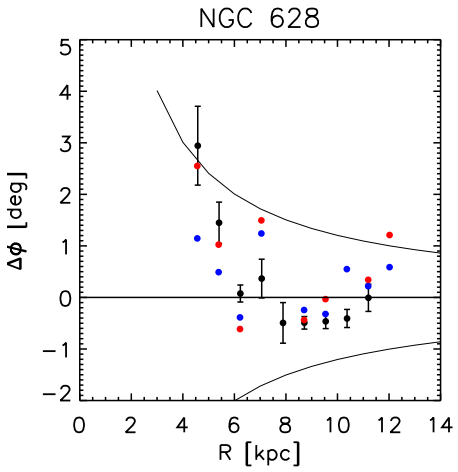

Figure 4.9: Comparison of the offsets found by T08 (black) and the offsets measured in this study using two slightly different fitting ranges of the $cc(l)$ (blue and red). The offsets measured by T08 are all below the angular resolution limit, which varies with radius (thin black line).

cross-correlation coefficient is below 0.3.

Examining the results for NGC 628, we see that the highest cross-correlation value provides at least a reasonable estimate of $t_{HI\rightarrow 24\mu m}$ and R_{cor} (*i.e.* $R_{cor} = 2.8r_{exp}$ and $t_{HI\rightarrow 24\mu m}$=0.4 Myr). However, these results are not equivalent to those found by T08 (*i.e.* $R_{cor} = 1.5r_{exp}$ and $t_{HI\rightarrow 24\mu m}$=3.8 Myr). For NGC 5194, the results are not even plausible (*i.e.* $R_{cor} = 0.2r_{exp}$ and $t_{HI\rightarrow 24\mu m}$=0.1 Myr). The whole sample shows considerable scatter and includes quite unrealistic results. This suggests that angular offsets, if they are present, do not follow the simple description put forth by a long-lived spiral structure with a constant pattern speed.

4.5 Angular Offsets with Other Tracers

We saw in Chapter 3 that the HI distribution was not as concentrated to the spiral arms as H_2 and other star formation tracers. Since the HI emission is more evenly distributed than the 24μm emission, this may make the measurements of angular offsets challenging. Thus, we investigate whether there is evidence for angular offsets between other star formation tracers.

Eight of the galaxies had CO coverage from HERACLES with 13$''$ resolution. As described in Chapter 3, we process and convert those maps to produce deprojected maps of H_2 emission, which we transform to polar coordinates. Fig. 4.13 shows the H_2 emission in polar coordinates with 24μm contours overlaid for NGC 5194. Once again, we see that the offsets between these tracers must be small. As in §4.3, we measure angular offsets between the H_2 and 24μm emission by locating the peak of the cross-correlation function. Fig. 4.14 shows the radial profile of the angular offsets between these two tracers. In a similar fashion to Fig. 4.6, we find little

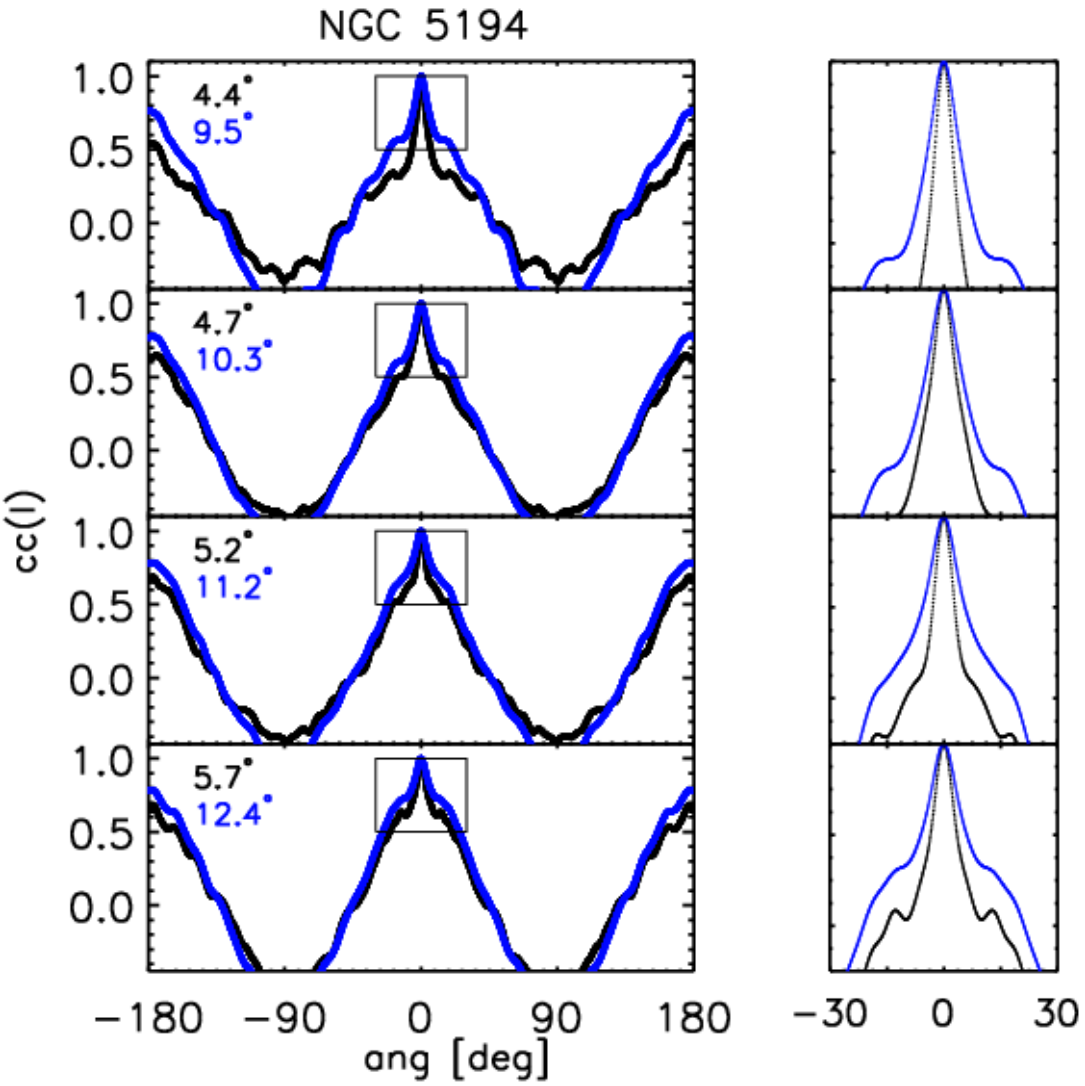

Figure 4.10: The effect of spatial resolution on the autocorrelation function of HI maps with 6″ (black) and 13″ (blue) resolution for NGC 5194 at a series of fiducial radii. Since the azimuthal resolution varies with radius, it is listed in the upper left of each panel. As one moves out in radius (from bottom to top) the azimuthal resolution size increases. As in Fig. 4.7 we zoom in on the peak between $\pm$ 30°. We see that as the size of azimuthal resolution increases, the peak of $cc(l)$ broadens and increases in value.

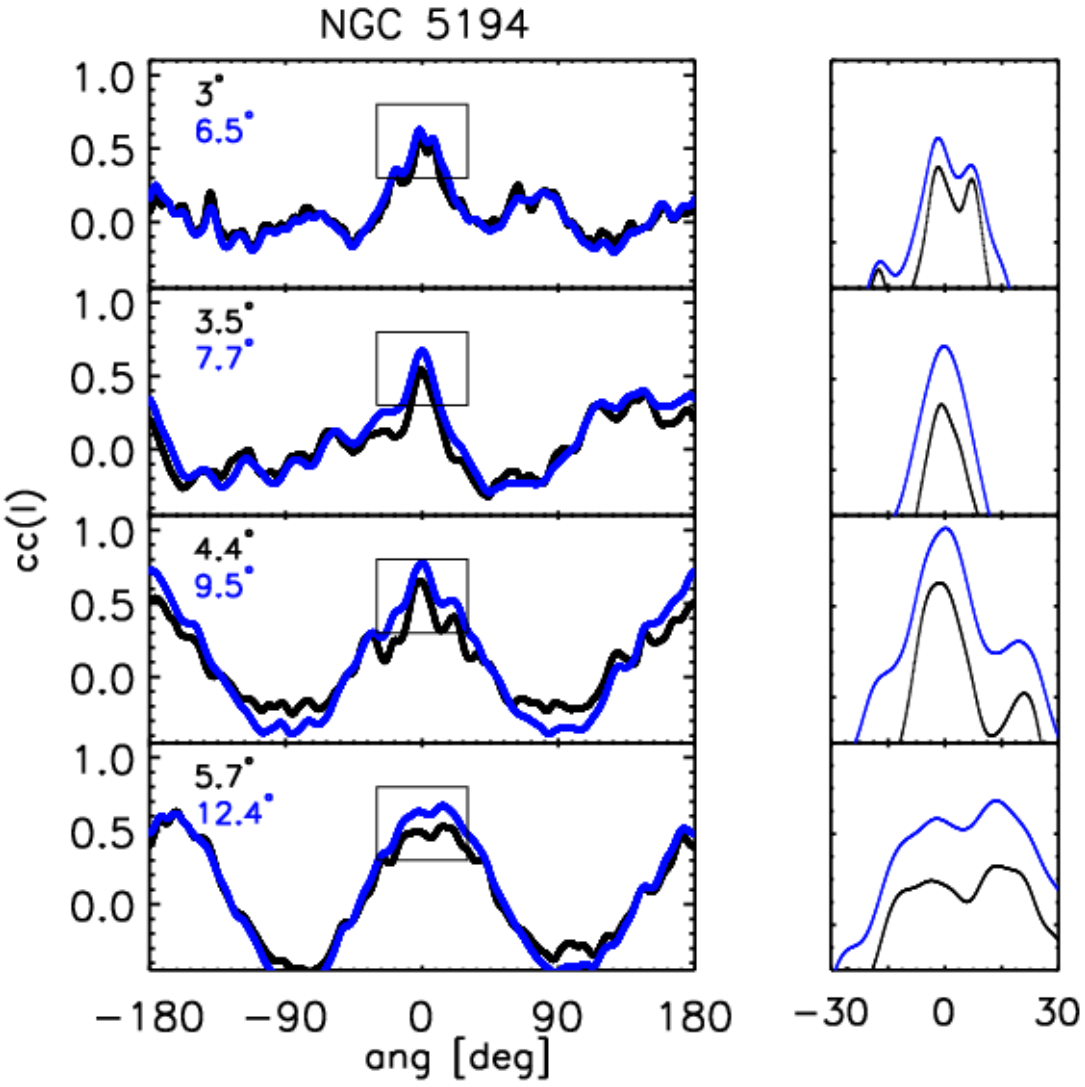

Figure 4.11: The effect of spatial resolution on the $cc(l)$ function calculated using HI and 24μm maps with 6″ (black) and 13″ (blue) resolution for NGC 5194 at a series of fiducial radii. Since the azimuthal resolution varies with radius, it is listed in the upper left of each panel. As one moves out in radius (from bottom to top) the azimuthal resolution size increases. As in Fig. 4.7 we zoom in on the peak between $\pm$ 30°. While the $cc(l)$ is roughly similar, features on the peak change substantially, which may introduce differences in the polynomial fit and the position of the maxima.

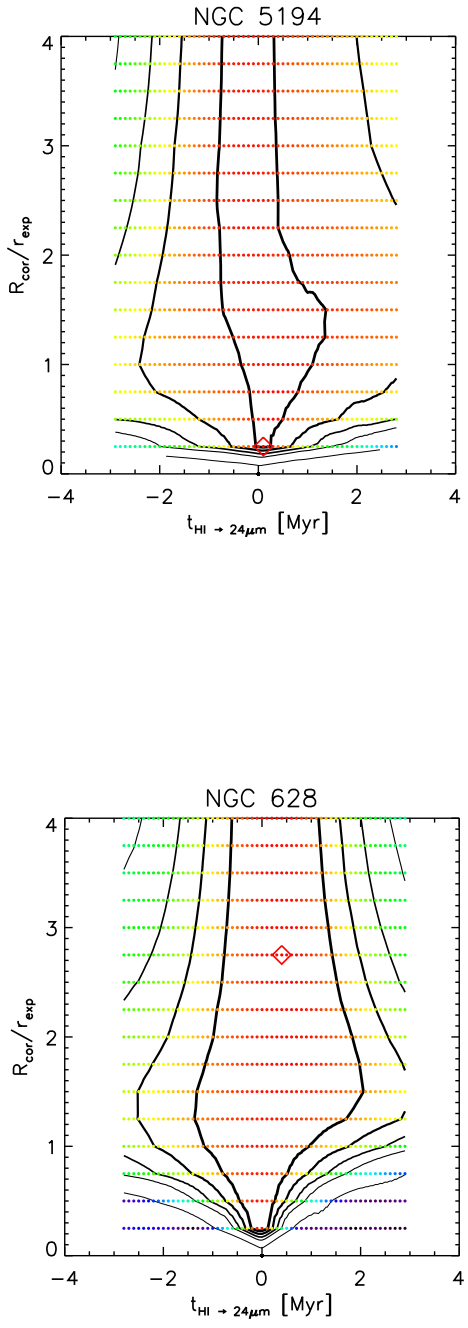

Figure 4.12: 2D Cross correlation coefficients for a range of $t_{HI\rightarrow 24\mu m}$ and R_{cor} for NGC 5194 (top) and NGC 628 (bottom). The colored points reflect the value of the 2D cross-correlation coefficient with red colors denoting high values and blue colors denoting low values. The contours delineate regions of the cross-correlation coefficient with thicker lines showing higher values. The red diamonds shows the parameter space value with the highest cross-correlation coefficient (NGC 5194: $R_{cor} = 0.2r_{exp}$ and $t_{HI\rightarrow 24\mu m}$=0.1 Myr; NGC 628: $R_{cor} = 2.8r_{exp}$ and $t_{HI\rightarrow 24\mu m}$=0.4 Myr).

evidence for offsets as presented by R69 and T08. There is some evidence for a sequence of offsets in NGC 6946 and NGC 5194. Thus, we examine these galaxies as well as NGC 628 for possible offsets between the SFR as described by the combination of 24μm and UV emission (see Chapter 3) and H_2 as well as the SFR and 3.6μm emission which traces the underlying old stellar population.

Fig. 4.15 and Fig. 4.16 show the angular offset profiles for cross-correlations of H_2 with the SFR and the SFR with 3.6μm emission repsectively. Of these galaxies, only NGC 6946 presents any trend suggestive of the picture of R69. However, it is important to note that many of these offsets are well below the resolution of the images, especially for the case of H_2, which only has 13$''$ resolution.

Despite having examined many variations of the cross-correlation as well as offsets between different tracers, we find no systematic ordering of star formation tracers through measures of angular offsets in the way put forth by R69 and others. While there may be some patches of star formation tracers that show by-eye offsets, an algorithmic analysis shows that such patches are isolated and there is no overall trend which supports the prediction of a model where the spiral structure is long-lived with a constant pattern speed and is shock triggering star formation. Our technique made use of the highest resolution to date and provided the timescales of star formation are at least a few Myrs, angular offsets should have been detectable. There are number of possible reasons why such a systematic ordering was not detected. It may be the case that there are no angular offsets between the tracers. This would be the case if the spiral structrue were simply a result of sheared patches of star forming regions or if the structure was rapidly dissolving and reforming. However, it is also possible that offsets are present, but that structure is more complex than a single pattern with a constant pattern speed. Indeed, recent studies have measured multiple pattern speeds for several spiral galaxies (Meidt et al. 2009). Furthermore, in Chapter 3 we saw that there was substantial star formation in the interarm regions (at least 30%). This may be obfuscating the offsets near the spiral arms due to our cross-correlation method which uses all azimuthal positions. In our toy model analysis (see §4.1.2) we saw that the dispersion and interarm star formation did cause the peak of the cross-correlation function to be slightly shifted. Interarm star formation patches may be the cause of the broad, bumpy cross-correlation function. The arms may also have slightly different offsets, which would introduce uncertainties when fitting over the whole galaxy. Thus, there is still room for the possibility that offsets between star formation tracers exists in the arms, but we may not be able to quantitatively measure them with this technique.

4.6 Dispersion of Star Formation Tracers

Given that the cross-correlation method may not be able to accurately measure angular offsets due to the complexity of the spiral structure and significant interarm star formation, we now examine in greater detail isolated regions near the arms of grand-design spirals by plotting az-

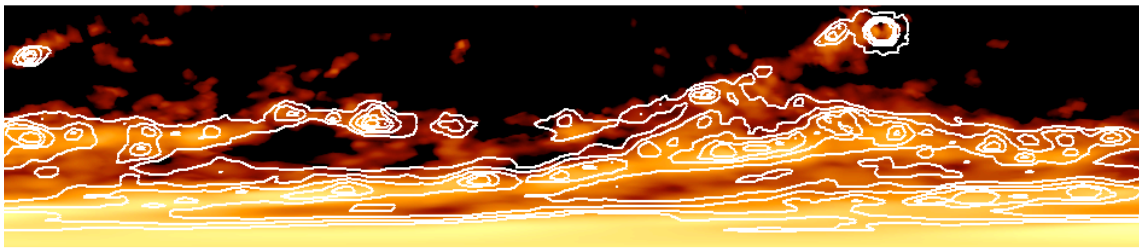

Figure 4.13: H_2 as traced by CO emission of NGC 5194 in polar coordinates with contours of the 24μm emission overlaid. As in Fig. 4.5, the angular offsets are small between the arm patterns of these two tracers.

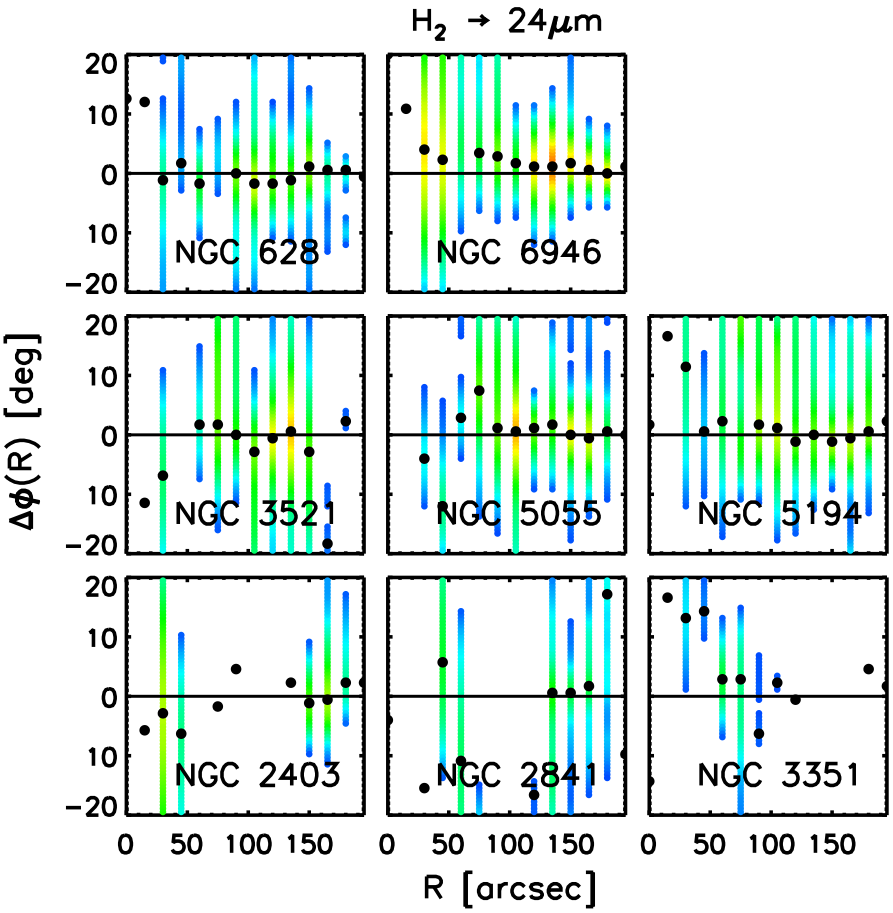

Figure 4.14: Radial profiles of the angular offsets based on the location of the peak of the cross-correlation function between H_2 and 24μm versus radius (black dots). The colored points reflect the value of the cross-correlation coefficients from high (red) to low (blue) in the range of $\pm 20°$. Values below 0.3, our chosen cutoff, are not shown. The angular offsets are corrected for the direction of rotation.

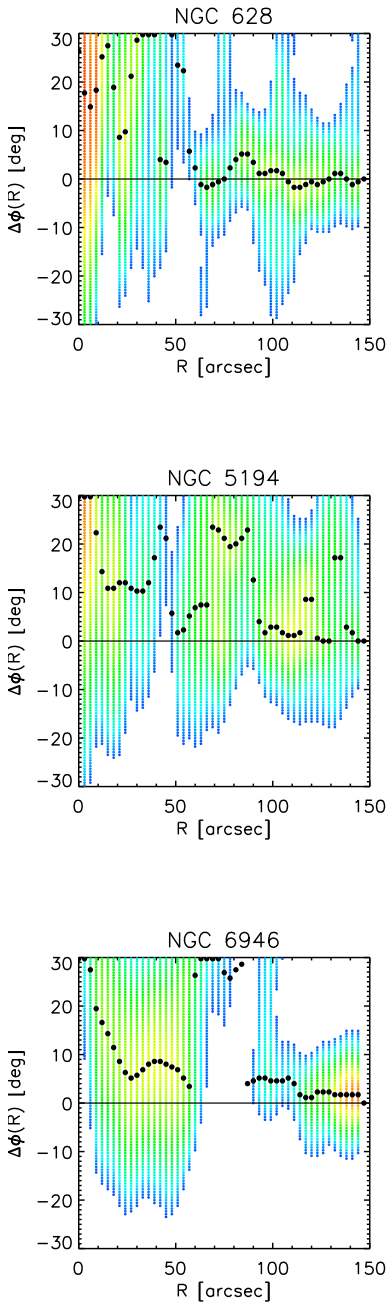

Figure 4.15: Radial profiles of the angular offsets based on the location of the peak of the cross-correlation function between H_2 and the SFR as traced by a combination of 24μm and UV emission versus radius (black dots). The colored points reflect the value of the cross-correlation coefficients from high (red) to low (blue) in the range of $\pm 20°$. Values below 0.3, our chosen cutoff, are not shown. The angular offsets are corrected for the direction of rotation.

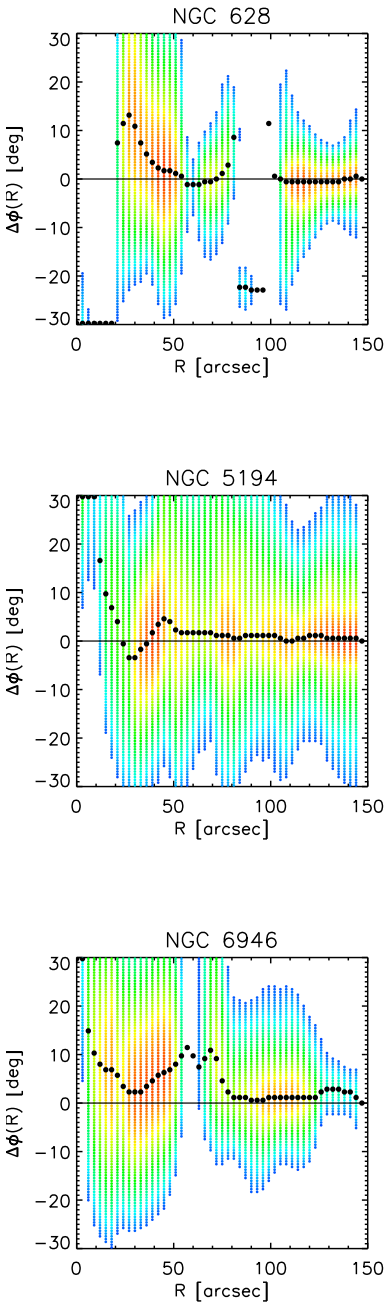

Figure 4.16: Radial profiles of the angular offsets based on the location of the peak of the cross-correlation function between the SFR as traced by a combination of 24μm and UV emission and the 3.6μm emission versus radius (black dots). The colored points reflect the value of the cross-correlation coefficients from high (red) to low (blue) in the range of $\pm 20^{\circ}$. Values below 0.3, our chosen cutoff, are not shown. The angular offsets are corrected for the direction of rotation.

imuthal profiles of the star formation tracers. If the arms are quasi-stationary and star formation follows the sequence of events put forth by R69 and others, one would expect to find the distribution of star formation tracers to be sharp on the upstream side of the arms with a gradual fall off and dispersion on the downstream side. Such profiles have been seen in simulations, which have examined spiral arm shock triggering with a rigid spiral potential (*e.g.* Dobbs & Bonnell 2006). As we saw with the toy model in §4.1.2, the autocorrelation function remains symmetrical regardless of this dispersion, thus we must turn to the profiles of the tracers directly to detect this.

In order to examine whether such dispersion is present in the galaxies in our sample, we have selected two grand-design spirals, NGC 628 and NGC 5194. Both galaxies have two prominent spiral arms, that can be easily fit with straight lines in $\log R$ and ϕ. Fig. 4.17 and 4.18 show the fitted arms in polar coordinates overlaid on the maps of three star formation tracers, H_2 (green), 24μm emission (red) and UV emission (blue). UV should have the longest decay times followed by 24μm and H_2 emission. At each radial position r, we note the position of each of the spiral arms $\phi_{peak,1}$ and $\phi_{peak,2}$ where 1 and 2 denote the arms furthest to left and right respectively in these figures. We then select a number of fiducial radii and plot the azimuthal flux profile for each tracer in terms of $\phi - \phi_{peak}$. Thus, $\phi - \phi_{peak} = 0$ denotes a position centered on the arm.

Fig. 4.19 shows the results for NGC 5194 and our three star formation tracers H_2 (green), 24μm (red) and UV (blue) emission. Note that the maps each have different resolutions (*i.e.*, 13$''$ for the CO maps which trace H_2 emission and 6$''$ for the 24μm and UV emission). Each panel has been centered on one of the two arms and in both panels a position zero marks the center of the spiral arm. To the left of zero is upstream to the arm and to the right is downstream from the arm. We expect to find the tracer emission to be more dispersed downstream. At some radii, this appears to be the case, but at most radii, the dispersion is very little if at all. In a similar fashion we plot the azimuthal profiles for NGC 628 in Fig. 4.20. For this galaxy, there is no obvious dispersion downstream of the spirals for any of the tracers. We also note that, for all three galaxies, the distribution of the tracers around the arms is quite broad and uneven. This is likely the cause of the broad, uneven cross-correlation function found in §4.3.

4.7 Conclusion

We have used high resolution images of a sample of 12 spiral galaxies to look for evidence for a model of spiral structure that is long-lived, quasi-stationary with a constant pattern speed and is shock triggering star formation. Such a model makes two important predictions: 1) that star formation tracers should be offset from one another reflecting the relative velocity between the disk and pattern and the onset time for star formation; and, 2) that the star formation tracers should exhibit a skewness or asymmetry in the spiral arms.

We have used an algorithmic technique developed by T08 to measure angular offsets be-

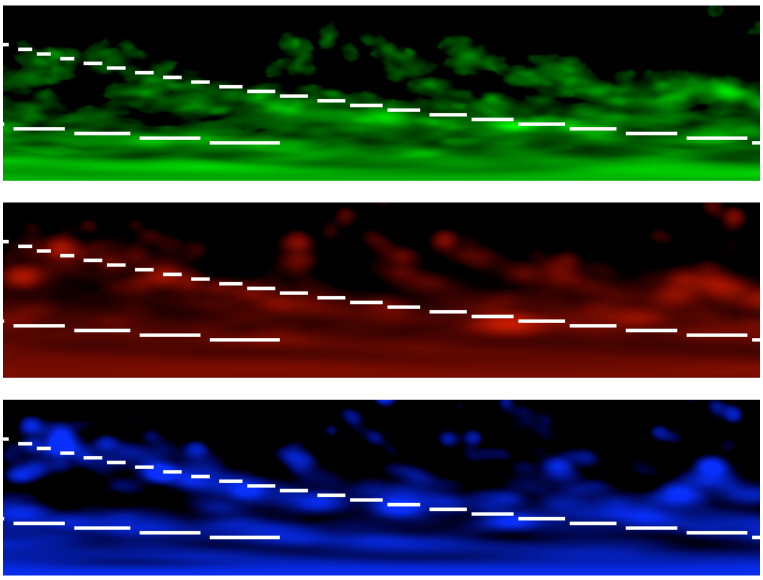

Figure 4.17: Fit of spiral arm in r, ϕ, (white lines) overlaid on maps in polar coordinates of NGC 628 for H_2 (green,top), 24μm emission (red, middle) and UV emission (blue, bottom).

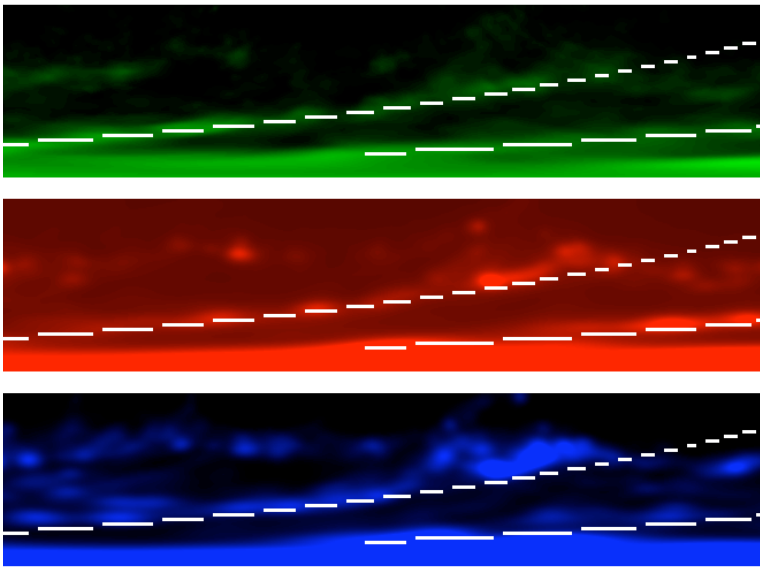

Figure 4.18: Fit of spiral arm in r, ϕ, (white lines) overlaid on maps in polar coordinates of NGC 5194 for H_2 (green,top), 24μm emission (red, middle) and UV emission (blue, bottom).

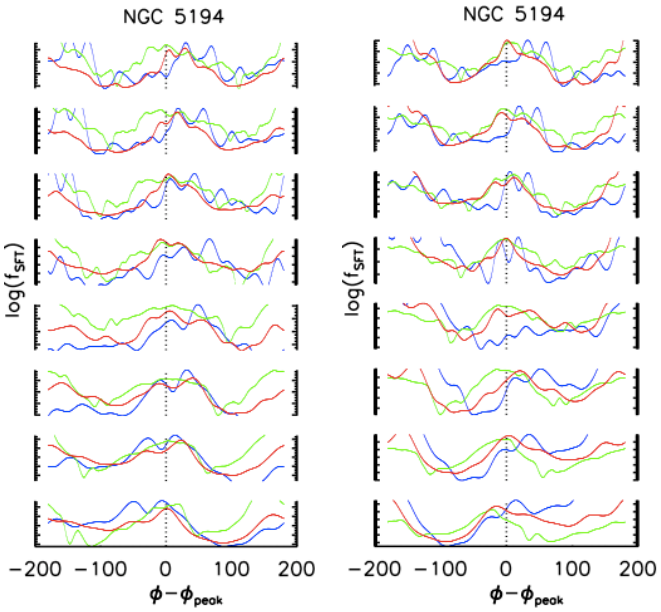

Figure 4.19: Azimuthal profiles of star formation tracers for NGC 5194. At a series of fiducial radii between 10″ (bottom) and 80″ (top), the profiles of H_2 (green), 24μm (red) and UV (blue) emission in terms of $\phi - \phi_{peak}$ are shown, where ϕ_{peak} is the azimuthal location of the spiral arm. The left panel shows the first arm in the left of Fig. 4.18 and the right panel references the arm furthest to the right. The profiles are arranged so that the galaxy rotation is toward positive angular values (right).

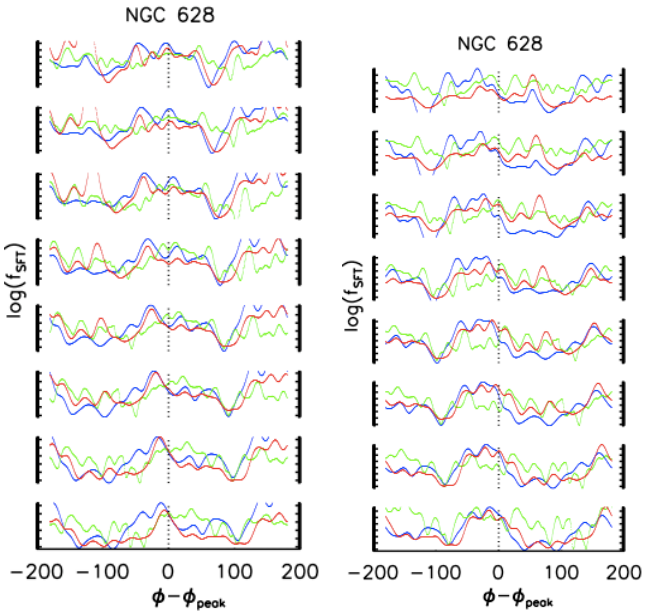

Figure 4.20: Azimuthal profiles of star formation tracers for NGC 628. At a series of fiducial radii between 10″ (bottom) and 80″ (top), the profiles of H_2 (green), 24μm (red) and UV (blue) emission in terms of $\phi - \phi_{peak}$ are shown, where ϕ_{peak} is the azimuthal location of the spiral arm. The left panel shows the first arm in the left of Fig. 4.18 and the right panel references the arm furthest to the right. The profiles are arranged so that the galaxy rotation is toward positive angular values (right).

tween star formation tracers in high-resolution images of 12 spiral galaxies and found that the angular offsets did not have a systematic ordering in the way predicted by the the simple prescription of R69. We specifically measured offsets between HI and 24μm emission in order to directly compare with the work of T08 and are unable to reproduce their results. We attribute this to subjective decisions in fitting the peak of the $cc(l)$ and the sensitivity of the offsets to small changes in the way in which the $cc(l)$ is calculated. We also note that all of the offsets found by T08 are below the resolution limit. Whether or not this is of a concern remains unclear. Since the cross-correlation involves all azimuthal positions, it may be possible to probe below the resolution limit. We also attempted to calculate angular offsets using the 2D cross-correlation and between other star formation tracers including H_2 as traced by CO, the SFR and 3.6μm images. The radial profiles of angular offsets did not agree with the findings of T08 and did not match the predictions of R69. This raises serious questions for a model of spiral structure that is long-lived with a constant pattern speed and is shock triggering star formation.

We examined in greater detail the azimuthal profiles of star formation tracers in two grand-design spirals with two arms and did not find that the tracers were dispersed downwind of the arms as one would expect in the case of a quasi-stationary spiral that is shock triggering star formation in the arms.

As we saw in Chapter 3, both the star formation efficiency and molecular cloud formation efficiency were similar in the arm and interarm regions and there is a comparable fraction of interarm star formation. Combined with our results in this chapter, this suggests that spiral arms play only a minor role in star formation and likely only at the level of reorganizing the disk material.

The fact that there is no evidence for a long-lived spiral structure that is shock triggering star formation lends support to a model with a transient spiral structure that reorganizes the ISM (*e.g.* Elmegreen & Elmegreen 1986; Dobbs et al. 2008; Sellwood 2010) or models that have spiral arms forming due to the shearing of gas and stars by differential rotation (*e.g.* Seiden & Gerola 1979 and Elmegreen et al. 2003). Simulations largely support such pictures and other observational studies have shown that most spiral structures are quite complex with multiple pattern speeds (*e.g.* Meidt et al. 2009). However, this work does not completely rule out the shock triggering scenario and a long-lived spiral structure as posited by R69 and others. Angular offsets between star formation tracers may be too small to measure with accuracy at our resolution, streaming motions may disrupt the relative positions of the tracers and remove the dispersion and even a small fraction of interarm star formation could make measurements very challenging. However, the lack of evidence for this scenario and the fact that the overwhelming majority of simulations also point to a different picture raises questions for the validity of this model.

Dobbs & Pringle (2010) have recently compared four different models of spiral structure using simulations and comparing the distribution of stellar clusters. As we saw in §4.1.1, the long-lived spiral structure was simulated using a rigid potential and indeed the ordering of the

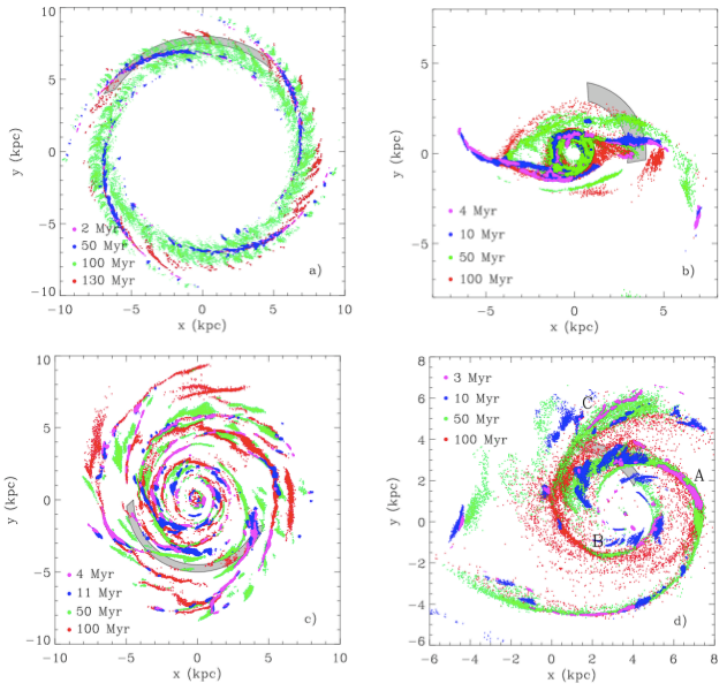

Figure 4.21: Distribution of stellar cluster ages in the spiral arms of a long-lived spiral potential with a constant pattern speed (top left), a barred galaxy (top bottom), a self-excited flocculent galaxy (bottom left), and a galaxy interacting with a companion (bottom right) (Figure 2 of Dobbs & Pringle (2010)). While the ordering of the stellar clusters is systematic in the long-lived spiral, the other cases show a much more complex distribution.

stellar cluster ages seems to fit the predictions of R69 and others (see Fig. 4.1). Since the long-lived structure requires a rigid potential in order to ensure its longevity, the other three cases may be more realistic (see Fig. 4.21 for all four cases). In these cases the ordering is much more complex. For the flocculent galaxy, each segment of the spiral arms contains clusters of different ages. The interacting galaxy has an almost incoherent distribution. Thus, while a long-lived spiral structure with a constant pattern speed does not agree with our observational results, other theories of spiral structure might. It is clear that a systematic comparison between observations and simulations will be required in order to uncover how spiral structures form and persist.

Chapter 5

Conclusions & Outlook

Spiral arms are a beautiful instance of many physical processes conspiring to create an enigmatic and enthralling structure. While the nature of this structure is as yet to be fully understood, we have investigated how its presence can affect the observable properties of the host galaxy. We have looked specifically at how spiral structure and other non-axisymmetric features affect the secular evolution of galaxies and we have explored the influence of spiral arms on star formation. We have also examined how star formation tracers can be used to constrain theories of spiral structure formation and its longevity. We now briefly summarize the main results of this work and suggest directions for future research.

5.1 Secular Evolution

In Chapter 2 we examined the strength of gravitational torques induced by non-axisymmetric features, like bars and spiral arms, on the stellar mass distribution. If such torques are strong enough such that they act on a timescale much less than a Hubble time, they could lead to angular momentum and matter transport in the disk. Such mechanisms are thought to be responsible for the development of "pseudo-bulges" and outer disk truncations. We first used a series of N-body/SPH simulations to test our method and determine the relative role of dark matter torques on the stellar distribution, which cannot be measured by observations. We then chose a sample of 24 nearby spiral galaxies and created pixel-by-pixel mass maps from which we derived torque maps. The individual torque maps showed that the barred galaxies had the strongest torques. Since the longevity and persistence of a spiral structure remain unclear, as it may dissolve and reform over time, we avoided the assumption that the spiral and bar patterns observed today are typical of the past and future by stacking the sample to replace the time average by an ensemble average. *The stacked sample showed that the torques transport angular momentum outward over much of the disk. The torques were strong enough to be effective at redistributing angular momentum on a timescale of $\sim$ 4 Gyr in the inner regions of the disk (within one disk scale length). This work presents the first observational study to determine the strength of torque-driven angular momentum flow for stars in a sample of galaxies.*

Our sample, however, was modest in size (24 galaxies) preventing us from answering a number of interesting questions including whether all types of galaxies exhibit such torques. Even in our modest sample there appeared to be a difference between barred and unbarred galaxies, with barred galaxies having stronger torques. If we extended such an analysis to a sample of $\sim$ 1000 galaxies we could not only confirm our results with greater confidence, but also group the galaxies based on certain properties including total stellar mass, colour, star formation rate, bulge-to-disk ratio and the presence and strength of a bar. Thus, we may be able to uncover correlations between the strength of gravitational torques and the observable properties in disk galaxies.

Beyond this direct extension, a number of other interesting problems presented themselves while working on this project. For instance, to what extent and under which conditions does angular momentum flow translate into matter redistribution? Angular momentum flow leads not only to matter flow, but also to disk heating, increased orbital eccentricities and can also be absorbed by the surrounding dark halo (Athanassoula 2002 and 2003; Sellwood & Binney 2002). In order to disentangle this complex process, one could use numerical simulations to trace how angular momentum flow translates into each of these mechanisms. With an understanding of how torques translate into matter redistribution, we could then apply the stacked torque profile on an average mass density profile to see its evolution. Such a study would allow us to see how matter redistribution affects exponential profiles and if it leads to the formation of "pseudo-bulges", disk truncations and other features.

5.2 Star Formation & Spiral Arms

In Chapter 3 we explored the interplay between star formation and spiral arms. The fact that spiral arms are visible to us means that there must be enhanced star formation in these regions. However, it has yet to be quantified how much star formation occurs in the interarm region and whether the spiral arms are shock triggering star formation in a way that means these regions are more efficient at forming stars per unit gas density. Recently L08 and B08 have shown that the SFE in nearby spiral galaxies does not vary systematically with other galaxy properties to first order on a pixel-by-pixel basis. However, they did not examine if there were differences between the arm and interarm regions. We used two grand-design spirals and a more flocculent spiral galaxy with high-resolution images that trace recent star formation — far-ultraviolet (GALEX NGS) and 24μm emission (*Spitzer* SINGS) and cold gas — CO (HERACLES) and HI (THINGS) to determine the amount of star formation in the interarm regions and whether the arms had a higher SFE due to shock triggering. We defined the arm and interarm regions using 3.6μm (IRAC) images from Spitzer that were median-filtered and Fourier-reconstructed to spatially filter the spiral arms. We chose 3.6μm images, as they are least affected by young stars, allowing us to use the location of stellar mass density enhancements to define the spiral arms. The two grand-design spirals showed a clear two-armed structure, while the flocculent

one was more complex. The arm and interarm regions were defined by azimuthal fractions of the highest and lowest pixel values in these images.

Perhaps not unexpected, we found, that the tracers were more concentrated to the arms than the stellar mass density. *However, the majority of the star formation was found in the interarm regions, using a definition of spiral arms with 25% of the highest pixels. Even with a generous definition of spiral arms, at least 30% of the star formation tracer emission was in the interarm regions.* We compared the SFE based on the molecular gas in the arm and interarm regions and found that there was no obvious enhancement of the SFE in the grand-design spirals. For the more flocculent spiral, with a more complex structure, some enhancement was found in the arms, but it is plausible that, in light of a weak or no dynamical spiral, our definition of the spiral arm location was biased by young stars. We also examined the ratio of H_2 to HI in the arm and interarm regions and found only a weak enhancement of the molecular gas fraction in the arms. However, at fixed gas surface density, no significant enhancement of the molecular gas fraction was found. *These results show that, while there is an enhancement in the star formation rate in the spiral arms, spiral arms do not have an enhanced SFE as one would expect if the arms were shock triggering star formation. Rather, spirals act to concentrate the gas in the arms, which may aid cloud formation.*

While L08 and B08 found that the spirals in their sample had a constant SFE to first order with a median of $5.25 \pm 2.5 \times 10^{-10}$ yr^{-1}, there is considerable scatter. It would be interesting to divide the spiral sample based on spiral classification (*i.e.* grand-design, intermediate and flocculent) to uncover if there is a difference in the SFE for these spiral types. While Elmegreen & Elmegreen (1986) found that the galaxy-averaged star formation rates determined from Hα and UV fluxes showed no difference for galaxies with or without grand-design spirals, Phillipps & Disney (1985) found the flocculent galaxies had higher surface brightnesses. In light of the recent increase in high-resolution multi-band images, it would be interesting to examine possible differences in the SFR and SFE of grand-design and flocculent spirals. We have already begun a preliminary study using the 12 spiral galaxies in the study of L08. It seems that, particularly at low gas densities, the grand-design spirals have a higher SFE than the flocculent spirals. The median SFE of grand-design spirals is 7.5×10^{-10} yr^{-1}, while flocculent spirals have a median SFE of 4.7×10^{-10} yr^{-1}. These preliminary results need to be confirmed by extending this to a larger sample and investigating this in greater detail.

5.3 Towards an Understanding of Spiral Structure

Since the SFE was not enhanced in the arms as opposed to the interarm regions, this raised questions for a model of spiral structure which is long-lived with a constant pattern speed and is shock triggering star formation. In Chapter 4 we decided to examine if there was any other evidence for such a model. If spiral structure can be explained in this way, one expects to find angular offsets between star formation tracers that depend on the relative speed between the

spiral pattern and the disk and the onset time of star formation. One would also expect that the star formation and gas tracers should show an asymmetry in the spiral arms with a dispersion downstream to the arms within corotation. We used a sample of 12 spiral galaxies with images of gas and star formation tracers to look for evidence of these two predictions.

Following Tamburro et al. (2008) we used an algorithmic technique to measure angular offsets by cross-correlating annuli of star formation and gas tracers. As Tamburro et al. (2008), we looked for angular offsets between HI and 24 μm emission and also extended their study to look for offsets between other tracers including CO, 3.6μm emission and the SFR (a combination of UV and 24μm emission). Unlike Tamburro et al. (2008) we did not find radial profiles of angular offsets that would be consistent with a spiral structure with a constant pattern speed that was shock triggering star formation. We examined the reasons for this disagreement and found that their method was very sensitive to subjective choices in fitting the cross-correlation peaks and that the angular offsets were all below the resolution limit of the images. Using two grand-design spirals, we examined azimuthal profiles of star formation tracers in the regions of the spiral arms and found no obvious asymmetry of these tracers as one would expect. *Thus, despite having the highest resolution images to date, neither a systematic ordering of star formation tracers nor an asymmetry of star formation tracers in the arms is detectable, raising serious questions for a model of spiral structure that is long-lived with a constant pattern and is shock triggering star formation.* It may be that our method was unable to uncover such signatures due to effects like interarm star formation, different offset patterns for individual arms or multiple pattern speeds. However, our findings in Chapter 2 showed that, in the inner regions of the disk, angular momentum redistribution occurs on a timescale of $\sim$ 4 Gyr. This would likely affect even the strongest spiral patterns and raises questions as to their longevity. Furthermore, simulations have consistently pointed towards a picture of spiral structure that is transient and recurring and unless one applies a rigid spiral potential, angular offsets are not observed in simulations (Dobbs et al. 2008).

Sellwood and co-workers have developed a theory for a transient spiral structure that has already proven to have some agreements with observations (Sellwood 2010). In Sellwood's model, the scattering of stars at resonances, particularly corotation, changes the distribution function which seeds the growth of a new instability which develops a new spiral structure. Such a model also predicts radial migration of stars which has been examined by simulations (Sellwood & Binney 2002; Roškar et al. 2008).

Recently Dobbs & Pringle (2010) conducted a series of simulations investigating possible mechanisms for the excitation of spiral structure. They looked at excitation due to bars and companions, a global density wave and self-excitation. They located dense gas regions in different snapshots in the simulations and assumed those regions would form stellar clusters at those times. They then were able to locate the cluster positions relative to the arms at later times. They found that the distribution of stellar cluster ages varied significantly depending on the mechanism for spiral structure excitation.

The next step in this work will be to compare our observations with such simulations in a consistent fashion.

5.4 Conclusion

Taken together, the results of this work have shown that spiral structure plays perhaps less of a role in shaping the observable properties of disk galaxies than common lore in astronomy suggests. In terms of the dynamical secular evolution of galaxies, it is barred galaxies that have the strongest gravitational torques. Furthermore, spiral arms do not play an exceptional role in producing stars beyond increasing the gas density in the arms. It also seems that spiral structure is likely a transient, recurring phenomenon in the way that simulations have suggested, since we have found that several predictions of a long-lived spiral structure model seem not to be borne out. However, there remains many open questions as to how galaxies develop spiral structure and how it is maintained. Future advances made in estimating the distribution of stellar mass with higher resolution images and improved models will allow us to further elucidate how spiral structure acts to reorganize matter in the stellar disk. The next generation of telescopes and satellites will present exciting new results. For example, the Atacama Large Millimeter Array (ALMA) will allow us to probe with higher spatial resolution the molecular gas distribution in galaxies and the Herschel satellite will allow us to better map the dust distribution. This will allow us to probe in finer detail the complex processes of star formation and their connection to spiral arms. By combining these observations with high resolution simulations we may soon be able to resolve the debate between different spiral structure models. In short, we are close to answering some of the most fundamental questions surrounding how these beautiful structures form and persist.

Acknowledgements

While working on this thesis I have made many friendships and met many interesting people who have made this time both enriching and fulfilling. I thank them for traveling this road with me and sharing this experience.

First and foremost, I wish to thank my supervisor, Hans-Walter Rix. I am deeply indebted to him for his mentorship, tireless dedication to working with me and encouraging words throughout this process. His contagious enthusiasm for science and learning has made these years such a pleasure.

I feel extremely lucky to have been able to work at the MPIA, which has provided such a rich environment in which to work and learn. I have benefited from many discussions with colleagues and friends including Eric Bell, Kris Blindert, Cassie Fallscheer, Christine Ruhland, Christian Schwab, Rosalind Skelton, Ramin Skibba, and Hsiang-Hsu Wang. I am particularly grateful for the assistance and friendship of Stefano Zibetti, who patiently showed me so many computing techniques and was a tireless observing companion in Chile. I am also indebted to Adam Leroy and Fabian Walter who have contributed many ideas, comments and corrections to this work. I would also like to thank my office mate, Aurora Sicilia-Aguilar for living through all the drilling noise with me. I thank the MPIA for the financial support to travel to conferences, where I had interesting exchanges with many people including Lia Athanassoula, Jerry Sellwood and Bruce Elmegreen.

I am grateful to my thesis committee- Ralf Klessen, Fabian Walter and Frank van den Bosch for all their comments and suggestions. I also thank Ralf Klessen, Matthias Bartelmann and Eva Grebel for agreeing to be on my exam committee and for reading this work.

I feel very fortunate to have shared my time in Heidelberg with my IMPRS generation and for the assistance of the IMPRS program. I have many fond memories of our retreats, BBQs and Christmas parties. I thank Leonard Burtscher for sharing the pleasure and the work of being IMPRS representative. I owe a great deal to Christian Fendt, not only for his work as IMPRS co-ordinator, but also for his help, particularly during my first days in Heidelberg.

I am especially indebted to my IMPRS friends with whom I've shared so many fun nights including Ioanna Arka, Denija Crnojevic, Baybars Kuelebi, Giovanni Natale, Massimo Viola and Olga Zacharopoulou. I thank them for making me smile and laugh on so many occasions and for being the kind of friends you can always count on.

I feel so fortunate to have lived in Rohrbach and Berlin, two places which served as a

backdrop to this work and offered such wonderful homes away from home. There have been many people in both cities and beyond which have made my stay in Germany so enriching. I thank Hans-Walter Rix and Mary Beth Robinson for sharing the natural beauty of the Alps and Arizona.

I am especially grateful to Stéphane Courteau, my M.Sc. supervisor, for encouraging me to come to Heidelberg and offering advice and encouragement during many stages of my time here. I thank Jean Godin for inspiring me to pursue astronomy and for giving me my first look through a telescope.

I feel very fortunate to have had a loving and supporting family. I thank my mother, Rosalie Foyle, not only for correcting many typographical errors in this work, but more importantly, for always believing in me. I thank my father, Marcus Foyle, for instilling in me the wonders of science at an early age.

Not last, from the bottom of my heart, I thank my partner, Simon Kiss, for his love, friendship and support. I am forever grateful for his being so willing and eager to join me in Germany, for sharing so many adventures during this time and for encouraging me to try new things and face my fears. He has believed in me even when I didn't and I am a stronger, smarter and kinder person because of him.

Bibliography

Abazajian, K. N., et al. 2009, ApJS, 182, 543

Abd-al-Rahman Al Sufi, 964. Book of Fixed Stars. Isfahan, Persia

Athanassoula, E. 1980, A&A, 88, 184

Athanassoula, E. 1984, Phys. Rep., 114, 321

Athanassoula, E., & Bosma, A. 1985, ARA&A, 23, 147

Athanassoula, E. 2002, ApJ, 569, L83

Athanassoula, E. 2003, arXiv:astro-ph/0302521

Balbus, S. A. 1988, ApJ, 324, 60

Baldry, I. K., Glazebrook, K., Brinkmann, J., Ivezić, Ž., Lupton, R. H., Nichol, R. C., & Szalay, A. S. 2004, ApJ, 600, 681

Barazza, F. D., Jogee, S., & Marinova, I. 2008, Astronomical Society of the Pacific Conference Series 396, 351

Barden, M., et al. 2005, ApJ, 635, 959

Barnes, J. E., & Hernquist, L. 1996, ApJ, 471, 115

Bell, E. F., & de Jong, R. S. 2001, ApJ, 550, 212

Bell, E. F., McIntosh, D. H., Katz, N., & Weinberg, M. D. 2003, ApJS, 149, 289

Bell, E. F., et al. 2004, ApJ, 608, 752

Bell, E. F., et al. 2006, ApJ, 640, 241

Bennett, C. L., et al. 2003, ApJS, 148, 1

Berentzen, I., Heller, C. H., Shlosman, I., & Fricke, K. J. 1998, MNRAS, 300, 49

Bertin, G. 1983, A&A, 127, 145

Bertin, G., Lin, C. C., Lowe, S. A., & Thurstans, R. P. 1989, ApJ, 338, 78

Bertin, G., Lin, C. C., Lowe, S. A., & Thurstans, R. P. 1989, ApJ, 338, 104

Bertin, G., & Lin, C. C. 1996, Spiral structure in galaxies a density wave theory, Publisher: Cambridge, MA MIT Press, 1996

Bertin, G., & Amorisco, N. C. 2010, A&A, 512, A17

Bigiel, F., Leroy, A., Walter, F., Brinks, E., de Blok, W. J. G., Madore, B., & Thornley, M. D. 2008, AJ, 136, 2846

Binney, J., & Merrifield, M. 1998, Galactic astronomy, NJ : Princeton University Press, 1998.

Binney, J., & Tremaine, S. 2008, Galactic Dynamics: Second Edition, Princeton University Press, Princeton, NJ USA, 2008.

Bland-Hawthorn, J., Vlajić, M., Freeman, K. C., & Draine, B. T. 2005, ApJ, 629, 239

Blitz, L., & Rosolowsky, E. 2006, ApJ, 650, 933

Blumenthal, G. R., Faber, S. M., Primack, J. R., & Rees, M. J. 1984, Nature, 311, 517

Boggess, N. W., et al. 1992, ApJ, 397, 420

Boissier, S., Prantzos, N., Boselli, A., & Gavazzi, G. 2003, MNRAS, 346, 1215

Boroson, T. 1981, ApJS, 46, 177

Bosma, A., Ekers, R. D., & Lequeux, J. 1977, A&A, 57, 97

Bosma, A. 1981, AJ, 86, 1825

Bothun, G. D. 1982, PASP, 94, 774

Bottema, R. 2003, MNRAS, 344, 358

Bournaud, F., & Combes, F. 2002, A&A, 392, 83

Bournaud, F., Combes, F., & Semelin, B. 2005, MNRAS, 364, L18

Bruzual, G., & Charlot, S. 2003, MNRAS, 344, 1000

Buta, R., Laurikainen, E., & Salo, H. 2004, AJ, 127, 279

Calzetti, D., et al. 2007, ApJ, 666, 870

Carlberg, R. G., & Freedman, W. L. 1985, ApJ, 298, 486

Cayatte, V., van Gorkom, J. H., Balkowski, C., & Kotanyi, C. 1990, AJ, 100, 604

Cepa, J., & Beckman, J. E. 1990, ApJ, 349, 497

Chakrabarti, S. 2008, arXiv:0812.0821

Cole, S., et al. 2005, MNRAS, 362, 505

Courteau, S. 1996, ApJS, 103, 363

Courteau, S. 1997, AJ, 114, 2402

Courteau, S., Andersen, D. R., Bershady, M. A., MacArthur, L. A., & Rix, H.-W. 2003, ApJ, 594, 208

Courteau, S., Dutton, A. A., van den Bosch, F. C., MacArthur, L. A., Dekel, A., McIntosh, D. H., & Dale, D. A. 2007, ApJ, 671, 203

Cox, T. J., Jonsson, P., Primack, J. R., & Somerville, R. S. 2006, MNRAS, 373, 1013

Curir, A., Mazzei, P., & Murante, G. 2008, A&A, 481, 651

Dalcanton, J. J., Spergel, D. N., & Summers, F. J. 1997, ApJ, 482, 659

Davis, M., Efstathiou, G., Frenk, C. S., & White, S. D. M. 1985, ApJ, 292, 371

Debattista, V. P., & Sellwood, J. A. 2000, ApJ, 543, 704

Debattista, V. P., Mayer, L., Carollo, C. M., Moore, B., Wadsley, J., & Quinn, T. 2006, ApJ, 645, 209

de Jong, R. S. 1996, A&A, 313, 45

del Rio, M. S., & Cepa, J. 1998, A&A, 340, 1

de Vaucouleurs, G. 1958, ApJ, 127, 487

de Vaucouleurs, G. 1959, Handbuch der Physik, 53, 311

Dobbs, C. L., Bonnell, I. A., & Pringle, J. E. 2006, MNRAS, 371, 1663

Dobbs, C. L., & Bonnell, I. A. 2007, MNRAS, 376, 1747

Dobbs, C. L., & Bonnell, I. A. 2008, MNRAS, 385, 1893

Dobbs, C. L., Theis, C., Pringle, J. E., & Bate, M. R. 2010, MNRAS, 403, 625

Dobbs, C. L., & Pringle, J. E. 2010, arXiv:1007.1399

Dutton, A. A., van den Bosch, F. C., Dekel, A., & Courteau, S. 2007, ApJ, 654, 27

Efstathiou, G., Lake, G., & Negroponte, J. 1982, MNRAS, 199, 1069

Egusa, F., Kohno, K., Sofue, Y., Nakanishi, H., & Komugi, S. 2009, ApJ, 697, 1870

Elmegreen, D. M., & Elmegreen, B. G. 1982, MNRAS, 201, 1021

Elmegreen, B. G., & Elmegreen, D. M. 1983, ApJ, 267, 31

Elmegreen, D. M., & Elmegreen, B. G. 1984, ApJS, 54, 127

Elmegreen, B. G., & Elmegreen, D. M. 1985, ApJ, 288, 438

Elmegreen, B. G., & Elmegreen, D. M. 1986, ApJ, 311, 554

Elmegreen, B. G. 1995, The Physics of the Interstellar Medium and Intergalactic Medium, 80, 218

Elmegreen, B. G., Elmegreen, D. M., & Leitner, S. N. 2003, ApJ, 590, 271

Erwin, P., Beckman, J. E., & Pohlen, M. 2005, ApJ, 626, L81

Eskridge, P. B., et al. 2000, AJ, 119, 536

Eskridge, P. B., et al. 2002, ApJS, 143, 73

Fall, S. M., & Efstathiou, G. 1980, MNRAS, 193, 189

Ferrière, K. M. 2001, Reviews of Modern Physics, 73, 1031

Foyle, K., Courteau, S., & Thacker, R. J. 2008, MNRAS, 386, 1821

Foyle, K., Rix, H.-W., & Zibetti, S. 2010, MNRAS, 976

Freeman, K. C. 1970, ApJ, 160, 811

Frei, Z., Guhathakurta, P., Gunn, J. E., & Tyson, J. A. 1996, AJ, 111, 174

Fujimoto, M. 1968, ApJ, 152, 391

Gadotti, D. A. 2010, arXiv:1003.1719

Garcia-Burillo, S., Guelin, M., & Cernicharo, J. 1993, A&A, 274, 123

Gil de Paz, A., et al. 2007, ApJS, 173, 185

Gittins, D. M., & Clarke, C. J. 2004, MNRAS, 349, 909

Gnedin, O. Y., Goodman, J., & Frei, Z. 1995, AJ, 110, 1105

Gnedin, N. Y., & Kravtsov, A. V. 2010, arXiv:1004.0003

Goldreich, P., & Lynden-Bell, D. 1965, MNRAS, 130, 125

Governato, F., Willman, B., Mayer, L., Brooks, A., Stinson, G., Valenzuela, O., Wadsley, J., & Quinn, T. 2007, MNRAS, 374, 1479

Grosbøl, P., Patsis, P. A., & Pompei, E. 2004, A&A, 423, 849

Haan, S., Schinnerer, E., Emsellem, E., García-Burillo, S., Combes, F., Mundell, C. G., & Rix, H.-W. 2009, ApJ, 692, 1623

Helfer, T. T., Thornley, M. D., Regan, M. W., Wong, T., Sheth, K., Vogel, S. N., Blitz, L., & Bock, D. C.-J. 2003, ApJS, 145, 259

Helou, G. 1986, ApJ, 311, L33

Hitschfeld, M., Kramer, C., Schuster, K. F., Garcia-Burillo, S., & Stutzki, J. 2009, A&A, 495, 795

Hogg, D. W. 2009, arXiv:0910.3374

Hohl, F. 1970, NASA Tech. Rep., NASA-TR R-343, 2 + 108 p., 343

Hubble, E. P. 1926, ApJ, 64, 321

Humphreys, R. M., & Sandage, A. 1980, ApJS, 44, 319

Hunt, L. K., et al. 2008, A&A, 482, 133

Jarrett, T. H., Chester, T., Cutri, R., Schneider, S. E., & Huchra, J. P. 2003, AJ, 125, 525

Jogee, S., Scoville, N., & Kenney, J. D. P. 2005, ApJ, 630, 837

Julian, W. H., & Toomre, A. 1966, ApJ, 146, 810

Kendall, S., Kennicutt, R. C., Clarke, C., & Thornley, M. D. 2008, MNRAS, 387, 1007

Kennicutt, R. C., Jr. 1981, AJ, 86, 1847

Kennicutt, R., Jr., & Hodge, P. 1982, ApJ, 253, 101

Kennicutt, R. C., Jr. 1982, AJ, 87, 255

Kennicutt, R. C., Jr. 1989, ApJ, 344, 685

Kennicutt, R. C., Jr. 1998, ApJ, 498, 541

Kennicutt, R. C., Jr., et al. 2003, PASP, 115, 928

Kim, C.-G., Kim, W.-T., & Ostriker, E. C. 2008, ApJ, 681, 1148

Kim, C.-G., Kim, W.-T., & Ostriker, E. C. 2010, arXiv:1006.4691

Knapen, J. H., Cepa, J., Beckman, J. E., Soledad del Rio, M., & Pedlar, A.1993, ApJ, 416, 563

Knapen, J. H., Beckman, J. E., Cepa, J., & Nakai, N. 1996, A&A, 308, 27

Knapen, J. H. 1997, MNRAS, 286, 403

Koda, J. 2008, Astronomical Society of the Pacific Conference Series, 396, 97

Koda, J., et al. 2009, ApJ, 700, L132

Kormendy, J., & Kennicutt, R. C., Jr. 2004, ARA&A, 42, 603

Kormendy, J., & Fisher, D. B. 2005, Revista Mexicana de Astronomia y Astrofisica Conference Series, 23, 101

Kranz, T., Slyz, A., & Rix, H.-W. 2003, ApJ, 586, 143

Krumholz, M. R., & McKee, C. F. 2005, ApJ, 630, 250

Krumholz, M. R., & Matzner, C. D. 2009, ApJ, 703, 1352

Kuno, N., Tosaki, T., Nakai, N., & Nishiyama, K. 1997, PASJ, 49, 275

Larson, R. B. 2003, Reports on Progress in Physics, 66, 1651

Leroy, A. K., Walter, F., Brinks, E., Bigiel, F., de Blok, W. J. G., Madore, B., & Thornley, M. D. 2008, AJ, 136, 2782

Leroy, A. K., et al. 2009, AJ, 137, 4670

Levinson, F. H., & Roberts, W. W., Jr. 1981, ApJ, 245, 465

Li, Y., Mac Low, M.-M., & Klessen, R. S. 2005, ApJ, 626, 823

Lin, C. C., & Shu, F. H. 1964, ApJ, 140, 646

Lin, C. C., & Shu, F. H. 1966, Proceedings of the National Academy of Science, 55, 229

Lindblad, B. 1940, ApJ, 92, 1

Lindblad, P. O. 1960, Stockholms Observatoriums Annaler, 21, 4

Loinard, L., Dame, T. M., Koper, E., Lequeux, J., Thaddeus, P., & Young, J. S. 1996, ApJ, 469, L101

Lord, S. D., & Young, J. S. 1990, ApJ, 356, 135

Lubow, S. H., Cowie, L. L., & Balbus, S. A. 1986, ApJ, 309, 496

Lynden-Bell, D., & Kalnajs, A. J. 1972, MNRAS, 157, 1

Lynds, B. T. 1970, The Spiral Structure of our Galaxy, 38, 26

Marinova, I., & Jogee, S. 2007, ApJ, 659, 1176

Mathewson, D. S., van der Kruit, P. C., & Brouw, W. N. 1972, A&A, 17, 468

McKee, C. F., & Ostriker, E. C. 2007, ARA&A, 45, 565

Meidt, S. E., Rand, R. J., & Merrifield, M. R. 2009, ApJ, 702, 277

Merrifield, M. R., Rand, R. J., & Meidt, S. E. 2006, MNRAS, 366, L17

Mo, H. J., Mao, S., & White, S. D. M. 1998, MNRAS, 295, 319

Naab, T., & Burkert, A. 2003, ApJ, 597, 893

Navarro, J. F. & Benz, W. 1991, ApJ, 380, 320

Navarro, J. F. & White, S. D. M. 1994, MNRAS, 267, 401

Navarro, J. F. & Steinmetz, M. 1997, ApJ, 478, 13

Oort, J. H. 1962, The Distribution and Motion of Interstellar Matter in Galaxies, 234

Pasha, I. I., & Smirnov, M. A. 1982, Ap&SS, 86, 215

Pasha, I. I. 1985, Soviet Astronomy Letters, 11, 1

Pasha, I. I. 2004, arXiv:astro-ph/0406142

Pasha, I. I. 2004, arXiv:astro-ph/0406143

Peebles, P. J. E. 1969, ApJ, 155, 393

Peebles, P. J. E. 1982, ApJ, 263, L1

Peng, C. Y., Ho, L. C., Impey, C. D., & Rix, H.-W. 2002, AJ, 124, 266

Pérez, I., Márquez, I., Freeman, K., & Fux, R. 2005, A&A, 438, 127

Phillipps, S., & Disney, M. 1985, MNRAS, 217, 435

Planck Collaboration 2006, arXiv:astro-ph/0604069

Pohlen, M., & Trujillo, I. 2006, A&A, 454, 759

Rand, R. J., & Kulkarni, S. R. 1990, ApJ, 349, L43

Rand, R. J. 1995, AJ, 109, 2444

Rix, H.-W., & Zaritsky, D. 1995, ApJ, 447, 82

Roberts, W. W. 1969, ApJ, 158, 123

Roberts, W. W., Jr., Roberts, M. S., & Shu, F. H. 1975, ApJ, 196, 381

Roškar, R., Debattista, V. P., Quinn, T. R., Stinson, G. S., & Wadsley, J. 2008, ApJ, 684, L79

Rots, A. H. 1975, A&A, 45, 43

Rubin, V. C., & Ford, W. K., Jr. 1970, ApJ, 159, 379

Rubin, V. C., Ford, W. K. J., & . Thonnard, N. 1980, ApJ, 238, 471

Sancisi, R., Allen, R. J., & Sullivan, W. T., III 1979, A&A, 78, 217

Sanduleak, N. 1969, AJ, 74, 47

Schinnerer, E., Weiss, A., Aalto, S., & Scoville, N. Z. 2010, arXiv:1007.0692

Schlegel, D. J., Finkbeiner, D. P., & Davis, M. 1998, ApJ, 500, 525

Schmidt, M. 1959, ApJ, 129, 243

Schneider, S. E. 1989, ApJ, 343, 94

Schuster, K. F., Kramer, C., Hitschfeld, M., Garcia-Burillo, S., & Mookerjea, B. 2007, A&A, 461, 143

Schweizer, F. 1976, ApJS, 31, 313

Seiden, P. E., & Gerola, H. 1979, ApJ, 233, 56

Seigar, M. S., & James, P. A. 1998, MNRAS, 299, 685

Seigar, M. S., & James, P. A. 2002, MNRAS, 337, 1113

Sellwood, J. A., & Carlberg, R. G. 1984, ApJ, 282, 61

Sellwood, J. A., & Lin, D. N. C. 1989, MNRAS, 240, 991

Sellwood, J. A., & Kahn, F. D. 1991, MNRAS, 250, 278

Sellwood, J. A. 2000, Ap&SS, 272, 31

Sellwood, J. A., & Binney, J. J. 2002, MNRAS, 336, 785

Sellwood, J. A. 2010, arXiv:1001.5430

Sheth, K., et al. 2008, ApJ, 675, 1141

Shetty, R., Vogel, S. N., Ostriker, E. C., & Teuben, P. J. 2007, ApJ, 665, 1138

Skelton, R. E., Bell, E. F., & Somerville, R. S. 2009, ApJ, 699, L9

Sofue, Y., Tutui, Y., Honma, M., Tomita, A., Takamiya, T., Koda, J., & Takeda, Y. 1999, ApJ, 523, 136

Somerville, R. S. 2002, ApJ, 572, L23

Sparke, L. S., van Moorsel, G., Schwarz, U. J., & Vogelaar, M. 2009, AJ, 137, 3976

Springel, V., & Hernquist, L. 2003, MNRAS, 339, 289

Springel, V. 2005, MNRAS, 364, 1105

Strateva, I., et al. 2001, AJ, 122, 1861

Tamburro, D., Rix, H.-W., Walter, F., Brinks, E., de Blok, W. J. G., Kennicutt, R. C., & MacLow, M.-M. 2008, AJ, 136, 2872

Tan, J. C. 2000, ApJ, 536, 173

Thacker, R. J., & Couchman, H. M. P. 2001, ApJ, 555, L17

Thornley, M. D. 1996, ApJ, 469, L45

Tielens, A. G. M. 2005, The Physics and Chemistry of the Interstellar Medium, Cambridge, UK: Cambridge University Press, 2005.

Toomre, A. 1964, ApJ, 139, 1217

Toomre, A., & Toomre, J. 1972, ApJ, 178, 623

Toomre, A. 1977, ARA&A, 15, 437

Toomre, A. 1981, Structure and Evolution of Normal Galaxies, 111

Tully, R. B., & Fisher, J. R. 1977, A&A, 54, 661

Tully, R. B., Shaya, E. J., Karachentsev, I. D., Courtois, H. M., Kocevski, D. D., Rizzi, L., & Peel, A. 2008, ApJ, 676, 184

Valenzuela, O., & Klypin, A. 2003, MNRAS, 345, 406

van den Bergh, S. 1960, ApJ, 131, 215

van den Bergh, S. 1960, ApJ, 131, 558

van der Kruit, P. C., & Shostak, G. S. 1982, A&A, 105, 351

van der Kruit, P. C. 1987, A&A, 173, 59

Verdes-Montenegro, L., Bosma, A., & Athanassoula, E. 2002, A&A, 389, 825

Vogel, S. N., Kulkarni, S. R., & Scoville, N. Z. 1988, Nature, 334, 402

Wada, K., & Koda, J. 2004, MNRAS, 349, 270

Walter, F., Brinks, E., de Blok, W. J. G., Bigiel, F., Kennicutt, R. C., Thornley, M. D., & Leroy, A. 2008, AJ, 136, 2563

Wong, T., & Blitz, L. 2002, ApJ, 569, 157

Woodward, P. R. 1975, ApJ, 195, 61

York, D. G., et al. 2000, AJ, 120, 1579

Young, J. S., & Scoville, N. Z. 1991, ARA&A, 29, 581

Zhang, X. 1996, ApJ, 457, 125

Zhang, X. 1998, ApJ, 499, 93

Zhang, X. 1999, ApJ, 518, 613

Zibetti, S., Charlot, S., & Rix, H.-W. 2009, MNRAS, 400, 1181

Zibetti, S. 2009, arXiv:0911.4956